ISSN: 2153-036X Vol.1, No.2, August 2010

Scientific Research

Journal of Biophysical Chemistry

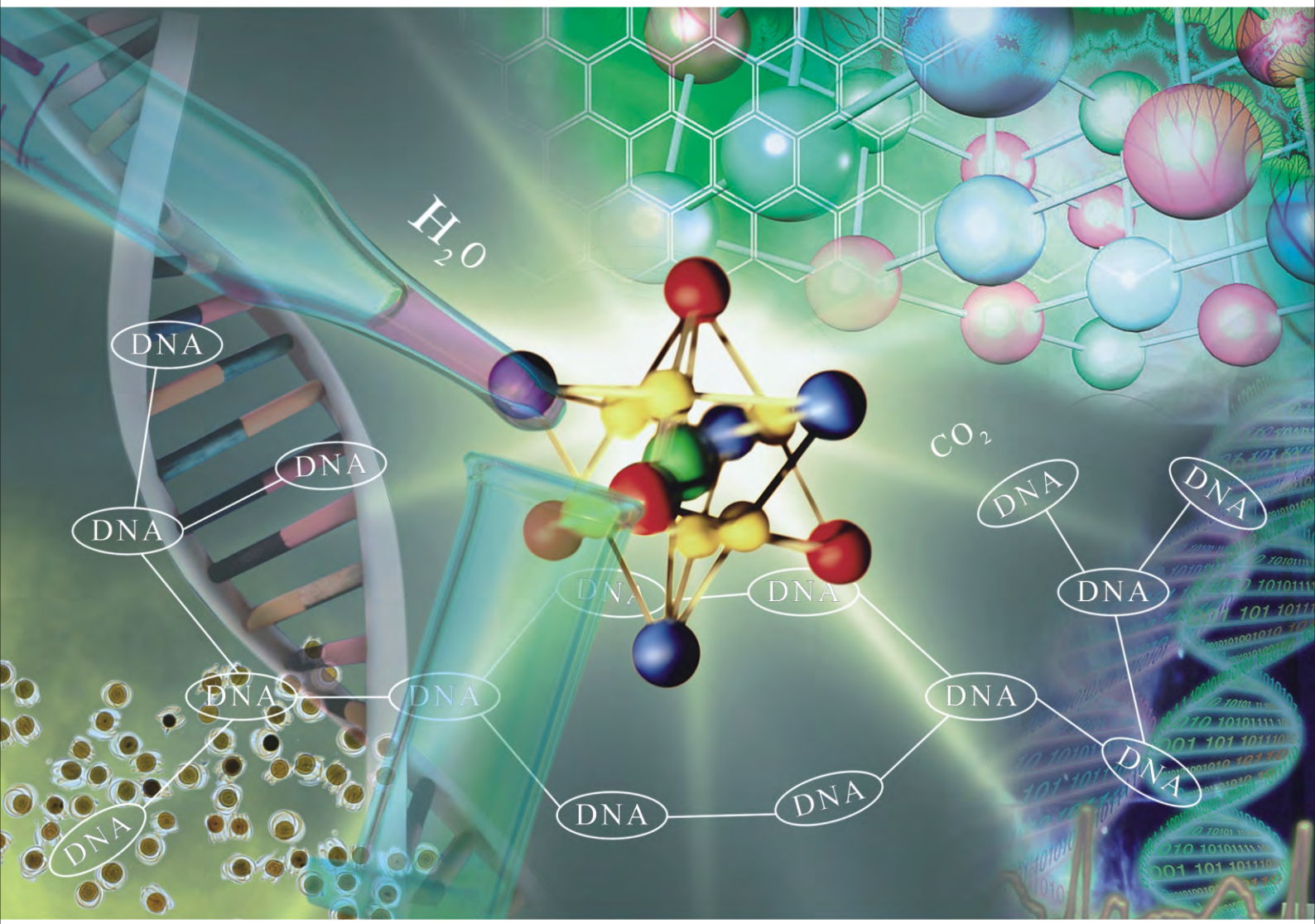

ISSN 2153-036X

9 772153 036007 02

www.scirp.org/journal/jbpc

Journal Editorial Board

ISSN 2153-036X (Print) ISSN 2153- 0378 (Online)

http://www.scirp.org/journal/jbpc/

TABLE OF CONTENTS

Volume 1, Number 2, August 2010

Journal of Biophysical Chemistry

Journal Information

SUBSCRIPTIONS

Journal of Biophysical Chemistry (Online at Scientific Research Publishing, www.SciRP.org) is published quarterly by Scientific Research Publishing, Inc., USA.

Subscription rates:

Print: $50 per issue.
To subscribe, please contact Journals Subscriptions Department, E-mail: sub@scirp.org

SERVICES

Advertisements
Advertisement Sales Department, E-mail: service@scirp.org

Reprints (minimum quantity 100 copies)
Reprints Co-ordinator, Scientific Research Publishing, Inc., USA.
E-mail: sub@scirp.org

COPYRIGHT

PRODUCTION INFORMATION

For manuscripts that have been accepted for publication, please contact:
E-mail: jbpc@scirp.org

Vol.1, No.2, 77-85 (2010)
doi:10.4236/jbpc.2010.12010

Journal of Biophysical Chemistry

Distance-dependent coherent charge transport in DNA: crossover from tunneling to free propagation

Natallia V. Grib[1*], Dmitry A. Ryndyk[2], Rafael Gutiérrez[3], Gianaurelio Cuniberti[3]

[1]Department of Micro- and Nanoelectronics, Belarusian State University of Informatics and Radioelectronics, Minsk, Belarus; *Corresponding Author: ngrib@uvic.ca
[2]Institute for Theoretical Physics, University of Regensburg, Regensburg, Germany
[3]Institute for Material Science and Max Bergmann Center for Biomaterials, Dresden University of Technology, Dresden, Germany

Received 8 June 2010; revised 4 July 2010; accepted 10 July 2010.

ABSTRACT

Using a tight-binding model, we investigate the influence of intra- and interstand coupling parameters on the charge transport properties in a G-$(T)_j$-GGG DNA sequence and its (G:C)-$(T:A)_j$-$(G:C)_3$ duplex attached to four electrodes. Dependences of the transmission function and of the corresponding conductance of the system on the number of bridging sites were obtained. Simulation results of a recently proposed two-strand superexchange (tunneling) model were reproduced and extended. It is demonstrated that the crossover from strong to weak distance-dependent charge transport is elucidated by a transition from under-barrier tunneling mechanism to free over-barrier propagation in the coherent regime, controlled by temperature and coupling parameters. The role of DNA-electrode coupling has been also considered. It was found that an asymmetry in the DNA-electrode coupling has a drastic effect on the conductance leading to an increase in delocalization of the electronic states in the DNA duplex.

Keywords: DNA; Electron Transport; Modeling of DNA; Electronic Structure of DNA

1. INTRODUCTION

The discovery of charge migration in deoxyribonucleic acid (DNA) stimulated intensive investigations of the electronic properties of DNA due to their significance in biosynthesis and radiation-induced damage and repair processes [1-3]. Furthermore, considerable interest in nanodimensional structures of DNA possessing unique self-assembling and self-recognition properties has increased the last decade in connection with the possibility of the development of molecular nanoelectronic devices which are expected to provide high storage of information and high-speed signal processing within a wide temperature range [4-6]. In fact, DNA molecules can be well combined with silicon technology transcending the potential of the present quantum wires and are supposed to be used in modern computer technology as a binary data structure by applying a programmable linear self-assembly of the sequence of complementary nucleic base pairs of DNA [7,8].

Until now numerous experimental and theoretical data on charge migration through DNA molecules show an apparently contradictory behavior which can be elucidated by supposing two primary mechanisms. They include the single-step superexchange (tunneling) charge transfer that is strongly dependent on length of a molecular chain, and the multi-step hopping mechanism that is characterized by a weak change in the charge transfer efficiency (CTE) with increasing of the donor-acceptor distance in the double helix [9-11]. However, experimental measurements of DNA molecule do not give any unequivocal evidence in favor of one or other mechanism of charge transfer in DNA. Many of them demonstrate a combined hopping-superexchange mechanism with a transition from the coherent superexchange to the thermally induced incoherent hopping process.

Beside electron *transfer* experiments, also *transport* experiments became an important field of modern research. In transport measurements a molecule is placed between metallic leads and steady-state current can be produced by finite voltage. A direct measurement of electrical transport through single biological molecules, such as DNA and peptides [12,13], is a very appealing, although challenging, issue in molecular electronics because of the potential peculiar capabilities of forming self-assembled nanodevices at the molecular scale. Quantum transport experiments through single DNA oligomers

This work was funded by the Deutsche Forschungsgemeinschaft (SPP 1243) and Collaborative Research Center SFB 689.

can be performed in both molecular junction configurations [14-17] and STM setups [18]. These enable the investigation of charge migration in both longitudinal and transverse configurations and stimulate theoretical interpretations.

Theoretically, single-step superexchange and multistep hopping models have been considered within various approaches such as variable range hopping [19,20], one-dimensional quantum mechanical tight-binding models [21-24], and nonlinear methods [25,26]. Recently, Wang and Chakraborty [27] have proposed a ladder model to describe charge transfer via DNA bridges and applied this model to the (G:C)-(T-A)$_n$-(G:C)$_3$ sequence studied experimentally by Giese *et al.* [28]. There, the presence of both transfer mechanisms was obtained by analyzing strand cleavage efficiencies that are caused by oxidized guanines. It has been shown that the superexchange mechanism exponentially decreased with distance and predominated for short bridges ($n \leq 3$) consisting of A:T base pairs. For long bridges ($n > 3$), the CTE showed an almost distance-independent behavior. This distance dependence was further proved experimentally by Lewis and co-workers [29], who clarified the rates of photoinduced charge transfer in short DNA hairpins. The theoretical analysis in [27], which addresses the conductance of the same sequence rather than the CTE, rests on Landauer theory and implicitly assumes purely coherent charge propagation upon injection. As shown by the authors, by tuning the inter-strand coupling the experimentally observed [28,29] length dependence vs. n can be reproduced. Wang and Chakraborty interpreted the crossover between strong and weak length dependencies as a transition to a quasitwo dimensional behavior characterized by a topological effect. While there is a consensus that the exponential decrease of CTE with number of A:T base pair for short bridges is related to a superexchange tunneling process between the distant G-bases, the saturation of CTE for large n seems more difficult to understand.

In this paper, we consider a ladder model within a nearest-neighbor tight-binding picture to describe the distance dependent charge transport in DNA. We introduce the model Hamiltonian and discuss the transmission function which is required to calculate the conductance in DNA in order to reproduce and to extend the Wang-Chakraborty model [27]. We show that different electronic coupling regimes of nucleobases in DNA within its single- and double-stranded configurations can determine the crossover point from exponential distance dependence of charge transfer to length-independent behavior.

2. MODEL

The DNA molecules under study are considered to consist of repeated stacks of nucleobases formed by either A-T/T-A or G-C/C-G pairs located along a sugar-phosphate frame, as shown schematically in **Figure 1**. Hydrogen bonds between basic and acid centers of the complementary bases and also their stacking interaction stabilize the spiral structure of the molecule and do not participate in the charge carrier transport. It has determined that a $\pi - \pi$ orbital overlapping of neighboring nucleobases forms the basis of charge transfer mechanism in DNA [30] allowing the basic charge carriers (holes) to jump from one base to another with increasing their transfer rate for the sequence of identical nucleotides. Since the guanine has the lowest oxidation potential [31], holes are effectively trapped at the sites of guanines in the DNA duplex, where (5′-G) segment supposed to be a donor and (GGG-3′) site performs an acceptor function (see red regions in **Figure 1**). We assume that charge carriers are moving along the base-pair stack in the direction of an applied electric field, thus neglecting the slow migration of holes in the opposite direction. In the model we do not take into account environmental effects and helical impact arising from the real structure of the DNA.

Along the lines of [21] and [32], we represent the DNA molecule with N-base-pair nucleic chains, attached to four semi-infinite electrodes by the following tight-binding Hamiltonian (**Figure 1**):

$$\hat{H} = \hat{H}_{S1} + \hat{H}_{S2} + \hat{H}_{S1-S2} + \hat{H}_L + \hat{H}_R + \hat{H}_L^{(T)} + \hat{H}_R^{(T)} \quad (1)$$

Hamiltonians for the first $\hat{H}_{S1}$, second $\hat{H}_{S2}$ DNA strands and the coupling between them $\hat{H}_{S1-S2}$ are described as:

$$\hat{H}_{S1} = \varepsilon_G b_1^\dagger b_1 + \sum_{i=n-2}^{n} \varepsilon_G b_i^\dagger b_i + \sum_{i=2}^{j+1} \varepsilon_i b_i^\dagger b_i + t_\parallel \sum_{i=1}^{n-1} \left[b_i^\dagger b_{i+1} + h.c. \right] \quad (2)$$

$$\hat{H}_{S2} = \varepsilon_C c_{n+1}^\dagger c_{n+1} + \sum_{i=N-2}^{N} \varepsilon_C c_i^\dagger c_i + \sum_{i=n+2}^{n+j+1} \varepsilon_i c_i^\dagger c_i + t_\parallel \sum_{i=n+1}^{N-1} \left[c_i^\dagger c_{i+1} + h.c. \right] \quad (3)$$

$$\hat{H}_{S1-S2} = t_\perp \sum_{i=1}^{n} \left[b_i^\dagger c_i + h.c. \right], \quad (4)$$

where $b_i^\dagger(b_i)$ is the creation (annihilation) operator of hole on ith site in the first DNA strand ($1 \leq i \leq n$) and $c_i^\dagger(c_i)$ is the same operator in the second molecular strand ($n + 1 \leq i \leq N$). The on-site energies ε_i are evaluated by ionization potentials of the respective nucleobases as the HOMO hole energies given in [10,33]: ε_G = 7.75 eV, ε_C = 8.87 eV, ε_T = 9.14 eV and ε_A = 8.24 eV. The coupling parameter $t_\parallel$ is the corresponding nearest-neighbor electronic hopping

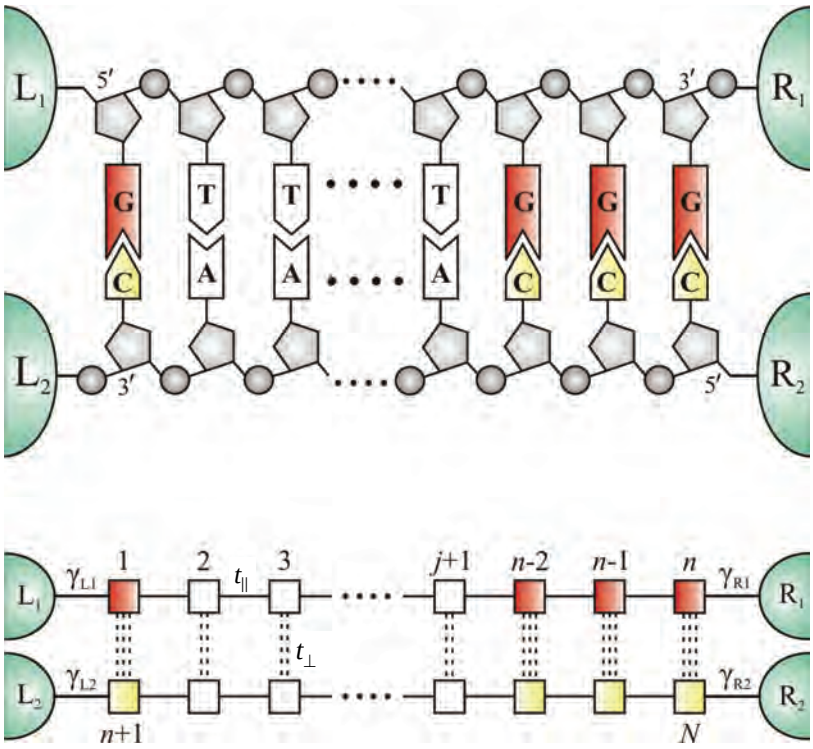

Figure 1. Upper panel: Schematic representation of the double-strand DNA attached to four semi-infinite left ($L_{1,2}$) and right ($R_{1,2}$) electrodes. A nucleobase-pair sequence with the donor (5'-G) and acceptor (GGG-3') segments is placed between two sugar-phosphate backbones. Lower panel: A two-leg ladder model of the DNA with the $(G:C)$-$(T:A)_j$-$(G:C)_3$ configuration used to imitate the double-strand structure of a DNA molecule. Charge carriers are moved along the 5'-G-$(T)_j$-GGG-3' chain from the emitter electrode L_1 to the collector electrode R_1.

integral along the two strands while $t_\perp$ describes the inter-strand hopping.

The Hamiltonians of the left and right electrodes represented by the terms $\hat{H}_L$ and $\hat{H}_R$ in (1) and their contact Hamiltonians with the DNA duplex $\hat{H}_L^{(T)}$ and $\hat{H}_L^{(T)}$ are given as:

$$\hat{H}_{L(R)} = \sum_{k\in L,R} \left[\varepsilon_k a_k^\dagger a_k + h.c. \right] \quad (5)$$

$$\hat{H}_L^{(T)} = \gamma_{L1} \sum_{k\in L_1} \left[a_k^\dagger b_1 + h.c. \right] + \gamma_{L2} \sum_{k\in L_2} \left[a_k^\dagger c_{n+1} + h.c. \right] \quad (6)$$

$$\hat{H}_R^{(T)} = \gamma_{R1} \sum_{k\in R_1} \left[a_k^\dagger b_n + h.c. \right] + \gamma_{R2} \sum_{k\in R_2} \left[a_k^\dagger c_N + h.c. \right] \quad (7)$$

Here, ε_k is the energy of electrons in the leads, $a_k^\dagger(a_k)$ is the creation (annihilation) operator of hole in the state k, $\gamma_{L1(L2)}$ and $\gamma_{R1(R2)}$ are the coupling terms to the left and right electrodes, respectively (**Figure 1**).

Studying the injected hole transport along the 5'-G-$(T)_j$-GGG-3' DNA chain located between the emitter electrode L_1 and the collector electrode R_1 as in [27], the choice of the intra- and inter-strand electronic transfer integrals is of considerable importance. The least change in their values can lead to quite different quantum transfer properties in DNA duplexes because the coupling parameters are rather sensitive to the relative position of two neighboring nucleobases due to their highly anisotropic π-bonds [34]. In order to reduce the number of model parameters and to simplify our computation we have adopted a simple parameterization taking a homogenous hopping along both legs in a range of 0.1 – 0.5 eV for the coupling parameter $t_\parallel$ and 0.01 – 0.07 eV for inter-strand hopping integral $t_\perp$. While in [35] has been shown that hopping integral values are different for each combination of nucleotide pairs and the inter-strand hopping is usually very small, ~ few meV [36], we do not consider the hopping integrals as bare tight-binding parameters but as effective ones, thus keeping some freedom in the choice of their specific values.

To diminish contact effects on quantum tunneling-transport process in the DNA molecule, the contact strength with the left and the right DNA chain ends is kept constant and the coupling parameter $\gamma_{L(R)}$ supposed to be much larger than the coupling parameter between the nucleobases in the DNA sequence [27]. We choose equal couplings to all electrodes ($\gamma_{L1}= \gamma_{L2}= \gamma_{R1}= \gamma_{R2}= 1.5$ eV) that provides a decrease in the influence of interference

effects at the electrode-DNA interface [37] and allows to ascertain the veritable conduction properties of the DNA.

The Green's function theory is used to calculate the transmission coefficient in the open system "electrode-DNA-electrode" by the expression

$$t(E) = Tr\left\{ \Gamma_L \hat{G}(E) \Gamma_R \hat{G}^{\dagger}(E) \right\} \quad (8)$$

with the Green function, $\hat{G}(E) = [EI - \hat{H} - \Sigma]^{-1}$. Here the self-energy $\Sigma = \Sigma_L + \Sigma_R$ is introduced due to the contacts of the DNA molecules to the left and the right metallic electrodes, and the corresponding coupling matrices are related to the self-energies as $\Gamma_{L(R)} = \mathrm{Im}(\Sigma_{L(R)} - \Sigma^{\dagger}_{L(R)})$. Then the N × N ladder-lead energy-independent coupling matrices within the wide-band limit in the electrodes spectral densities are given by

$$(\Gamma_L)_{ml} = \gamma_{L1}\delta_{m,1}\delta_{l,1} + \gamma_{L2}\delta_{m,n+1}\delta_{l,n+1}$$
$$(\Gamma_R)_{ml} = \gamma_{R1}\delta_{m,n}\delta_{l,n} + \gamma_{R2}\delta_{m,N}\delta_{l,N} \quad (9)$$

Finally, the conductance of the DNA molecule in the coherent regime is defined as

$$g(E) = \frac{2e^2}{h} \int_{-\infty}^{\infty} t(E) \left(-\frac{\partial f(E)}{\partial E} \right) dE, \quad (10)$$

where $f(E) = (\exp[(E - E_F)/k_BT] + 1)^{-1}$ is the Fermi function at the room temperature T. As an essential physical factor controlling the injection efficiency of holes onto the stack of nucleobases is the local position of the electrode Fermi level E_F relative to the unoccupied molecular orbitals, we assume the energy coincides with the on-site energy of guanine in the chain at the fixed voltage threshold. In this case the conductance of the DNA molecule starts to be governed by the ability of the base pair sequence to transport a charge rather than by the injection process.

3. SIMULATION RESULTS AND DISCUSSION

We evaluated the transmission coefficient $t(E_F)$ at the Fermi energy and the corresponding conductance $g(E)$ as functions of number j (T:A) nucleobase pairs that compose the molecular bridge and determine the length of the (G:C)-(T:A)$_j$-(G:C)$_3$ DNA duplex (**Figure 2**). At first the calculations have been carried out for different values of intrastrand hopping integral $t_{\parallel}$ in the single-stranded 5'-G-(T)$_j$-GGG-3' DNA sequence when $t_{\perp} = 0$ (1-4 lines in **Figure 2(a)**). For this case the simulation results show a typical exponential distance-dependent behavior of single-step hole-transfer process in DNA with increasing T-bases as has been found for the current through the same DNA chain in [27]. A temperature contribution to a conduction mechanism of the one-leg DNA configuration

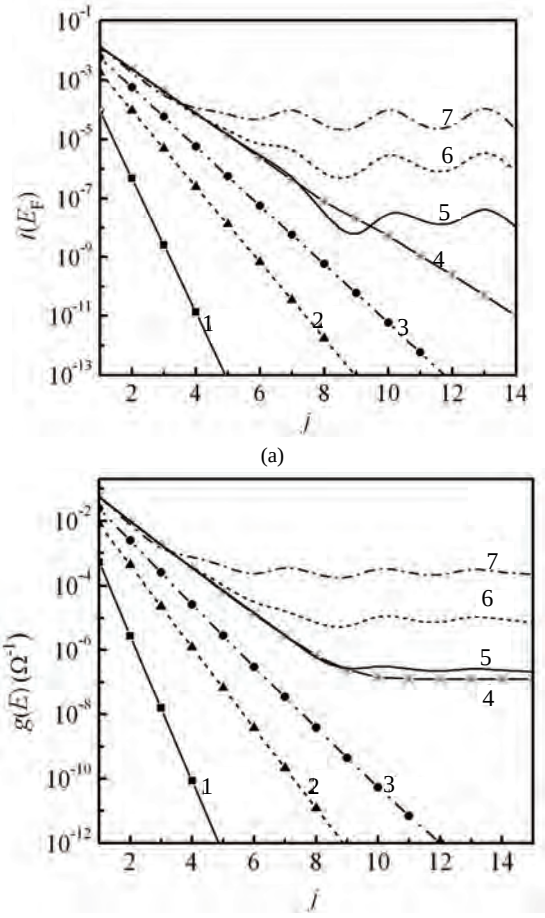

Figure 2. (a) Transmission coefficient $t(E_F)$ and (b) corresponding conductance $g(E)$ vs. number of j (T:A) base pairs at T = 300 K for different intrastrand hopping integrals $t_{\parallel}$ (1 – 0.1 eV, 2 – 0.3 eV, 3 – 0.4 eV, 4 – 0.5 eV) in the single-strand structure of 5'-G-(T)$_j$-GGG-3' DNA (equivalent to $t_{\perp} = 0$) and for various values of the interstrand hopping $t_{\perp}$ (5 – 0.01 eV, 6 – 0.03 eV, 7 – 0.07 eV) at fixed $t_{\parallel} = 0.5$ eV in the double-stranded (G:C)-(T:A)$_j$-(G:C)$_3$ molecule. Coupling to the electrodes are $\gamma_{L1} = \gamma_{L2} = \gamma_{R1} = \gamma_{R2} = 1.5$ eV.

results in modification of the distance dependence when the overlapping of adjacent nucleobases becomes rather big. In **Figure 2(b)** it is seen a transition from the strong to the weak distance dependence of the conductance $g(E)$ at the intrastrand hopping integral $t_{\parallel} = 0.5$ eV (curve 4). The presence of such the crossover was obtained to appear only for the two-stranded DNA in the Wang-Chakraborty model [27]. The point is that the T-bridge forms an energy barrier for charge carries, propagating free through electronic states of G-bases, which have the on-site energies close to the Fermi energy in the electrodes (**Figure 3**, mechanism 1). This barrier is lower for longer bridges since the splitting between the bridge states of the identical bases is larger for longer bridge lengths leading to a

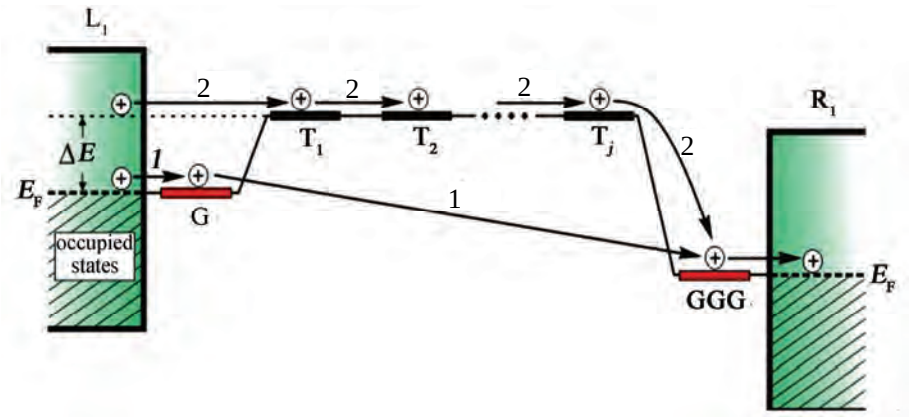

Figure 3. An approximate energetic scheme for hole transport in the 5'-G-$(T)_j$-GGG-3' DNA strand: 1 – under-barrier tunneling mechanism between G-base and GGG-triplet connected to the metal leads; 2 – free over-barrier propagation along the T-bridge with a hole energy ΔE in the emitter electrode comparable with the energy level of T-nucleotide at finite temperature (see text).

strong overlap between orbitals in the linear T-chain [20]. At finite temperature the holes in the leads exist also at energies, sufficient for their capture by the first T-nucleotide in the bridge, and can coherently tunnel through the extended electronic states of T-bases resulting in distance-independent conductance while the number of the bridging sites rises (**Figure 3**, mechanism 2). The next curves (5-7) in **Figure 2** were obtained for the double-stranded (G:C)-$(T:A)_j$-$(G:C)_3$ molecule at fixed $t_{\parallel}$ = 0.5 eV along both legs when the interstrand coupling parameter $t_{\perp}$ is variable. An increase in the number of periodic nucleotides, which constitute the (T:A) molecular bridge, leads to a formation of an energy gap due to the high degree of their π-orbital overlap and the large interstrand coupling between them. In what follows, the hole migration through the set of (T:A) base pairs has a band-like behavior with preservation of hole energy during the transport process in the DNA. A crossover region is characterized by an appearance of oscillations for larger number of (T:A) dinucleotides when the over-barrier charge propagation through the (T:A) bridge preponderates over the under-barrier tunneling mechanism from the donor G-site to the acceptor GGG and shifts toward smaller j with increasing $t_{\perp}$. However, it has a smoother behavior in comparison with the result of the work [27] and the experimental findings [28,38,39]. We suppose that these oscillations are to be a consequence of neglecting the environmental effects and the electron-phonon interaction in the system, and smaller for the dependence of $g(E)$ on j due to temperature effect.

To reach a clearer understanding of the transport mechanisms we investigated the energy dependent transmission $t(E)$ for different length of the molecular bridge in the 5'-G-$(T)_j$-GGG-3' DNA configuration and its (G:C)-$(T:A)_j$-$(G:C)_3$ duplex. The results are displayed in **Figure 4**. The transmission spectrum consists of peaks related to the energetic states of the corresponding nucleobases, which take part in the hole transport. At the same time in the strong coupling regime (in this case $t_{\parallel}$ = 0.5 eV) some peaks are merged due to an increase in the hybridization between the π orbitals of the bases giving a broadening of the electronic manifolds. An inset in **Figure 4(a)** used to show the transmission $t(E)$ around the Fermi energy for j = 2, 3, 6, 10 and 12. An extension of the bridge does not modify the charge propagation mechanism by the primary unistep model and just leads to exponential decreasing of the charge transfer rate in the 5'-G-$(T)_j$-GGG-3' DNA strand. However, in the analogical inset of **Figure 4(b)** we observe that the $t(E)$ picks have a steady spectral level for the (G:C)-$(T:A)_j$-$(G:C)_3$ duplex when j is more than 6, in that way demonstrating the crossover from the unistep transport through guanine sites to the coherent tunneling through the long (T:A) bridge. The obtained displacement of the picks can be explained by an energy alteration of the charge transport pathways [27].

In view of the fact that the hopping integral between the bases along the DNA chain has been determined not to exceed 0.4 eV [23,35,40], we calculated the transmission coefficient $t(E_F)$ (**Figure 5**) and the conductance $g(E)$ (inset in **Figure 5**) for the (G:C)-$(T:A)_j$-$(G:C)_3$ DNA molecule with increased bridge length in a weak-coupling regime, viz. at $t_{\parallel}$ = 0.1 eV. As in **Figure 2(b)**, the intrastrand hopping integral is variable. It was obtained that the magnitude of the $g(E)$ at these conditions is noticeably less than the one in case of the stronger hopping coupling between the nucleobases, while the conductance in DNA molecules has been found to be higher in the recent stud-

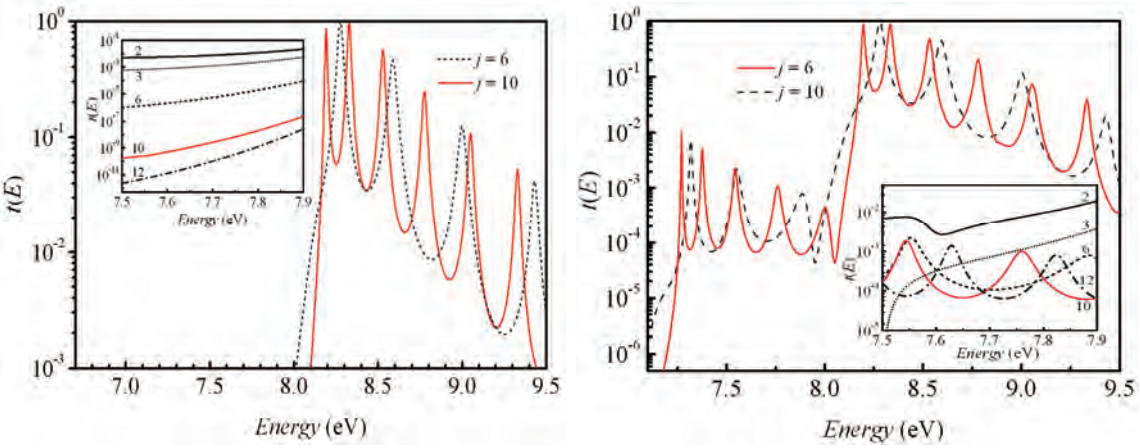

Figure 4. (a) Electronic transmission $t(E)$ as a function of the energy E for $j = 6$ and $j = 10$ in 5'-G-$(T)_j$-GGG-3' sequence of the DNA molecule. Inset: blow-up of the transmission in an energy window around the Fermi energy $E_F = 7.75$ eV for $j = 2$ (solid line), 3 (shot dotted line), 6 (dashed line), 10 (solid red line), and 12 (dot-dashed line). Parameters: $t_{\|} = 0.5$ eV, $\gamma_{L1} = \gamma_{L2} = \gamma_{R1} = \gamma_{R2} = 1.5$ eV. (b) Same as in (a) for the DNA molecule with (G:C)-$(T:A)_j$-$(G:C)_3$ configuration at $t_{\perp} = 0.07$ eV.

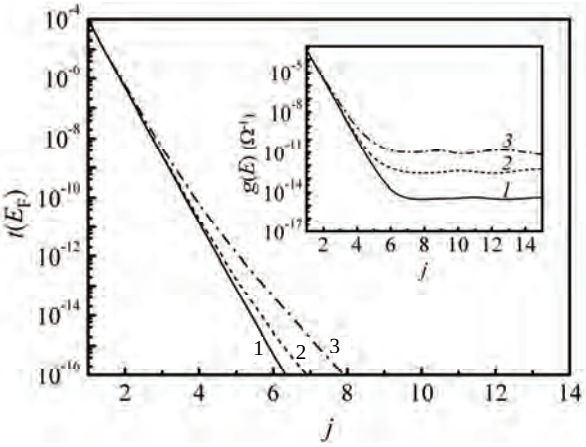

Figure 5. Transmission coefficient $t(E_F)$ vs. number of j (T:A) base pairs for different interstrand hopping integrals $t_{\perp}$ (1 – 0.01 eV, 2 – 0.03 eV, 3 – 0.07 eV) at fixed $t_{\|} = 0.1$ eV in the double-stranded (G:C)-$(T:A)_j$-$(G:C)_3$ molecule, when $\gamma_{L1} = \gamma_{L2} = \gamma_{R1} = \gamma_{R2} = 1.5$ eV. Inset: the corresponding conductance at $T = 300$ K at the same parameters.

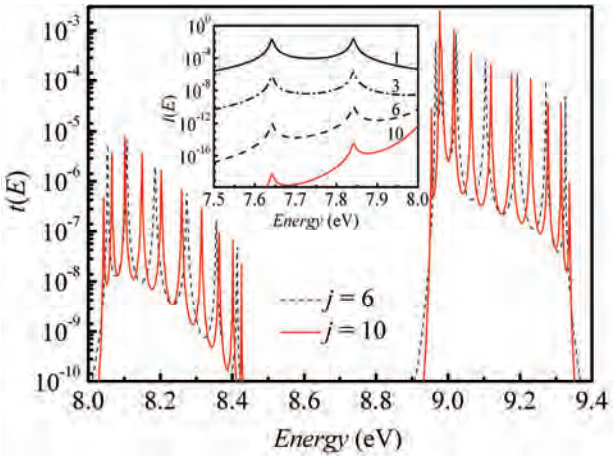

Figure 6. Energy dependent electronic transmission for $j = 6$ and $j = 10$ in the (G:C)-$(T:A)_j$-$(G:C)_3$ ladder structure of DNA. Inset: blow-up of the transmission in an energy window around the Fermi energy $E_F = 7.75$ eV for $j = 2$ (solid line), 3 (shot dotted line), 6 (dashed line), and 10 (solid red line). Parameters: $t_{\|} = 0.1$ eV, $t_{\perp} = 0.07$ eV, $\gamma_{L1} = \gamma_{L2} = \gamma_{R1} = \gamma_{R2} = 1.5$ eV.

ies [41-43]. Nevertheless, the crossover point is shifted to 6 (T:A) base pairs in that regime that is closer to the experimental results [28,41].

We find that reducing the parameter $t_{\|}$ for the two-leg DNA leads to a shift and change in width of the transmission resonances (**Figure 6**). Energetically, the transmission window moves towards larger energies with exponentially decreasing in the peak intensities. There is no much distinction in the transmission spectrum nearby the Fermi energy, where just two principal peaks are seen for $j = 1$ as well as for $j = 10$ (inset in **Figure 6**). Consequently, when the number of the (T:A) di-nucleotides is not more than 6, the single-step coherent tunneling through G-nucleotides in the duplex is the dominating transport mechanism. However, we suppose that the derived transition in the distance dependence of CTE can be distinctly modified by taking into account dynamic effects in the transmission [44] and environment. These factors and also the equalization of the Fermi energy of the DNA and the electrodes have an impact on the charge propagation pathways through DNA bridges changing significantly the energy levels of the bridging states [16].

We now consider the charge transport in the (G:C)-$(T:A)_j$-$(G:C)_3$ ladder that is coupled asymmetrically to the electrodes, when only the 5'-ends of the duplex are contacted. **Figure 7** shows the dependence of the transmission function and conductance on the number of j (T:A)

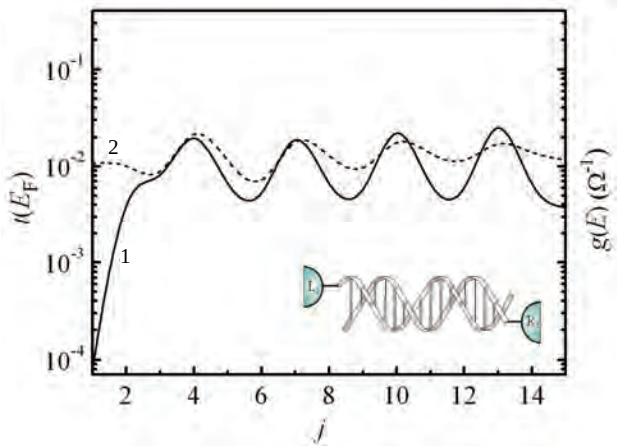

Figure 7. Transmission function $t(E_F)$ (curve 1) and conductance $g(E)$ (curve 2) vs. number of j (T:A) base pair at T = 300 K and $t_{\|}$ = 0.5 eV, $t_{\perp}$= 0.07 eV for the case of asymmetric coupling of the (G:C)-(T:A)$_j$-(G:C)$_3$ ladder to the electrodes: γ_{L1}= γ_{R2}= 1.5 eV, γ_{L2}= γ_{R1}= 0.

pairs for this contact geometry (γ_{L1}= γ_{R2}= 1.5 eV, γ_{L2}= γ_{R1}= 0). Now there is a single pathway for an electronic tunneling from the electrodes into the ladder. That results in increasing the delocalization of the electronic states in the DNA chains leading to a drastic effect on the transport characteristics. This effect is evidently displayed in **Figure 8(a)**, where new transmission peaks appear irrespective of the number of the bridging sites and the spectrum becomes more fragmented. Thus the transmission and conductance of the duplex are characterized by large oscillations and do not practically depend on the bridge length. In **Figure 8(b)** the spectrum of the electronic transmission around the Fermi energy gives an apt illustration that the holes propagate through the set of the nucleobases choosing optimal pathways to move in the structure not following the well-defined transport mechanism. Meanwhile, in a case of the asymmetric contact coupling to the 3'-end molecular sites the conductance properties do not undergo any changes, while in [45], where electron-vibron coupling has been taken into account, the absolute values of the current considerably depends on the way the two strands are contacted to the electrodes. So, the model of the charge transport in the DNA duplex, proposed in [27] and extended here, is very sensitive to the DNA-metal contact topology.

The transport mechanism based on a fully coherent picture of charge propagation through the bridge seems to be questionable in the case of DNA. For instance, the inclusion of dynamical effects into our model may qualitatively modify the calculated length dependence. Furthermore, temperature effects in this model are only associated with the electrode Fermi functions; more involved temperature dependencies – observed in the case where charge motion is coupled to dynamical degrees of freedom [20] – may therefore not be adequately described.

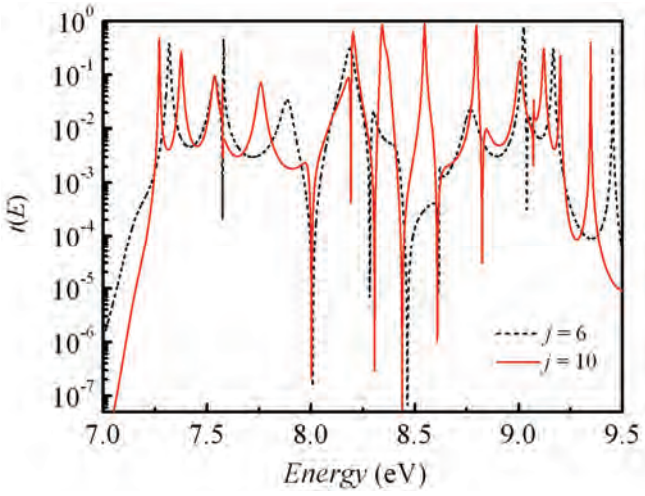

(a)

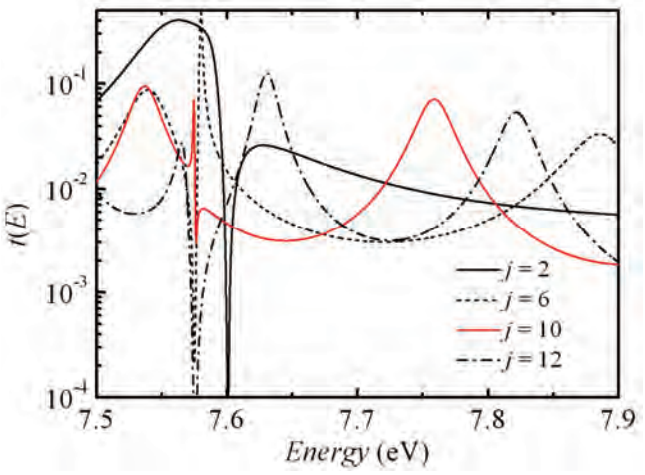

(b)

Figure 8. (a) Electronic transmission vs. energy E for j = 6 and j = 10 in (G:C)-(T:A)$_j$-(G:C)$_3$ sequence of the DNA molecule attached asymmetrically to the electrodes: γ_{L1}= γ_{R2}= 1.5 eV, γ_{L2}= γ_{R1}= 0, ($t_{\|}$ = 0.5 eV, $t_{\perp}$= 0.07 eV); (b) Electronic transmission in an energy window around the Fermi energy E_F = 7.75 eV at the same parameters.

Thus different mechanisms of charge motion in DNA cannot be distinguished only on the basis of the measured length dependence of CTE. To decide what particular mechanism dominates under given experimental conditions, the whole range of experimental data including information on the hole mobility and diffusion coefficients should be considered.

4. CONCLUSIONS

We reproduced and extended the simulation results, obtained in [27], applying a tight-binding model to a system "electrode-DNA-electrode", with standard transfer matrix formalism. It has been shown that the almost zero

distance dependence of the charge transport cannot be a result of solely the interstrand coupling in DNA, but it is a consequence of a transition from under-barrier tunneling mechanism to over-barrier propagation when the nearest neighbor hopping is chosen large enough. It was demonstrated that the crossover from the strong to the weak distance-dependent charge transport in DNA can be controlled by the electronic coupling between the complementary nucleobases within a chain as well as by their coupling between two strands. Within the proposed model, we establish that the DNA-electrode coupling governs the conductance in the molecule. An asymmetry in the contact of the DNA duplex with the electrodes has a drastic effect on the conducting properties of the system, leading to a lessening in the localization length of the positive charges along the structure.

REFERENCES

[1] Arkin, M.R., Stemp, E.D.A., Holmlin, R.E., Barton, J.K., Hörmann, A., Olson, E.J.C. and Barbara, P.F. (1996) Rates of DNA-mediated electron transfer between metallointercalators. *Science*, **273(5274)**, 475-480.

[2] Dandliker, P.J., Núñez, M.E. and Barton, J.K. (1998) Oxidative charge transfer to repair thymine dimers and damage guanine bases in DNA assemblies containing tethered metallointercalators. *Biochemistry*, **37(18)**, 6491-6502.

[3] Rajski, S.R., Jackson, B.A. and Barton, J.K. (2000) DNA repair: models for damage and mismatch recognition. *Mutation Research*, **447(1)**, 49-72.

[4] Grib, N.V., Berashevich, J.A. and Borisenko, V.E. (2006) Equivalent electrical network of the DNA molecule. *Russian Microelectronics*, **35(6)**, 398-404.

[5] Bhalla, V., Bajpai, R.P. and Bharadwaj, L.M. (2003) DNA electronics. *European Molecular Biology Organization Reports*, **4(5)**, 442-445.

[6] Niemeyer, C.M. and Adler, M. (2002) Nanomechanical devices based on DNA. *Angewandte Chemie International Edition*, **41(20)**, 3779-3783.

[7] Parker, J. (2003) Computing with DNA. *European Molecular Biology Organization Reports*, **4(1)**, 7-10.

[8] Rauhe, H., Vopper, G., Feldkamp, U., Banzhaf, W. and Howard, J.C. (2000) Digital DNA molecules. *Proceedings of 6th DIMACS Workshop on DNA Based Computers*, Leiden, 13-17 June 2000, 1-10.

[9] Jortner, J., Bixon, M., Langenbacher, T. and Michel-Beyerle, M.E. (1998) Charge transfer and transport in DNA. *Proceedings of the National Academy of Sciences of the United States of America*, **95(22)**, 12759-12765.

[10] Berlin, Y.A., Burin, A.L. and Ranter, M.A. (2000) On the long-range charge transfer in DNA. *Journal of Physical Chemistry A*, **104(3)**, 443-445.

[11] Lewis, F.D., Wu, T., Zhang, Y., Letsinger, R.L., Greenfield, S.R. and Wasielewski, M.R. (1997) Distance-dependent electron transfer in DNA hairpins. *Science*, **277(5326)**, 673-676.

[12] Porath, D., Cuniberti, G. and Di Felice, R. (2004) Charge transport in DNA-based devices. *Topics in Current Chemistry*, **237**, 183-227.

[13] Gutierrez, R., Porath, D., Cuniberti, G. and Baranowski, S. (2006) Charge transport in disordered solids with applications in electronics. John Wiley & Sons Inc., Hoboken.

[14] Porath, D., Bezryadin, A., De Vries, S. and Dekker, C. (2000) Direct measurement of electrical transport through DNA molecules. *Nature*, **403(6670)**, 635-638.

[15] Xu, B., Zhang, P., Li, X. and Tao, N. (2004) Direct conductance measurement of single DNA molecules in aqueous solution. *Nano Letters*, **4(6)**, 1105-1108.

[16] Cohen, H., Nogues, C., Naaman, R. and Porath, D. (2005) Direct measurement of electrical transport through single DNA molecules of complex sequence. *Proceedings of the National Academy of Sciences of the United States of America*, **102(33)**, 11589-11593.

[17] Cohen, H., Nogues, C., Ullien, D., Daube, S., Naaman, R. and Porath, D. (2006) Electrical characterization of self-assembled single- and double-stranded DNA monolayers using conductive AFM. *Faraday Discussions*, **131**, 367-376.

[18] Shapir, E., Cohen, H., Calzolari, A., Cavazzoni, C., Ryndyk, D.A., Cuniberti, G., Kotlyar, A.B., Di Felice, R. and Porath, D. (2008) Electronic structure of single DNA molecules resolved by transverse scanning tunnelling spectroscopy. *Nature Materials*, **7(1)**, 68-74.

[19] Yu, Z.G. and Song, X. (2001) Variable range hopping and electrical conductivity along the DNA double helix. *Physical Review Letters*, **86(26)**, 6018-6021.

[20] Renger, T. and Marcus, R.A. (2003) Variable-range hopping electron transfer through disordered bridge states: Application to DNA. *Journal of Physical Chemistry A*, **107(41)**, 8404-8419.

[21] Cuniberti, G., Craco, L., Porath, D. and Dekker, C. (2002) Backbone-induced semiconducting behavior in short DNA wires. *Physical Review B*, **65(24)**, (241314)1-4.

[22] Roche, S. (2003) Sequence dependent DNA-mediated conduction. *Physical Review Letters*, **91(10)**, (108101)1-4.

[23] Wang, H., Lewis, J.P. and Sankey, O.F. (2004) Band-gap tunneling states in DNA. *Physical Review Letters*, **93(1)**, (016401)1-4.

[24] Zhang, W. and Ulloa, S.E. (2004) Extended states in disordered systems: Role of off-diagonal correlations. *Physical Review B*, **69(15)**, (153203)1-4.

[25] Cuenda, S. and Sanchez, A. (2004) Disorder and fluctuations in nonlinear excitations in DNA. *Fluctuation and Noise Letters*, **4(3)**, L491-L504.

[26] Fialko, N.S. and Lakhno, V.D. (2000) Nonlinear dynamics of excitations in DNA. *Physical Letters A*, **278(2)**, 108-111.

[27] Wang, X.F. and Chakraborty, T. (2006) Charge transfer via a two-strand superexchange bridge in DNA. *Physical Review Letters*, **97(10)**, (106602)1-4.

[28] Giese, B., Amaudrut, J., Köhler, A.-K., Spormann, M. and Wessely, S. (2001) Direct observation of hole transfer through DNA by hopping between adenine bases and by tunnelling. *Nature*, **412(6844)**, 318-320.

[29] Lewis, F.D., Zhu, H., Daublain, P., Cohen, B. and Wasielewski, M.R. (2006) Hole mobility in DNA A tracts. *Angewandte Chemie International Edition*, **45(47)**, 7982-7985.

[30] Treadway, C.R., Hill, M.G. and Barton, J.K. (2002) Charge

transport through a molecular π-stack: Double helical DNA. *Chemical Physics*, **281(2-3)**, 409-428.

[31] Seidel, A.M., Schulz, A. and Sauer, H.M. (1996) Nucleobase-specific quenching of fluorescent dyes. 1. Nucleobase one-electron redox potentials and their correlation with static and dynamic quenching efficiencies. *Journal of Physical Chemistry*, **100(13)**, 5541-5553.

[32] Gutiérrez, R., Mandal, S. and Cuniberti, G. (2005) Dissipative effects in the electronic transport through DNA molecular wires. *Physical Review B*, **71(23)**, (235116)1-9.

[33] Sugiyama, H. and Saito, I. (1996) Theoretical studies of GG-specific photocleavage of DNA via electron transfer: significant lowering of ionization potential and 5'-localization of HOMO of stacked GG bases in B-form DNA. *Journal of the American Chemical Society*, **118(30)**, 7063-7068.

[34] Endres, R.G., Cox, D.L. and Singh, R.R.P. (2004) *Colloquium*: The quest for high-conductance DNA. *Reviews of Modern Physics*, **76(1)**, 195-214.

[35] Senthilkumar, K., Grozema, F.C., Guerra, C.F, Bickelhaupt, F.M., Lewis, F.D., Berlin, Y.A., Ratner, M.A. and Siebbeles, L.D.A. (2005) Absolute rates of hole transfer in DNA. *Journal of the American Chemical Society*, **127(42)**, 14894-14903.

[36] Nitzan, A., Jortner, J., Wilkie, J., Burin, A.L. and Ratner, M.A. (2000) Tunneling time for electron transfer reactions. *Journal of Physical Chemistry B*, **104(24)**, 5661-5665.

[37] Macia, E., Triozon, F. and Roche, S. (2005) Contact-dependent effects and tunneling currents in DNA molecules. *Physical Review B*, **71(11)**, (113106)1-4.

[38] Williams, T.T., Odon, D.T. and Barton, J.K. (2000) Variations in DNA charge transport with nucleotide composition and sequence. *Journal of the American Chemical Society*, **122(37)**, 9048-9049.

[39] Sartor, V., Boone, E. and Schuster, G.B. (2001) Long-distance radical cation migration through A/T base pairs in DNA: An experimental test of theory. *Journal of Physical Chemistry B*, **105(45)**, 11057-11059.

[40] De Pablo, P.J., Moreno-Herrero, F., Colchero, J., Gomez-Herrero, J., Herrero, P., Baro, A.M., Ordejon, P., Soler, J.M. and Artacho, E. (2000) Absence of dc-conductivity in λ-DNA. *Physical Review Letters*, **85(23)**, 4992-4995.

[41] Segal, D., Nitzan, A., Davis, W.B., Wasielewski, M.R. and Ratner, M.A. (2000) Electron transfer rates in bridged molecular systems 2. A steady-state analysis of coherent tunneling and thermal transitions. *Journal of Physical Chemistry B*, **104(16)**, 3817-3829.

[42] Valis, L., Wang, Q., Raytchev, M., Buchvarov, I., Wagenknecth, H.A. and Fiebig, T. (2006) Base pair motions control the rates and distance dependencies of reductive and oxidative DNA charge transfer. *Proceedings of the National Academy of Sciences of the United States of America*, **103(27)**, 10192-10195.

[43] Voityuk, A.A. (2005) Charge transfer in DNA: Hole charge is confined to a single base pair due to solvation effects. *Journal of Chemical Physics*, **122(20)**, (204904)1-4.

[44] Davies, O.R. and Inglesfield, J.E. (2004) Embedding method for conductance of DNA. *Physical Review B*, **69**, (195110)1-4.

[45] Gutierrez, R., Mohapatra, S., Cohen, H., Porath, D. and Cuniberti, G. (2006) Inelastic quantum transport in a ladder model: Implications for DNA conduction and comparison to experiments on suspended DNA oligomers. *Physical Review B*, **74(23)**, (235105)1-10.

Vol.1, No.2, 86-95 (2010)
doi:10.4236/jbpc.2010.12011

Journal of Biophysical Chemistry

Curvature-driven lipid sorting: coarse-grained dynamics simulations of a membrane mimicking a hemifusion intermediate

Manami Nishizawa, Kazuhisa Nishizawa*

Department of Laboratory Medicine, Teikyo University School of Medical Technology, Tokyo, Japan; *Corresponding Author: kazunet@med.teikyo-u.ac.jp

Received 26 May 2010; revised 29 June 2010; accepted 5 July 2010.

ABSTRACT

How membrane curvature influences lipid distribution is under intensive research. In this short report, after a brief review of recent studies, the results of our coarse-grained (CG) molecular dynamics simulations of membranes with "hemifused ribbons" geometry are discussed. When membranes of a binary mixture of (dipalmitoyl-phosphatidylcholine (DPPC) / dioleoyl-phosphatidylethanolamine (DOPE) were used, DOPE accumulated in the negatively curved region of the monolayer that formed as the proximal monolayers fused (*i.e.*, *cis* leaflets). However, the enrichment was dependent on the presence of tethering molecules which kept the curvature high (the curvature radius of ~1 nm), placing the *cis* monolayers ~2-2.5 nm from each other. Simulations in which DOPE was replaced with dioleoyl-phosphatidylcholine (DOPC) showed an insignificant degree of DOPC accumulation, suggesting the importance of lateral interaction among DOPE molecules for the curvature sorting. The above composition was not close to a demixing point and our radial distribution function analysis suggested that the DOPE accumulation was not assisted by the lipid phase separation which has been shown to promote curvature-driven lipid sorting. Relevance of curvature-driven lipid sorting to biological membrane fusion is discussed.

Keywords: Membrane Fusion; Raft; Membrane Domain; Cholesterol; Lipid Phase Separation

1. INTRODUCTION

Inhomogeneous distribution of lipids within a lipid bilayer has been implicated in many biological activities. Lipid composition is different among organelles and membranous structures, implying the presence of mechanisms for lipid sorting (e.g., [1-3]). Several studies utilizing lipid-like dyes provide direct evidence for non-homogenous intracellular lipid distribution. Mukherjee *et al* [4] analyzed intracelluar distribution of three different DiI (dialkylindocarbocyanine) molecules that have the same headgroup but different acyl chains (in length or unsaturation) and showed that these display remarkably different sorting in cells. In several studies, the regions in which lipid inhomogeneity was observed often corresponded to highly curved membrane regions, suggesting that lipids are sorted primarily by curvature of the membrane. For example, when a membrane buds off during secretory and endocytic vesicle formation, some lipids are incorporated into vesicles while others are excluded [5]. In a study of *Tetrahymena* membrane [6], enrichment in cone-shaped 2-aminoethylphospholipids was shown in pore-containing membrane regions during mating when the regions become highly negatively curved. One possible mechanism for the inhomogeneous distribution is curvature-driven lipid sorting, where the lipids with intrinsic (spontaneous) curvature (due to the imbalanced size of the polar headgroups relative to the hydrophobic tail) are sorted laterally in the membrane such that the spontaneous curvature of each lipid fits better to the local membrane curvature. If the curvature-sorting works, cone-shaped lipid molecules like phosphatidylethanolamine (PE) and phosphatidylglycerol (PG) accumulate in the negatively curved region. In general, theoretical studies have suggested the possibility of lateral segregation of lipids based on the local curvature. On the other hand, the lipid accumulation at curved membrane regions is often associated with accumulation of specific proteins in the cellular environment. For example, the yeast vertex microdomain, which occurs around the periphery of the two apposed membranes on

vacuole docking, is enriched in Rab GTPase and the fusion protein as well as ergosterol, diacylglycerol and 3- and 4-phosphoinositides (e.g., [7]). This implies the difficulty in evaluating the relative importance of curvature-sorting and protein-mediated sorting of molecules in a physiological environment.

After Helfrich formulated curvature energy [8], theoretical frameworks for lateral segregation based on the lipid spontaneous curvature were proposed [9-11]. Markin [9] considered the composition dependence of spontaneous curvature and the bending stiffness of membranes. Kozlov and Helfrich [10] developed a framework for thermodynamic analyses of lipid distribution, bending stiffness and curvature. Curvature-induced phase segregation was also analyzed in a phenomenological continuum theory [11]. Curvature-driven lateral segregation of lipid was also computed in more recent works such as [12,13].

Experimental studies have significantly advanced the understanding of the curvature sorting of lipids. Using giant unilamellar vesicles (GUVs) formed from a ternary mixture of sphingomyelin, dioleoylphosphatidylcholine (DOPC) and cholesterol, in which L_o (liquid-ordered) and L_d (liquid-disordered) phases coexist, Baumgart *et al* [14] showed a correlation between domain composition and local membrane curvature. (At temperatures where single component PC bilayers would be in the fluid L_α phase, cholesterol gives rise to an intermediate degree of organization in PC membranes known as the L_o phase (e.g., [15]). Using microfabricated surfaces, Parthasarathy *et al* [16] showed that the L_o domains formed in DOPC/DPPC/cholesterol membranes, are preferentially localized at regions of low curvature. Several recent studies adopted a well-studied approach; tube-pulling from vesicles. With this method, very thin membrane tubes with a diameter of several tens of nanometers are formed by pulling a small portion of the membrane from GUVs (e.g., [17]). When applied to vesicles prepared from sphingomyelin, PC and cholesterol, this method showed that the tubes are essentially composed of membranes in the L_d phase enriched in DOPC, whereas GM1, which is known to segregate into the L_o phase, was excluded from tubes [18]. Lipid sorting by membrane curvature in these studies was therefore associated with phase separation (L_o and L_d), which is a collective behavior of lipids.

In both experiments and simulations, however, curvature sorting of lipids based on spontaneous curvature (of individual lipid molecule) has exhibited only a weak effect, not leading to strong segregation of lipids. A fluorescent-labeled lipid was used in the tube-pulling system [19], showing that spontaneous curvature is not a strong factor influencing partition of the fluorescent lipid. Intriguingly, in the same system, the Cholera toxin subunit B, a protein that interacts with several lipid molecules, showed a significant effect on curvature sorting, suggesting the importance of a collective behavior of lipids. Using fluorescence-labeled lipids and quenchers, the distribution of the lipids between the outer and inner monolayers of vesicles of various sizes was compared [20]. The difference in lipid density between the monolayers was present but small, indicating that the curvature sorting is weak [20]. In a simulation study using a CG representation of lipid (three beads for one lipid) [21], no significant sorting by curvature was observed. Theoretical consideration [13] has also suggested the weak effect of spontaneous curvature of individual lipids on curvature sorting.

Collectively, these studies have led to the consensus that lipid segregation is not significant when lipid sorting is driven only by spontaneous curvature of individual lipids. In most of the experimental settings, not only the curvature, but also the propensity toward phase separation is important for curvature sorting. That is, for curvature to induce strong lipid sorting, the lipid composition must be close to the demixing point. Thus, the enthalpy related to curvature fitness is not likely to be enough to overcome the entropic penalty that prefers good mixing.

One of the current models for membrane fusion proposes formation of a stalk (**Figures 1(a)** and **(b)**) (*i.e.*, an hourglass-shaped structure) and subsequently hemifusion intermediates (**Figures 1(c)** and **(d)**), leading to fusion pore formation (**Figure 1(e)**) [22-24]. The hemifusion intermediate is a state where contacting (proximal) monolayers are fused but the distal monolayers stay intact and therefore there is no content mixing. The model suggests that, for membrane fusion, properties of the monolayer are also important. The intrinsic curvature of lipid monolayers as well as bilayers has been studied [25,26]. However, the potential usefulness of their data has not been fully explored possibly because it is difficult to study biologically relevant "monolayers". With interest in hemifusion, we applied molecular dynamics simulation to a system mimicking a hemifusion intermediate. In this system, the curvature of a monolayer could be higher than physiologically relevant curvatures formed by bilayers. However, note that our system (*i.e.*, hemifused ribbon or 'λ'-system) has not yet been applied to membranes containing cholesterol. Therefore, more analyses are necessary in order to consider the behavior of physiological membranes in fusion intermediates.

2. SIMULATION DETAILS – HEMIFUSED MEMBRANE SYSTEM

In the present study, CG simulations of membranes con-

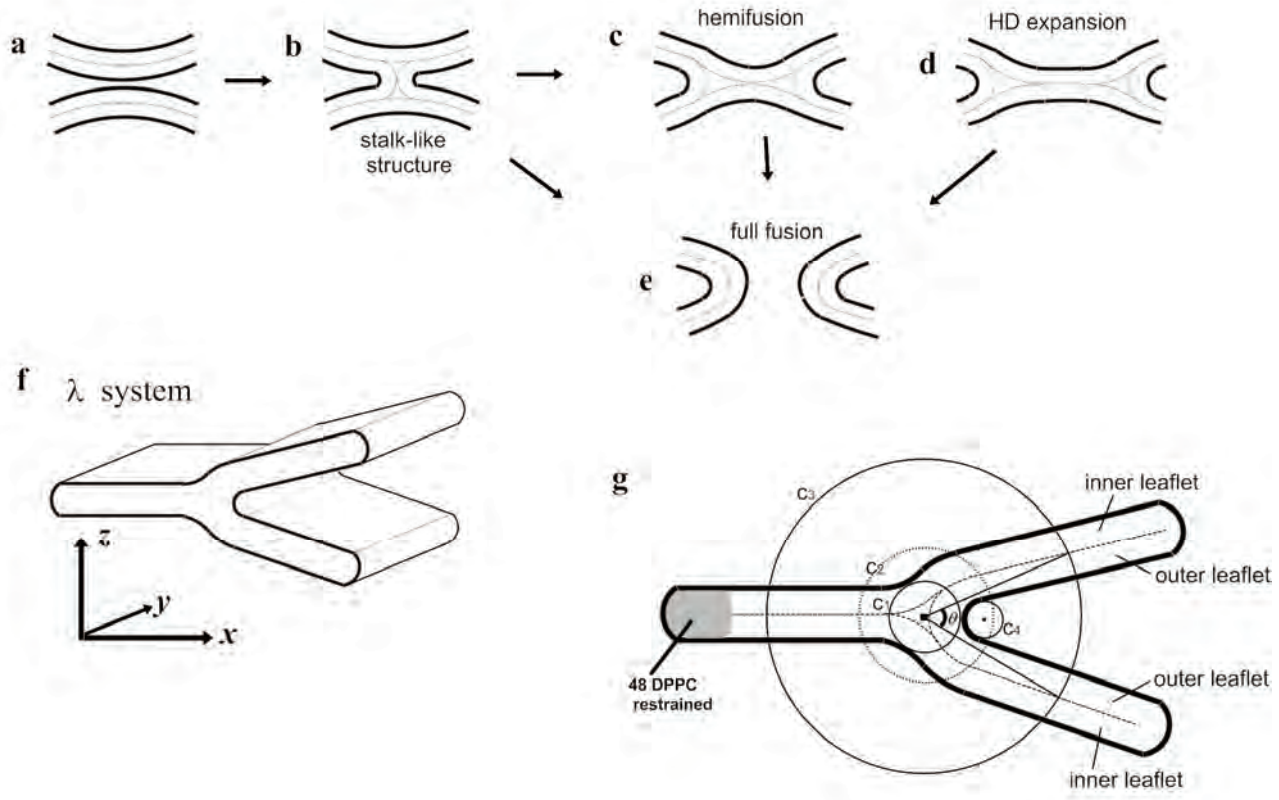

Figure 1. The stalk-hemifusion model (a-e) and the λ-system (f,g). In the stalk-hemifusion model [24], two apposed bilayers (a) initially form a stalk (b) and subsequently leads to hemifusion (c), which undergoes the hemifusion rupture (d) and finally ends with the full fusion (e). The arrow from (b) to (e) indicates a direct transition from the stalk-like structure to fusion pore formation, which has been observed in the CG-simulation studies [27,28]. (f) The λ-system. The periodic boundary condition allows the λ-shaped (hemifused) bilayer ribbons to have an infinite length in the y-direction. For clarity, water is hidden. The definition of the x,y and z directions is also shown. (g) The definition of the curvature strength. Shown are the angle between the two outer leaflets and the zone boundaries. To determine them, first, C1, the circle that has the longest radius located inside the phosphorus atoms of any lipid monolayers, is found. Two circles C2 and C3, which have the same center as that of C1 are drawn (in this study, the radius of C2 and C3 was set at 4 nm and 10 nm, respectively). C2 defines the curved region of the outer leaflet. The planar regions of the outer leaflet are defined as the regions located between the two circles whose sizes are 8nm and 12nm (radius) and the center is the same as C1. The com of each lipid molecule was used for reference. The points of intersection between C3 and the midplanes are used to define the angle θ. C4, the circle that best fits the phosphorus atoms belonging to the outer leaflet and located inside of C2, is determined. The radius of C4 represents the curvature of the outer leaflet.

taining bend(s) were carried out. We mainly used "λ-shaped" membranes (**Figure 1(f)**). This structure consists of two bilayer ribbons that are partly fused such that the cross section of the ribbon has a λ-like shape (**Figures 1(f)** and **(g)**). This structure has 2D-curvature; *i.e.*, the membranes projected onto the xz-plane are curved whereas they are basically flat along the y-axis (**Figure 1(f)**). For λ membranes, the "outer" leaflet refers to the monolayer which is highly negatively curved in **Figure 1(g)**, mimicking the fused *cis* monolayers. For the outer leaflet, the planar and the curved regions are defined as described in the legend for **Figure 1**. CG simulations were performed using the MARTINI forcefield (version 2.0) as in Marrink *et al* [29]. For example, for DPPC, the choline is represented as Q_o particle and the phosphate group as Q_a, whereas the glycerol ester, which has intermediate hydrophilicity, is represented by two N_a particles. (**Figure 2(a)**). Each of the lipid tails are modeled by four C_1 particles. For DOPE, the topology provided by Marrink *et al* (http://md.chem.rug.nl/~marrink/coarse-grain.html) was used (**Figure 2(b)**). λ membranes consisting of 350 DPPC and 184 (or DOPC molecules) were used making the nominal DOPE (or DOPC) fraction was 34.5%, but the higher density of DPPC at the membrane edges augmented the effective fraction of DOPC (DOPC) in the planar and curved regions. The leftmost part of the membrane was capped with additional 48 DPPC molecules (**Figure 1(g)**), the GL1 particles of which were harmonically restrained (with the coefficient of 100 kJ/nm^2/mol) so as to avoid the gross drift and deformation of the

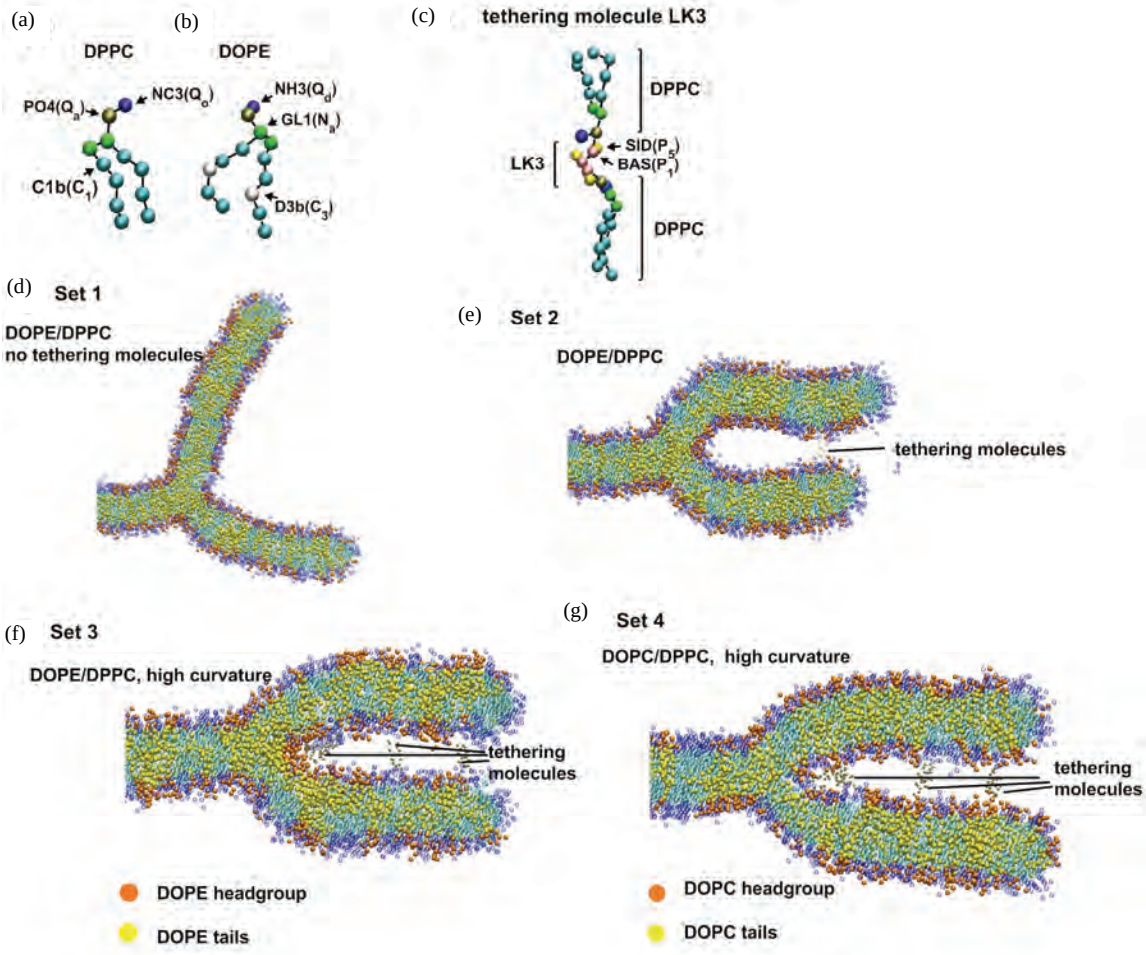

Figure 2. The CG model of lipids and representative snapshots of the simulations. (a) The CG model of DPPC; (b) The CG model of DOPE; (c) The CG model of the tethering molecule. Shown here is LK3 along with DPPC. For (a)-(c), particle name (e.g., NC3) and type (e.g., Q_o) used are indicated; (d)-(g) Representative snapshots obtained from the simulations. (d) Set 1, the simulations of DPPC/DOPE membrane without the tethering molecule; (e) Set 2, the DPPC/DOPE membrane simulated with the tethering molecules restrained at 12nm from the center of the circle C1 defined in **Figure 1**; (f) Set 3, the DPPC/DOPE with the tethering molecules used at three different positions; (g) Set 4, the DOPC/DPPC with the tethering molecules at the same positions as in (f). For (d)-(g) the leftmost part of the λ membrnae is hidden; this part consists of the DPPC molecules whose com was restrained to reduce the large drift of membranes. The representation scheme for (d)-(g): blue spheres, DPPC headgroup particles (from NC3 to GL2); light blue spheres, DPPC hydrophobic tail particles; orange spheres, DOPE (or DOPC) headgroup particles; yellow spheres, DOPE hydrophobic tail particles; gray spheres, particles representing the tethering molecules.

membrane. For the initial structure, a membrane of DPPC was prepared and, subsequently, an appropriate number of DPPC chosen randomly were replaced with DOPE. Four water molecules were modeled by one particle as in [29]. For all λ simulations 11423 water particles were used. A typical size of the simulation box was 31, 4.5, 16 (nm) in x-, y-, and z-direction respectively. The artificial tethering (crosslinking) molecules that tether the *cis* monolayers were CG-modeled peptides consisting of three ("LK3") or six ("LK6") Ser residues (**Figure 2(c)**). As in [30,31], the peptide backbone was represented by the P1 particle while the Ser sidechain was represented by P5. Each tethering molecule was attached to the PO4 particle of two DPPC molecules each contained in each of the *cis* (fused) monolayers (**Figure 2(c)**). When the tethering molecules were used (*i.e.*, set 2-4 in **Table 1**), their center of mass (com) positions were harmonically restrained; for example, for sets 3 and 4, the four LK3 were restrained at a position 4 nm (along the x-direction) from the center of the circle C1 (see **Figure 1(g)**), whereas the two LK6 were restrained at 6nm and two more LK6 were restrained at 8nm from

Table 1. Outer leaflet curvature and DOPE (DOPC) distribution in the curved and planar regions.

set	θ (degree)	*C4_radius* (nm)	DOPE fraction (%) ± s.d		n
			curved region	planar regions	
1	130.4 ±6.5	3.48 ± 0.36	38.2 ± 2.15	34.6 ± 0.10	2
2	82.6 ± 3.7	1.34 ± 0.07	37.8 ± 0.45	39.1 ± 2.05	2
3	73.3 ± 0.6	0.99 ± 0.02	62.6 ± 5.50	37.8 ± 5.10	4
			DOPC fraction (%)		
4	72.8 ± 3.68	1.01 ± 0.07	42.5 ± 6.59	35.1 ± 2.74	4

Set 1-3 are DOPE/DPPC simulations, where the overall DOPE fraction, DOPE / (DOPE+DPPC) = 34.5%. For set 4, the DOPC content was also 34.5%. s.d was calculated from the n average values, each of which was computed from the last 400ns period of each trajectory; n is the number of simulation runs (*i.e.*, trajectories).

the C1 center. For the remaining part of the λ-membrane, a harmonic restraint was applied to the com of each tethering molecule.

Nonbonded interactions are described by a Lennard-Jones potential [29]. In addition, the charged particles interact via a Coulombic energy function with a relative dielectric constant = 15, which represents screening effect. The cut-off lengths and the switching function were set as in [29]. Gromacs (ver 3.3) was used [32] for 500 ns simulations performed at 323 K with the time step of 20 fs and with semi-isotropic pressure coupling at 1bar. Due to the increased diffusion rate of molecules with the CG system [29], in the following we show the time after the 4-fold multiplication. The pressure coupling time constant was 0.2 ps and the compressibility set at 3×10^{-5} bar^{-1}.

3. RESULTS

Four sets of simulations, each consisting of two to five independent 2000ns simulations, were performed (**Table 1**). For sets 1-3, the DOPE/DPPC membranes were used, whereas for set 4 the DOPC/DPPC membrane was used. **Table 1** shows the average (± s.d.) of the mean values (each obtained from the final 400 ns of each trajectory) of θ, the C4 radius and the DOPE (or DOPC) density in the curved region and planar regions. For all these results the s.d. was small, which was not surprising because the 1600 ns pre-run allowed sufficient equilibration time. When no tethering molecule was used (set 1), the three bilayers quickly became equivalent (at ~400 ns); the angle between any two bilayers equally approached 120 degree (**Figure 2(d)**). The DOPE density relative to DPPC became similar between the curved and the planar regions (**Table 1**, set 1). Note that the enrichment of DPPC at the edge, generally increased the DOPE fraction above the nominal 34.5%.

When two LK3 molecules were used for tethering at 12nm from the C1 center, and the C4 radius decreased, indicating negative curvature. However, the outer leaflet had horseshoe-like roundness (**Figure 2(e)**). In this case, the DOPE accumulation in the negatively curved region was not significant (**Table 1**).

When the number of tethering molecules was increased and some positioned close to the junction (as described in the above section), the higher curvature was maintained (**Figure 2(f)**). Then, the significant enrichment in DOPE was observed for the negatively curved region compared to the planar region (set 3) ($p < 0.01$; *t*-test). In contrast, when the DOPE molecules of the DOPE/DPPC membrane (set 3) were all replaced with DOPC (set 4, **Figure 2(g)**), the DOPC density in the negatively curved region was lower than the density of DOPE of set 3 simulations ($p < 0.05$).

6000 ns simulations of simple planar bilayers of the same compositions as above were performed as a pilot analysis and, for the final 400ns, the radial distribution function (rdf) of the lipids were examined. The planar bilayers made up of 512 lipid molecules in total were used. The DOPE density in the proximity (~0.5-1 nm) of each DOPE molecule was high, indicating that the DOPE-DOPE interaction was stronger than DOPE-DPPC interaction, which, in turn was slightly stronger than DPPC-DPPC interaction (**Figures 3(a)** and **(b)**). The DOPC-DOPC interaction was as weak as the DOPC-

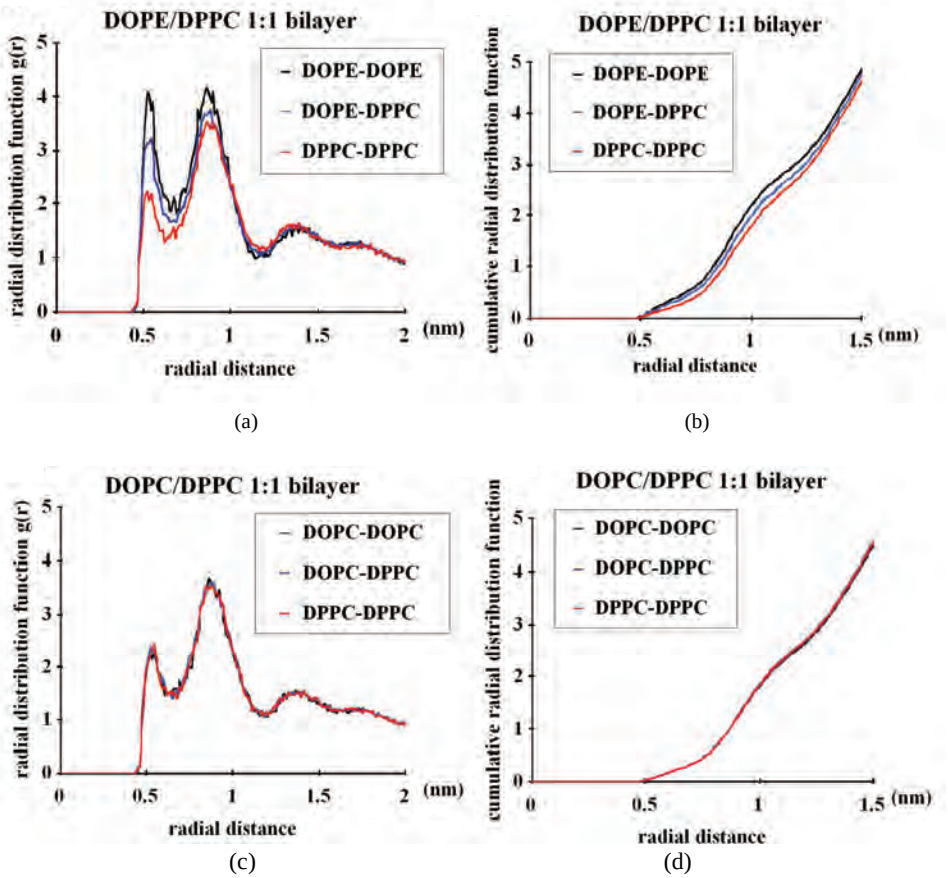

Figure 3. Radial distribution function (rdf) analyses of the CG lipids used in this study. 6000ns pilot simulations with planar bilayers composed of 512 lipid molecules were performed and the last 400ns data were used for this analysis. (a) DOPE/DPPC 1:1 membrane; (b) Same as (a) but the cumulative rdf is shown; (c) DOPC/DPPC 1:1 membrane; (d) Same as (c) but the cumulative rdf is shown. For example, the "DOPE-DOPE" curve shows the density (relative to the density over the whole system) of the DOPE NH3 particle at the indicated distance from each DOPE NH3 particle. Similarly, the DOPE-DPPC curve shows the density of DPPC NC3 around DOPE NH3, whereas DOPC-DPPC shows the DPPC NC3 density around DOPC NC3.

DPPC interaction and the DPPC-DPPC interaction (**Figures 3(c)** and **(d)**). Therefore, for the CG model used, the between-headgroups interaction determines the lateral distribution in planar bilayers, whereas the between-acyl chains interaction is not important. We also note that the DOPE-DOPE interaction is very local and there is no lipid clustering on scales greater than ~1 nm; in fact, at >2 nm from each DOPE molecule the density of DOPE is the same as that of DPPC (**Figure 3(a)**). Therefore, the DOPE and DPPC membrane is not demixed; only subtle enrichment in DOPE occurs in the close proximity (~0.5-1 nm) of each DOPE molecule. While we cannot rule out the possibility that further demixing of DOPE from DPPC could take place in longer simulations, there was no significant difference in the rdf results between the ~1000 ns and ~5600 ns data (details not shown), suggesting that the DOPE/DPPC planar bilayer was equilibrated earlier than 5600 ns.

4. DISCUSSION AND PERSPECTIVES

Above we showed that with the use of tethering molecules that maintain highly negative curvature, DOPE accumulates in the negatively curved monolayer region of the DOPE/DPPC membranes. Accumulation was significantly less when DOPC molecules were used in place of DOPE. Radial distribution function of a pilot analysis using a planar bilayer showed a modest level (~1.3 fold compared with DPPC) of enrichment in DOPE ~0.5 nm from each DOPE molecule (**Figure 3(a)**), which represents the direct contact of DOPE headgroups with each other. No phase separation was observed in the planar

DOPE/DPPC membrane until the end of the simulation (6000 ns).

While these results may be of physicochemical relevance, several questions remain in terms of membrane physiology. First, biological relevance of the tethering molecules is unclear; in the real fusion, proteins are generally large, likely making the curvature of the fused monolayers lower than our setting (e.g., [33,34]; and references cited therein). However, in a cell fusion study using SNARE proteins expressed on the cell surface, it has been shown that GPI (glycerophosphatidylinositol)-anchored EYFP (Enhanced Yellow Fluorescent Protein consisting of 239 amino acid residues) does not diffuse between hemifused cells whereas GPI-anchored short peptide (named GPI-AU1) does (Figure 7 of [35]). In the latter case, the negative curvature between the fused monolayers may be so high that membrane proteins with a large ectodomain are excluded from the between-cell diffusion.

Second, results with the 2D-curvature system have to be carefully interpreted; our 2D-curvature system is obviously different from a small hemifusion diaphragm having a saddle-like (*i.e.*, high Gaussian) curvature between the fused monolayers [24]. It should also be remembered that, while a large hemifusion diaphragm is observed especially with a high PE fraction, it is possible that the hemifusion diaphragm may not be a major intermediate in the fusion pathway of physiologic membranes [36,37].

It still seems relevant to ask why theoretical and *in vitro* experimental studies show only a weak degree of curvature sorting of lipids, despite *in vivo* evidence arguing for the curvature sorting effects that support cellular activities [5,6,38]. As several authors have suggested, the lateral interaction between lipids may have a profound impact on the efficacy of curvature sorting. The question arises then, how such lipid-lipid interactions modulate the lipid partitioning into differently curved membrane portions. This question may be considered based on two scenarios. First, a strong lipid-lipid interaction increases the effective area of the lipid molecule. For example, if DOPE favors interaction with DOPE, but not with DPPC, this leads to lipid sorting and can be regarded as an increase in the effective molecule area of both DOPE and DPPC. The second scenario is that the sorting can be based on the bending stiffness [19,39]. Once the curvature facilitates phase segregation in the membrane close to a demixing point, relatively soft and rigid domains may be generated. While soft domains can move into highly curved regions, rigid domains favor locations in the relatively flat regions.

Consider the first scenario. How does the increase in molecule area (surface area per molecule) influence curvature sorting. In the study employing tube pulling, a model considering individual molecule curvature sorting based on spontaneous curvature has been proposed [19,39]. For a membrane consisting of lipids α and β, based on the assumption of equal chemical potentials of molecule α (and β), on tether and vesicle, the authors have derived the following relationship:

$$k_c a (C - C_{st} + C_{sv}) (C_\beta - C_\alpha) = kT \ln (\phi_{\alpha ov} / \phi_{\alpha ot}) + kT \ln (\phi_{\beta ot} / \phi_{\beta ov}), \quad (1)$$

where, k_c is the bending stiffness, a is the molecule area, $C = 1/R_t$ is the tube curvature (with R_t being the tube radius), C_{st} and C_{sv} are the spontaneous curvature of the outer monolayer of the tube and the vesicle, respectively, k is the Bolzmann constant, $\phi_{\alpha ov}$, for example, is the mole fraction of molecule in the outer leaflet of the vesicle. **Eq.1** is derived via the partial differentiation of the total energy function by $N_{\alpha ot}$, which is the number of molecule in the outer monolayer of the tube. The left side of **Eq.1** corresponds to the potential regarding the bending energy, whereas the right side corresponds to the entropy term. The weighted average spontaneous curvature is assumed to be $C_{st} = (C_\alpha N_{\alpha ot} + C_\beta N_{\beta ot}) / N_{ot}$, where C_α is the spontaneous curvature of molecule α. Our λ system can be considered similarly; the curved region corresponds to the tube, while the planar regions correspond to the vesicle. Let α represent DOPE and β represent DPPC. Let $\phi_{\alpha ov} = 0.38$, $\phi_{\alpha ot} = 0.63$ (set 3), $C_\alpha = -0.3$ nm^{-1} [25]. The remaining terms may be approximated as: $k_c = 4 \times 10^{-20}$ J [25]; $C = -1.0$ nm^{-1}; $C_{st} = -0.19$ nm^{-1}; $C_{sv} = -0.11$ nm^{-1}; $C_\beta = \sim 0$ nm^{-1}; $kT = \sim 4 \times 10^{-21}$ J. These values lead to $a = \sim 0.4$ nm^2, smaller than the real value for the CG system (0.64 nm^2 and 0.66 nm^2 for DPPC and DOPE respectively). This may be because C_α and C_β for the CG-model of DOPE and DPPC are not known and also our definition of C and the curved region may not be suitable.

The above relationship helps to infer the impact of molecule area. For example, if the DOPE-DOPE interaction and the DPPC-DPPC interaction are greater than the DOPE-DPPC interaction so that DOPE and DPPC behave, on average, as a particle with a 1.5-fold effective molecular area, then this would increase the fraction of DOPE in the curved region from 0.63 to ~0.75. (Here, $N_{ov} >> N_{ot}$ was assumed.) The reality should be far more complex, yet this notion supports the view [20] that individual lipids have a small molecular area compared with transmembrane proteins or lipid clusters, and therefore, although some lipids have high spontaneous curvatures, the membrane curvature preference of these lipids is weak.

In the second scenario, where lipid sorting is based on rigidity or bending stiffness, the effect of cholesterol on membrane properties is likely to be important. After the detergent resistant membrane domains known as rafts

were identified as important membrane structural components in signal transduction and in the sorting of proteins and lipids [40,41], the effects of cholesterol on the phase properties of phospholipid bilayers were studied [42]. The cholesterol/saturated/unsaturated lipid mixture has a dramatically strong tendency toward phase separation compared with the binary mixture lacking cholesterol [15]. In addition, different fluid phases may have different bending stiffness. The L_d region (consisting of sphingomyelin and cholesterol) has a higher bending stiffness k_c value compared with the L_o phase [14]. While our analyses do not take into account the k_c difference between the membrane regions, this difference may be important in the case of cholesterol-containing mixtures as considered in [19,39]. Another intriguing finding regarding cholesterol segregation is that cholesterol accumulates in high curvature regions in a membrane composed of brominated di18:0 PC/cholesterol 2:1 [43].

Characterization of cholesterol-containing membranes is a topic of computational research. Several groups conducted atomistic simulations and showed several features such as hydrogen bond formation between cholesterol and phospholipids, which are consistent with experimental findings [44,45]. In general, the simulations supported the consensus that cholesterol interacts with phospholipid molecules and gives rise to the intermediate level of organization in lipid membranes, L_o [46]. (In the L_o phase, lipid hydrocarbon chains are ordered as in a L_c gel state, but phospholipid molecules are nearly as mobile as in a L_α fluid phase [47], for review see [41]). In terms of domain formation, Vattulainen and coworkers used a coarse-grained model and showed the formation of cholesterol-rich and cholesterol-poor domains at intermediate cholesterol concentrations [48,49]. Recently, Risselada and Marrink [50] showed that the CG model can reproduce the experimental findings on the formation of distinct phases (L_o and L_d (liquid-disordered) phase). The lateral organization of cholesterol of the raft-like structure in [50] resembles that derived from the atomistic preassembled raft-like mixtures [51]. The necessity of cholesterol for the phase separation has also been shown in [50]; in the absence of cholesterol, the DPPC/diC18:2-PC 3:1 mixture exhibited nonrandom (nonideal) mixing, yet macroscopic phase separation did not occur. From this finding, and also considering the choice of 323K in our system, it seems unlikely that the phase separation occurs in our DOPE/DPPC planar bilayer even when the simulation is extended longer than 6000ns. Future simulation analyses could focus on the phase separation in curved regions, especially those containing the stalk or the rim of the hemifusion diaphragm. As stated above, curvature sorting is significant only when the lipid mixture is close to the demixing point and therefore the ternary complex (cholesterol/saturated lipid/unsaturated lipid) may well be examined.

Computational lipid sorting analyses also have implications in peptide-lipid interaction. Although our atomistic simulations have recently shown that an influenza virus HA2 fusion peptide enhances the rate of stalk formation [52], it is yet unknown whether such fusion peptides associate with and stabilize a particular lipid domain or, more positively, draw particular types of lipid, creating a domain in the proximity of the peptide, thereby modulating the fusion rate. (The fusion peptide was also studied in recent atomistic simulations of vesicle fusion [53]). One difficulty is the limitation in the simulation time; atomistic simulations typically cover 10-100ns and therefore very subtle lipid sorting cannot be studied with this approach.. This problem may be partially remedied by using initial structures based on the ones obtained from well equilibrated CG simulations. Phase separation simulation in [50] may provide an important framework for analyses of interactions between peptides and lipid domains.

Another interesting problem in membrane fusion is the mechanism by which transmembrane (TM) peptide domains control the fusion. Findings from Langosch and other researchers ([54] and references cited therein) generally argue that, while the ectodomains (hydrophilic domains located between the *cis* membranes) of fusion proteins are important in stalk formation and/or in the hemifusion intermediate, TM domains play a crucial role in later steps of fusion, such as, the rupture of the hemifusion diaphragm and/or pore formation. Considering the practical difficulties in computation (*i.e.*, system size and simulation time), it is hoped that 2D-curved membrane systems such as ours will provide a useful starting point for such peptide analyses.

5. CONCLUSIONS

DOPE enrichment in a negatively curved region was observed in the CG models of the DOPE/DPPC monolayer mimicking the monolayer that would occur upon the fusion of the proximal monolayers. Enrichment was insignificant for DOPC in the DOPC/DPPC monolayer simulated similarly, suggesting the promoting effect of headgroup interaction between DOPE molecules on curvature sorting. Artificial tethering molecules that kept the negative curvature high (R = ~1 nm) were necessary for significant accumulation of DOPE. No phase separation was observed in the DOPE/DPPC membrane simulated as a planar bilayer. It is envisaged that, in a more physiological environment in which cholesterol is contained and is close to a demixing point, the membrane

curvature could exert more pronounced lipid sorting than the one shown in this study.

6. ACKNOWLEDGEMENTS

This work was supported by Grant-in-Aid for Scientific Research from the Ministry of Education, Culture, Sports, Science, and Technology of Japan.

REFERENCES

[1] Holthuis, J.C. and Levine, T.P. (2005) Lipid traffic: Floppy drives and a superhighway. *Nature Reviews Molecular Cell Biology*, **6(3)**, 209-220.

[2] Van Meer, G., Voelker, D.R. and Feigenson, G.W. (2008) Membrane lipids: Where they are and how they behave. *Nature Reviews Molecular Cell Biology*, **9(2)**, 112-124.

[3] De Matteis, M.A. and Luini, A. (2008) Exiting the Golgi complex. *Nature Reviews Molecular Cell Biology*, **9(4)**, 273-284.

[4] Mukherjee, S., Soe, T.T. and Maxfield, F.R. (1999) Endocytic sorting of lipid analogues differing solely in the chemistry of their hydrophobic tails. *Journal of Cell Biology*, **144(6)**, 1271-1284.

[5] Van Meer, G. and Lisman, Q. (2002) Sphingolipid transport: Rafts and translocators. *Journal of Biological Chemistry*, **277(29)**, 25855-25858.

[6] Ostrowski, S.G., Van Bell, C.T., Winograd, N. and Ewing, A.G. (2004) Mass spectrometric imaging of highly curved membranes during Tetrahymena mating. *Science*, **305(5680)**, 71-73.

[7] Fratti, R.A., Jun, Y., Merz, A.J., Margolis, N. and Wickner, W. (2004) Interdependent assembly of specific regulatory lipids and membrane fusion proteins into the vertex ring domain of docked vacuoles. *Journal of Cell Biology*, **167(6)**, 1087-1098.

[8] Helfrich, W. (1973) Elastic properties of lipid bilayers: Theory and possible experiments. *Zeitschrift fur Naturforschung C*, **28(11)**, 693-703.

[9] Markin, V.S. (1981) Lateral organization of membranes and cell shapes. *Biophysical Journal*, **36(1)**, 1-19.

[10] Kozlov, M.M. and Helfrich, W. (1992) Effects of a cosurfactant on the stretching and bending elasticities of a surfactant monolayer. *Langmuir*, **8(11)**, 2792-2797.

[11] Seifert, U. (1993) Curvature-induced lateral phase segregation in two-component vesicles. *Physical Review Letters*, **7(9)**, 1335-1338.

[12] Iglic, A., Hägerstrand, H., Veranic, P., Plemenitas, A. and Kralj-Iglic, V. (2006) Curvature-induced accumulation of anisotropic membrane components and raft formation in cylindrical membrane protrusions. *Journal of Theoretical Biology*, **240(3)**, 368-373.

[13] Derganc, J. (2007) Curvature-driven lateral segregation of membrane constituents in Golgi cisternae. *Physical Biology*, **4(4)**, 317-324.

[14] Baumgart, T., Hess, S.T. and Webb, W.W. (2003) Imaging coexisting fluid domains in biomembrane models coupling curvature and line tension. *Nature*, **425(6960)**, 821-824.

[15] Radhakrishnan, A. and McConnell, H. (2005) Condensed complexes in vesicles containing cholesterol and phospholipids. *Proceedings of the National Academy of Sciences of the United States of America*, **102(36)**, 12662-12666.

[16] Parthasarathy, R., Yu, C.H. and Groves, J.T. (2006) Curvature-modulated phase separation in lipid bilayer membranes. *Langmuir*, **22(11)**, 5095-5099.

[17] Bo, L. and Waugh, R.E. (1989) Determination of bilayer membrane bending stiffness by tether formation from giant, thin-walled vesicles. *Biophysical Journal*, **55(3)**, 509-517.

[18] Roux, A., Cuvelier, D., Nassoy, P., Prost, J., Bassereau, P. and Goud, B. (2005) Role of curvature and phase transition in lipid sorting and fission of membrane tubules. *European Molecular Biology Organization Journal*, **24(8)**, 1537-1545.

[19] Tian, A. and Baumgart, T. (2009) Sorting of lipids and proteins in membrane curvature gradients. *Biophysical Journal*, **96(7)**, 2676-2688.

[20] Kamal, M.M., Mills, D., Grzybek, M. and Howard, J. (2009) Measurement of the membrane curvature preference of phospholipids reveals only weak coupling between lipid shape and leaflet curvature. *Proceedings of the National Academy of Sciences of the United States of America*, **106(52)**, 22245-22250.

[21] Cooke, I.R. and Deserno, M. (2006) Coupling between lipid shape and membrane curvature. *Biophysical Journal*, **91(2)**, 487-495.

[22] Chernomordik, L.V., Melikyan, G.B. and Chizmadzhev, Y.A. (1987) Biomembrane fusion: A new concept derived from model studies using two interacting planar lipid bilayers. *Biochimica et Biophysica Acta*, **906(3)**, 309-352.

[23] Tamm, L.K., Crane, J. and Kiessling, V. (2003) Membrane fusion: A structural perspective on the interplay of lipids and proteins. *Current Opinion in Structural Biology*, **13(4)**, 453-466.

[24] Chernomordik, L.V. and Kozlov, M.M. (2008) Mechanics of membrane fusion. *Nature Structural & Molecular Biology*, **15(7)**, 675-683.

[25] Marsh, D. (2006) Elastic curvature constants of lipid monolayers and bilayers. *Chemistry and Physics of Lipids*, **144(2)**, 146-159.

[26] Fuller, N. and Rand, R.P. (2001) The influence of lysolipids on the spontaneous curvature and bending elasticity of phospholipid membranes. *Biophysical Journal*, **81(1)**, 243-254.

[27] Marrink, S.J. and Mark, A.E. (2003) The mechanism of vesicle fusion as revealed by molecular dynamics simulations. *Journal of American Chemical Society*, **125(37)**, 11144-11145.

[28] Kasson, P.M., Kelley, N.W., Singhal, N., Vrljic, M., Brunger, A.T. and Pande, V.S. (2006) Ensemble molecular dynamics yields submillisecond kinetics and intermediates of membrane fusion. *Proceedings of the National Academy of Sciences of the United States of America*, **103(32)**, 11916-11921.

[29] Marrink, S.J., Risselada, H.J., Yefimov, S., Tieleman, D.P. and De Vries, A.H. (2007) The MARTINI force field: Coarse grained model for biomolecular simulations. *Journal of Physical Chemistry B*, **111(27)**, 7812-7824.

[30] Bond, P.J. and Sansom, M.S.P. (2006) Insertion and assembly of membrane proteins via simulation. *Journal of the American Chemical Society*, **128(8)**, 2697-2704.
[31] Bond, P.J., Holyoake, J., Ivetac, A., Khalid, S. and Sansom, M.S.P. (2007) Coarse-grained molecular dynamics simulations of membrane proteins and peptides. *Journal of Structural Biology*, **157(3)**, 593-605.
[32] Lindahl, E., Hess, B. and Van der Spoel, D. (2001) GROMACS 3.0: A package for molecular simulation and trajectory analysis. *Journal of Molecular Modeling*, **7(8)**, 306-317.
[33] Weissenhorn, W., Hinz, A. and Gaudin, Y. (2007) Virus membrane fusion. *FEBS Letters*, **581(11)**, 2150-2155.
[34] Wickner, W. and Schekman, R. (2008) Membrane fusion. *Nature Structural & Molecular Biology*, **15(7)**, 658-664.
[35] Giraudo, C.G., Hu, C., You, D., Slovic, A.M., Mosharov, E.V., Sulzer, D., Melia, T.J. and Rothman, J.E. (2005) SNAREs can promote complete fusion and hemifusion as alternative outcomes. *Journal of Cell Biology*, **170(2)**, 249-260.
[36] Liu, T., Wang, T., Chapman, E.R. and Weisshaar, J.C. (2008) Productive hemifusion intermediates in fast vesicle fusion driven by neuronal SNAREs. *Biophysical Journal*, **94(4)**, 1303-1314.
[37] Kasson, P.M. and Pande, V.S. (2007) Control of membrane fusion mechanism by lipid composition: Predictions from ensemble molecular dynamics. *PLoS Computational Biology*, **3(11)**, 2228-2238.
[38] Van Meer, G. and Sprong, H. (2004) Membrane lipids and vesicular traffic. *Current Opinion in Cell Biology*, **16(4)**, 373-378.
[39] Tian, A., Capraro, B.R., Esposito, C. and Baumgart, T. (2009) Bending stiffness depends on curvature of ternary lipid mixture tubular membranes. *Biophysical Journal*, **97(6)**, 1636-1646.
[40] Edidin, M. (2003) The state of lipid rafts: From model membranes to cells. *Annual Review of Biophysics and Biomolecular Structure*, **32(1)**, 257-283.
[41] Jacobson, K., Mouritsen, O.G. and Anderson, R.G. (2007) Lipid rafts: At a crossroad between cell biology and physics. *Nature Cell Biology*, **9(1)**, 7-14.
[42] Mannock, D.A., Lewis, R.N., McMullen, T.P. and McElhaney, R.N. (2010) The effect of variations in phospholipid and sterol structure on the nature of lipid-sterol interactions in lipid bilayer model membranes. *Chemistry and Physics of Lipids*, **163(6)**, 403-448.
[43] Wang, W., Yang, L. and Huang, H.W. (2007) Evidence of cholesterol accumulated in high curvature regions: Implication to the curvature elastic energy for lipid mixtures. *Biophysical Journal*, **92(8)**, 2819-2830.
[44] Chiu, S.W., Jakobsson, E., Mashl, R.J. and Scott, H.L. (2002) Cholesterol-induced modifications in lipid bilayers: A simulation study. *Biophysical Journal*, **83(4)**, 1842-1853.
[45] Hofsäss, C., Lindahl, E. and Edholm, O. (2003) Molecular dynamics simulations of phospholipid bilayers with cholesterol. *Biophysical Journal*, **84(4)**, 2192-2206.
[46] Pandit, S.A., Khelashvili, G., Jakobsson, E., Grama, A. and Scott, H.L. (2007) Lateral organization in lipid-cholesterol mixed bilayers. *Biophysical Journal*, **92(2)**, 440-447.
[47] McMullen, T.P. and McElhaney, R.N. (1995) New aspects of the interaction of cholesterol with dipalmitoylphosphatidylcholine bilayers as revealed by high-sensitivity differential scanning calorimetry. *Biochimica et Biophysica Acta*, **1234(1)**, 90-98.
[48] Murtola, T., Falck, E., Patra, M., Karttunen, M. and Vattulainen, I. (2004) Coarse-grained model for phospholipid/cholesterol bilayer. *Journal of Chemical Physics*, **121(18)**, 9156-9165.
[49] Murtola, T., Karttunen, M. and Vattulainen, I. (2009) Systematic coarse graining from structure using internal states: Application to phospholipid/cholesterol bilayer. *Journal of Chemical Physics*, **131(5)**, (055101)1-15.
[50] Risselada, H.J. and Marrink, S.J. (2008) The molecular face of lipid rafts in model membranes. *Proceedings of the National Academy of Sciences of the United States of America*, **105(45)**, 17367-17372.
[51] Niemelä, P.S., Ollila, S., Hyvönen, M.T., Karttunen, M. and Vattulainen, I. (2007) Assessing the nature of lipid raft membranes. *PLoS Computational Biology*, **3(2)**, 304-312.
[52] Nishizawa, M. and Nishizawa, K. (2010) Molecular dynamics simulation analyses of viral fusion peptides in membranes prone to phase transition: Effects on membrane curvature, phase behavior and lipid-water interface destabilization *Journal of Biophysical Chemistry*, **1(1)**, 19-32.
[53] Kasson, P.M., Lindahl, E. and Pande, V.S. (2010) Atomic-resolution simulations predict a transition state for vesicle fusion defined by contact of a few lipid tails. *PLoS Computational Biology*, **6(6)**, e1000829.
[54] Langosch, D., Hofmann, M. and Ungermann, C. (2007) The role of transmembrane domain in membrane fusion. *Cellular and Molecular Life Sciences*, **64(7-8)**, 850-864.

Vol.1, No.2, 96-104 (2010)
doi:10.4236/jbpc.2010.12012

Journal of Biophysical Chemistry

Identification of potential *P. falciparum* transketolase inhibitors: pharmacophore design, *in silico* screening and docking studies

Shweta Joshi[1], Alok Ranjan Singh[1], Uzma Saqib[2], Prakash Chandra Misra[3], Mohammad Imran Siddiqi[2], Jitendra Kumar Saxena[1*]

[1]Division of Biochemistry, Central Drug Research Institute, Council of Scientific and Industrial Research, Lucknow, India; *Corresponding Author: jkscdri@yahoo.com
[2]Division of Molecular and Structural Biology, Central Drug Research Institute, Lucknow, India
[3]Department of Biochemistry, Lucknow University, Lucknow, India

Received 2 June 2010; revised 26 July 2010; accepted 2 August 2010.

ABSTRACT

Transketolase, the most critical enzyme of the non-oxidative branch of the pentose phosphate pathway, has been reported as a novel target in *Plasmodium falciparum* as it has least homology with the human host. Homology model of *P. falciparum* transketolase (PfTk) was constructed using the crystal structure of *S. cervisiae* transketolase as a template, and used for the identification and prioritization of potential compounds targeted against Plasmodium falciparum transketolase. The docking studies with fructose-6-phosphate and thiamine pyrophosphate showed that His^{31}, Asp^{473}, Ser^{388}, Arg^{361} and His^{465} formed hydrogen bonds with fructose-6-phosphate while pyrimidine ring of coenzyme interacted with conserved residues of protein viz., Leu^{121}, Glu^{415}, Gly^{119}. The major interacting residues involved in binding of oxythiamine pyrophosphate were similar to cofactor binding site of PfTk. An integrated pharmacophore, co-factor ThDP and substrate fructose-6-phosphate, based virtual screening of a small molecule database retrieved eight and thirteen compounds respectively. When screened for their activity against *P. falciparum* transketolase, one compound in case of ThDP and three compounds in case of fructose-6-phosphate based screening were found active against PfTk. Identification of these novel and chemically diverse inhibitors provides initial leads for optimization of more potent and efficacious drug candidates to treat malarial infection.

Keywords: *Plasmodium Falciparum* Transketolase; Thiamine Pyrophosphate; Fructose-6-Phosphate; Docking; Virtual Screening; Pharmacophore

1. INTRODUCTION

The thiamine diphosphate (ThDP) dependent enzyme transketolase (Tk; D-sedoheptulose-7-phosphate: D-glyceraldehyde-3-phosphate glycolaldehydetransferase, EC 2.2.1.1.) catalyzes the cleavage of a carbon-carbon bond adjacent to a carbonyl group in keto sugars and transfers a ketol moiety to aldosugar. Transketolase is the most critical enzyme of the non-oxidative branch of the pentose phosphate pathway (PPP) which provides ribose molecule, an essential metabolite in nucleic acid production. In addition, the ribose necessary for the abnormal proliferation of tumor cells is provided via the nonoxidative branch of the pentose phosphate pathway [1]. Transketolase plays a key role in tumor cell proliferation, neurodegenerative diseases, diabetes and cancer [1-3]. The inhibitors of transketolase are also used in the treatment of cancer [4].

The mechanism of action of transketolase has been mediated by its cofactor thiamine pyrophosphate (ThDP), which is coordinated to divalent metal ions [5,6]. However, drugs targeting the active site of transketolase, by acting as cofactor analogs, have poor activity and low selectivity over other thiamine dependent enzymes such as pyruvate dehydrogenase. Oxythiamine [7] or thiamine thiazolone diphosphate [8] are typical examples of this kind of inhibitor and thus they do not have any pharmacological application.

A lot of work has been devoted on the yeast (*Saccharomyces cerevisiae*), *Escherichia coli* and maize transketolases and their structures have been solved by X-ray diffraction [9-13] revealing important aspects of

the functional flexibility, metabolic profile and substrate binding. The homodimeric yeast transketolase is composed of three distinct domains: the N-terminal, middle and C-terminal domains [10,11]. Recently, Cristian *et al*. [14] reported the homology model of human transketolase and proposed that five critical sites containing arginines contribute to dimer stability.

However, scant attention has been focused on the *Plasmodium falciparum* transketolase protein. This enzyme in *P. falciparum* is a novel drug target as it shows least homology with the human host. Recently we have cloned, expressed and characterized transketolase from *P. falciparum* [15]. We have also identified two potent inhibitors of PfTk, i.e, p-hydroxyphenyl pyruvate and oxythiamine pyrophosphate, which have shown good *in-vivo* anti-malarial activity against the rodent malarial parasite *P. yoelii* (unpublished data). In this regard, it would be useful to determine the structure of *P. falciparum* transketolase in order to conduct further research into structure-based drug design. In our previous studies, we have proposed the model of *P. falciparum* transketolase, using the 3D structure of the yeast variant as a template and then performing a homology modelling which is subsequently refined through molecular dynamic simulations [15]. In the present study, this homology model of PfTk was used to study the binding properties of cofactor, substrate and inhibitors by docking these ligands in the cofactor and substrate binding sites of PfTk model. The information obtained on optimization of binding of substrate and cofactor was utilized in pharmacophore search of CDRI's 3D compound database to identify a new compound with similar geometry.

2. MATERIALS AND METHODS

2.1. Construction of *P. Falciparum* Transketolase Homodimer

The structure of PfTk was constructed by homology modelling using the Modeller program [16] interfaced with Insight II 2000.1 [17]. MODELLER is a general program that implements comparative protein structure modelling by satisfying spatial restraints in terms of probability density functions [16,18]. To this end, the homodimer crystal structure of the *S. cerevisiae* yeast transketolase (pdb code 1TRK) was used as a 3D template. Although the other variants, such as the *E. coli* transketolase or the maize transketolase, show similar sequence identity to the *P. falciparum* protein, but the yeast variant was chosen because more information is available about its structure and properties. Finally, the stereochemical evaluations of the model were performed with the program PROCHECK v 3.4.4 [19].

2.2. Molecular Docking

Three-dimensional structure of fructose-6-phosphate, thiamine pyrophosphate (ThDP) and oxythiamine pyrophosphate (OP) were constructed using the SYBYL7.1 suite of programs (TRIPOS Inc. 1699; South Hanley Road, St. Louis, M.O., 63144, USA) running under Irix 6.5. These ligands were docked into the active site of PfTk using the FlexX program interfaced with SYBYL7.1. FlexX program is a fast algorithm for the flexible docking of small ligands into fixed protein binding sites using an incremental construction process that considers ligand conformational flexibility (FlexX version 1.13.5, Saint Augustin, Germany, Bioselvel T, GmbH). The binding site regions for the Flex docking simulations of these ligands were specified based on the previously reported structure information of *S. cerevisiae* Tk and *E. coli* Tk [11,20,21]. The proposed interaction modes of fructose-6-phosphate with substrate binding site, and thiamine pyrophosphate & oxythiamine pyrophosphate with ThDP binding site were determined with FlexX score.

2.3. Virtual Screening

Binding property of fructose-6-phosphate to substrate binding site and thiamine pyrophosphate to ThDP binding site of PfTk was used for the generation of pharmacophore model. The pharmacophore model was derived by means of a feature based query derived on the basis of critical binding interactions of the ligands. This pharmacophore model was used to perform a flexible pharmacophore search of a subset of inhouse 3D compound database (5784 compounds) of Central Drug Research Institute (C.D.R.I.) to identify hits that satisfy the chemical and geometrical requirements using UNITY module of SYBYL7.1.

2.4. Purification of PfTk

The expression and purification of recombinant PfTk was carried out as described earlier [15]. PfTk was over-expressed in *E. coli* strain Rosetta (DE3) harboring the plasmid TOPOT7-PfTk. Cells were grown in Luria Bertani (L.B.) broth with 40 µg/ml chloramphenicol and 100 µg/ml ampicillin and induced with 1 mM isopropyl *β*-thiogalactopyranoside (IPTG). Cultures were then grown at 18°C for 20 h before harvest. Cells were harvested by centrifugation at 8000 × *g* for 10 min at 4°C. Protein was purified using Ni-nitrilotriacetic acid agarose affinity chromatography and ammonium sulphate precipitation. For the preparation of apo-PfTk the purified PfTk was extensively dialyzed against the buffer (50 mM NaH_2PO_4 and 300 mM NaCl) containing 10 mM EDTA [22].

2.5. Biological Screening

Activity was measured spectrophotometrically according to the method of Kochetov [23]. For the screening of compounds having homology with fructose-6-phosphate, the reaction mixture in 1 ml contained, 50 mM glycyl-glycine buffer (pH 7.6), 2 mM magnesium chloride, 0.1 mM thiamine pyrophosphate (ThDP), 0.5 mM potassium ferricyanide, 3 mM fructose-6-phosphate (F6P) and 0.24 mg enzyme protein in the absence and presence of 200 µM concentration of compound to be screened. For screening of compounds, having homology with thiamine pyrophosphate, apo-PfTk was incubated with the compound (200 µM) at room temperature in the presence of all constituents (50 mM glycyl-glycine buffer pH 7.6, 2 mM magnesium chloride, 3 mM fructose-6-phosphate) except the coenzyme i.e., thiamine pyrophosphate (ThDP). After incubation for 20 min, ThDP (0.01 mM) was added and initial activities were measured.

3. RESULTS

3.1. Homology Model of *P. Falciparum* Transketolase

S. cerevisiae Tk sequence having highest sequence homology of 50 % with PfTk sequence was used as a template for modeling of PfTk. The constructed model was *in silico* dimerized using the dimeric variant of yeast transketolase for further docking and virtual screening studies. The PfTk model is an average structure based on restraints derived from the coordinate sets of the template (**Figure 1(a)**). In our previous studies, we have already reported that similar to the *S. cereviseae* transketolase, PfTk model can also be divided into N-terminal, middle and C-terminal domains [15]. The superposition of PfTk homology model on template also revealed close structural resemblance of modelled PfTk (**Figure 1(b)**). Refinement of the homology model removed the steric constraints and obtained stable conformation by energy minimization of 1000 iterations. After the refinement process, the model was validated using PROCHECK program [19]. The Ramachandran plot [24] showed normal distribution of points with phi (Φ) values and psi (ψ) values clustered in a few distinct regions with 87.5 and 11.7 % of residues occupying core and allowed regions, respectively. Only a few residues (0.2 %) were in the disallowed regions (data not shown).

3.2. Docking Studies

Docking studies not only provide an understanding of the binding mode of the ligands but are also employed to validate homology models. The molecular models for

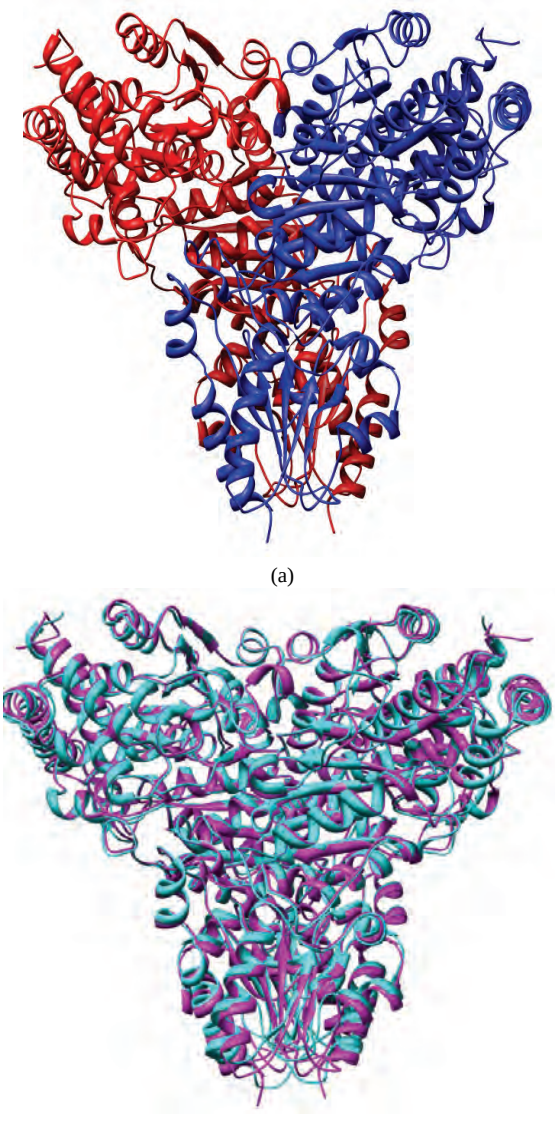

(a)

(b)

Figure 1. (a) Dimeric model structure of PfTk. Model structure of PfTk built on the basis of homologue transketolase of *S. cerevisiae* (ID: 1TRK, 2.0 Å resolution) [11]. In the model, (a) chain is colored red and (b) chain is colored blue; (b) Superposition of PfTk (cyan) with *S. cereviseae* model (magenta).

fructose-6-phosphate, thiamine pyrophosphate and oxythiamine pyrophosphate with PfTk were generated by SYBYL7.0/FlexX docking module. Among the 30 docked poses for each ligand, one with the highest dock score was chosen as the final conformation.

3.2.1. Docking of Fructose-6-Phosphate

Most of the residues in the PfTk binding pocket are polar in nature and hence make several hydrogen binding interactions with the ligand. Hence, when fructose-6-phosphate was docked into substrate binding site of PfTk,

most of the important active site residues like His[31], Asp[473], Ser[388], Arg[361] and His[465] showed hydrogen binding interactions with fructose-6-phosphate (**Figure 2(a)**).

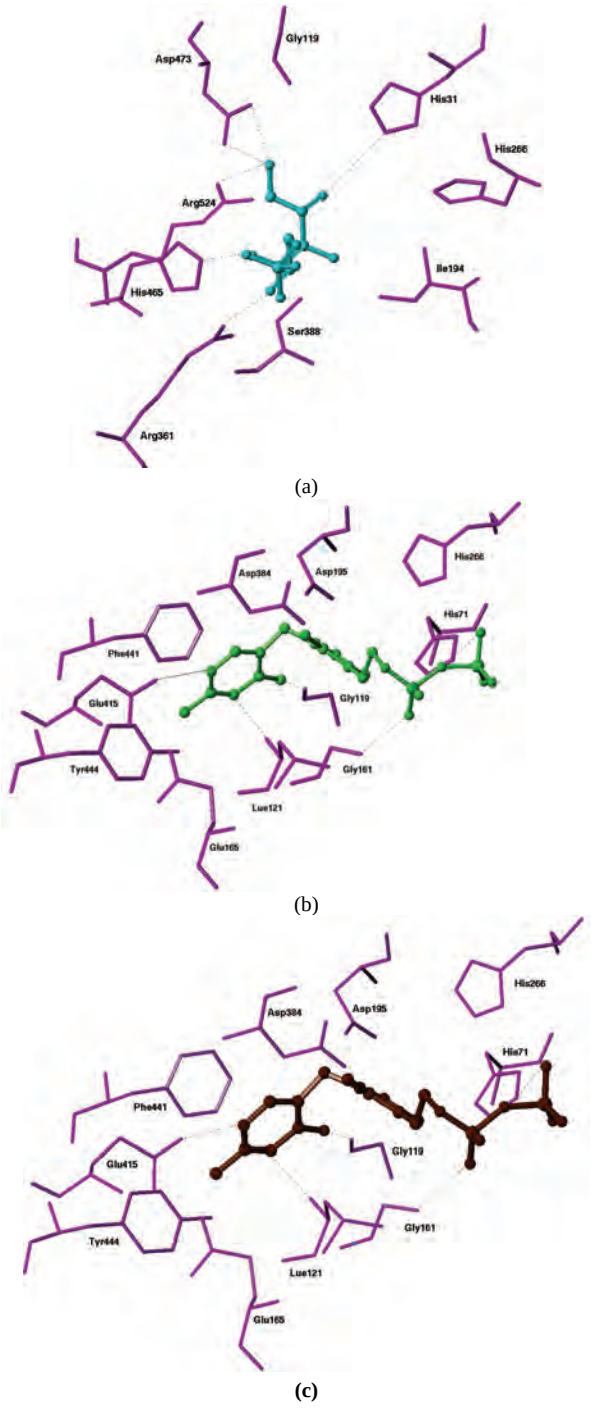

Figure 2. Docking of ligands into active site of PfTk: (a) Docking of fructose-6-phosphate into substrate binding site of PfTk; (b) & (c) represents the docking of thiamine pyrophosphate and oxythiamine pyrophosphate into ThDP binding site of PfTk. These ligands were docked in to their respective sites using the FlexX program interfaced with SYBYL7.1.

The total docking energy in the form of FlexX score was calculated to be –34.36 KJ/mole.

3.2.2. Docking of Thiamine Pyrophosphate

When thiamine pyrophosphate was docked into ThDP binding site of PfTk, the pyrimidine ring of the coenzyme interacts with the conserved residues of the protein, e.g. N3' of coenzyme with Leu[121], N-1' with Glu[415]; 4'NH_2 with Gly[119] (**Figure 2(b)**). The binding site for TPP is characterized by a number of hydrophobic interactions including the pi-pi stacking interactions with Phe[441], Phe[444] and the phenyl ring of ThDP were important for ligand binding. The total FlexX dock score was calculated as –25.37 KJ/mole.

3.2.3. Docking of Oxythiamine Pyrophosphate

When oxythiamine pyrophosphate was docked into ThDP binding site of PfTk, the major interacting residues were found to be similar as observed for thiamine pyrophosphate. Similar to ThDP, the N3' of pyrimidine ring of OP interacts with Leu[121], N-1' with Glu[415] and 4'NH_2 with Gly[119] (**Figure 2(c)**). Being a homolog of thiamine pyrophosphate, oxythiamine pyrophosphate, also displays similar mode of binding in terms of hydrophobic interactions involved. Similarly, no difference was observed in the binding energy of OP as compared to ThDP which is –25.29 KJ/mole**.**

3.3. Virtual Screening

A subset of CDRI repository comprising of 5784 were selected on the basis of their activity in enzyme based and cell based assay under various drug discovery programs. We have employed a virtual screening protocol based on two 3D database screening approaches: 1) pharmacophore hypothesis based 3-D database search and 2) protein structure based docking approach. Firstly, a simple ligand based pharmacophore model on the basis of binding property of fructose-6-phosphate with substrate binding site of PfTk and thiamine pyrophosphate with ThDP binding site of PfTk was developed. The model obtained from query based on critical binding interactions of the ligands was used to perform a pharmacophore search of 3D compound database to identify hits that satisfy the chemical and geometrical requirements using UNITY module of SYBYL7.1. The pharmacophore query used for fructose-6-phosphate consists of five acceptor points, one donor atom with distance as well as spatial constraints (**Figure 3(a)**). While the ThDP pharmacophore query consists of five acceptor atoms, one donor atom and hydrophobic feature with distance constraints (**Figure 3(b)**).

In the first step of virtual screening, the compound with unfavorable physicochemical and pharmacokinetic properties was filtered out, based on a modified Lipin-

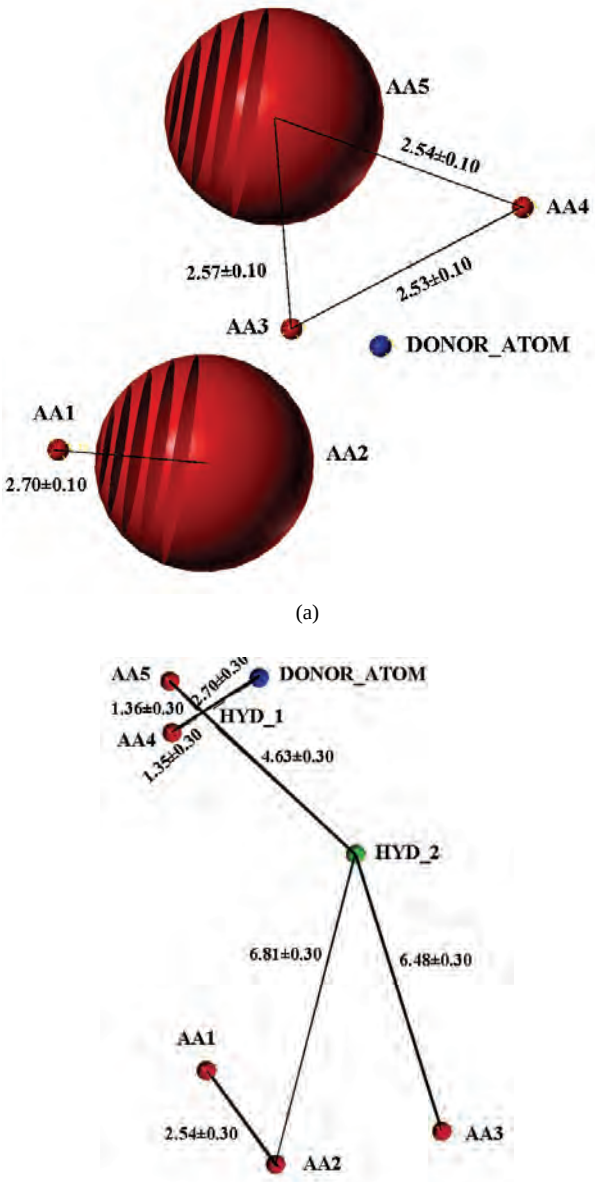

Figure 3. Diagramatic representation of pharmacophore query based on (a) fructose-6-phosphate and (b) thiamine pyrophosphate.

ski's rule of 5 [25]. Virtual screening with UNITY using ligand based pharmacophore model and employing Lipinski's rule of 5 yielded 42 hits in case of virtual screening based on ThDP while 36 hits were obtained on the basis of fructose-6-phosphate based virtual screening. Finally, protein structure based molecular docking was used to dock each hit into the active site of PfTk and to rank the binding affinities. FlexX [26] based molecular docking study was carried out to perform scoring and ranking of the hits obtained in database searching. All the hits obtained in database searching and FlexX score [27], were visually analyzed for their associations with the active site of PfTk and the capability to form hydrogen bond interaction with catalytic residues. At the final stage, 8 molecules in case of ThDP docking and 13 molecules in case of F6P docking which showed promising docking affinities in scoring method and a good binding mode in accordance with our pharmacophoric definition were retrieved from CDRI small molecule repository. These molecules were then subjected to biological evaluation. The flow chart of virtual screening based on fructose-6-phosphate and thiamine pyrophosphate is shown in **Figures 4(a)** & **(b)** respectively.

3.4. Biological Screening of Active Compounds

The eight compounds selected after virtual screening on the basis of ThDP and thirteen compounds obtained after screening on the basis of fructose-6-phosphate were further screened biologically as described in Materials and Methods. Our results indicated that one compound in case of ThDP based screening and three compounds in case of fructose-6-phosphate based screening were found active against PfTk (**Tables 1** & **2**). Maximum inhibition was achieved in presence of compound I and II, which showed 45% and 41% inhibition, respectively at 200 μM concentrations.

3.5. Docking of Active Compounds

The three virtual screening hits retrieved by the pharma-

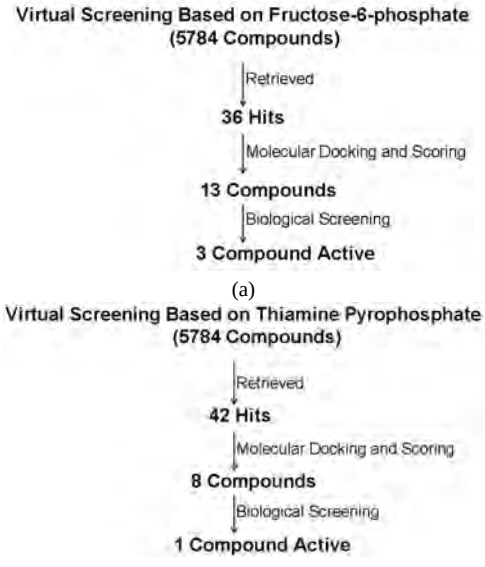

Figure 4. Flow chart indicated the results obtained from virtual screening of a CDRI small molecules database. (a) represents the virtual screening based on fructose-6-phosphate; (b) represents the virtual screening based on ThDP. The numbers given in figure represent the number of molecules selected after each stage.

cophoric query based on fructose-6-phosphate, showed almost all the major interactions as observed for F6P, like Asp[473], Arg[524], Ser[388], Arg[361] etc (**Figures 5(a)-(c)**).

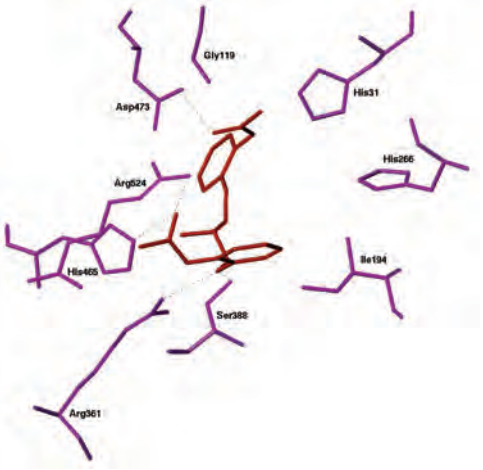

(a)

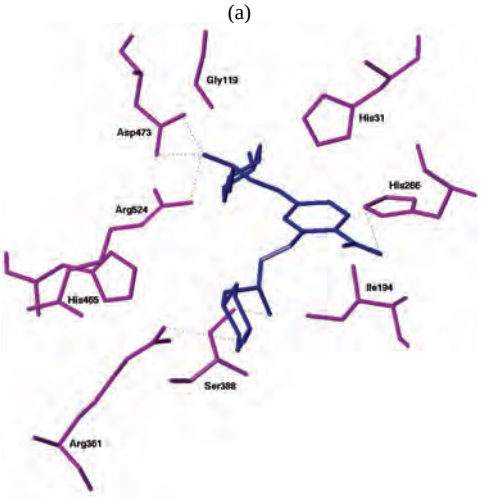

(b)

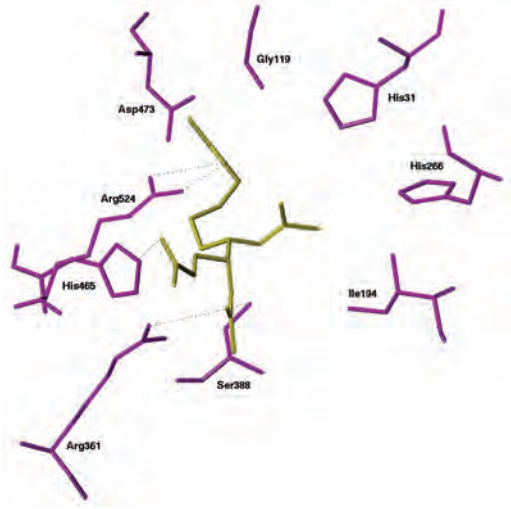

(c)

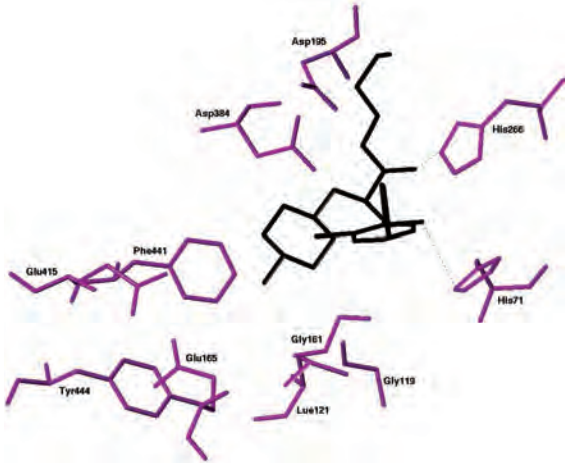

(d)

Figure 5. Binding mode of potential hits in PfTk model. (a) Compound I; (b) Compound II; (c) Compound III; (d) Compound IV.

Table 1. Inhibition of PfTk by compound obtained after screening on the basis of Thiamine pyrophosphate.

Compound	M.W.	Structure	Concentration	% Inhibition
1. Oxythiamine pyrophosphate (control)	338	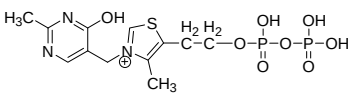	50 µM 100 µM 200 µM	40 ± 1.2 59 ± 2.7 74 ± 3.1
2. Compound IV	437	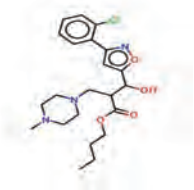	50 µM 100 µM 200 µM	N.I. 22 ± 1.8 37 ± 2.2

Table 2. Inhibition of PfTk by compounds obtained after screening on the basis of Fructose-6-phosphate.

Compound	M. W.	Structure	Concentration	% Inhibition
1. p-hydroxyphenylpyruvate (control)	180	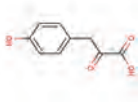	50 µM 100 µM 200 mM	25 ± 1.9 42 ± 2.3 56 ± 2.9
2. Compound I	358	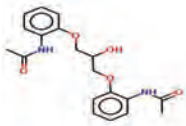	50 µM 100 µM 200 µM	22 ± 0.8 37 ± 1.1 45 ± 3.2
3. Compound II	466	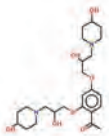	50 µM 100 µM 200 µM	14 ± 1.6 33 ± 1.3 41 ± 2.6
4. Compound III	311	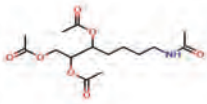	50 µM 100 µM 200 µM	N.I. 14 ± 2.2 34 ± 2.5

Similarly compound IV, the finally selected compound from virtual screening hits based on cofactor ThDP, though did not show some of the H-bond interactions but due to the presence of various hydrophobic (Gly^{161}, Gly^{119}) and π- π stacking interactions (Phe^{441}, Phe^{444}) has acquired a stable conformation within the binding site (**Figure 5(d)**).

4. DISCUSSION

Virtual screening is an emerging technology that is gaining an increased role in the drug discovery process [28,29]. The technology involves analyzing large collection of compounds and leading it to smaller subsets for biological testing. It is now perceived as a complementary approach to experimental screening (High-throughput screening) and when coupled with structural biology promises to enhance the probability of success in the lead identification stage of drug discovery process. Structure based virtual screening requires computational fitting of compound into an active site of a receptor by use of sophisticated algorithm, followed by scoring and ranking to these compounds to identify potential leads.

In the present study, a homology model of PfTk was built on the basis of crystal structure of transketolase of *S. cereviseae* [11]. This homology model was then used for docking studies which not only provided an understanding of the binding mode of ligands but also validated homology model. When fructose-6-phosphate was docked into substrate binding site of PfTk the major interacting residues were similar to that obtained in case of crystal structure of *E. coli* transketolase complexed with fructose-6-phosphate [21]. The docking of thiamine pyrophosphate into ThDP binding site showed similar interactions as observed in case of *S. cereviseae* [11]. The docking of oxythiamine pyrophosphate in to the ThDP binding site of PfTk revealed its similar mode of binding as that of ThDP.

Virtual screening is a computational technique used in drug discovery research involving the rapid *in silico* assessment of large libraries of chemical structures in order to identify those structures most likely to bind a drug target, typically a protein receptor or enzyme [30,31]. The available CDRI compound library comprising nearly 5784 compounds were screened *in silico* for homology model of PfTk to identify structurally diverse *Plasmodium falciparum* transketolase inhibitors. The report provides an example of optimum utilization of computational resources implementing stepwise docking strategy for virtual screening. Out of which, 8 compounds from ThDP based screening and 13 compounds obtained from F6P based screening were finally screened biologically. Among these, 4 compounds were identified as inhibitors of PfTk. All four compounds inhibited the enzyme activity at 200 µM concentration. Among these, compounds I and II were found to be specific as they showed 45 and 41% inhibition, respectively. Identification of these novel and chemically diverse inhibitors provides initial leads for optimization into more potent and efficacious drug candidates to treat malarial infection. Further in *vitro* screening of these inhibitors, design and synthesis of their analogs is in progress.

5. ACKNOWLEDGEMENTS

We gratefully acknowledge the Council of Scientific and Industrial Research (CSIR), New Delhi, for offering Junior and Senior Research fellowships to Shweta Joshi to carry out this work. We would like to extend our gratitude to Dr. T. K. Chakroborty, Director, CDRI for his invaluable support. The manuscript communication number is 7876.

REFERENCES

[1] Comín-Anduix, B., Boren, J., Martinez, S., Moro, C., Centelles, J.J., Trebukhina, R., Petushok, N., Lee, W.N., Boros, L.G. and Cascante, M. (2001) The effect of thiamine supplementation on tumour proliferation. A metabolic control analysis study. *European Journal of Biochemistry*, **268(15)**, 4177-4182.

[2] Mazzola, J.L. and Sirover, M.A. (2004) Subcellular analysis of aberrant protein structure in age-related neurodegenerative disorders," *Journal of Neuroscience Methods*, **137(2)**, 241-246.

[3] Saito, N., Kimura, M., Kuchiba, A. and Itokawa, Y. (1987) The relationship between blood thiamine levels and dietary thiamine content in diabetic outpatients and healthy subjects. *Journal of Nutrition Science Vitaminology*, **33(6)**, 431-438.

[4] Rais, B., Comin, B., Puigjaner, J., Brandes, J.L., Creppy, E., Saboureau, D., Ennamany, R., Lee, W.N.P., Boros, L.G. and Cascante, M. (1999) Oxythiamine and dihydroepiandrosterone induce a G1 phase cycle arrest in Eherlich's tumor cells through inhibition of the pentose cycle. *FEBS Letters*, **456(1)**, 113-118.

[5] Shreve, D.S., Holloway, M.P., Haggerty, J.C. III and Sable, H.Z. (1993) The catalytic mechanism of transketolase. Thiamin pyrophosphate-derived transition states for Transketolase and pyruvate dehydrogenase are not identical. *Journal of Biological Chemistry*, **258(20)**, 12405-12408.

[6] Schellenberger, A. (1992) Thiamin pyrophosphate binding mechanism and the function of the aminopyrimidine part. *Journal of Nutritional Science and Vitaminology* (*Tokyo*), 392-396.

[7] Boros, L.G., Puigjaner, J., Cascante, M., Lee, W.N., Brandes, J.L., Bassilian, S., Yusuf, F.I., Williams, R.D., Muscarella, P., Melvin, W.S. and Schirmer, W.J. (1999) Oxythiamine and dehydroepiandrosterone inhibit the non-oxidative synthesis of ribose and tumor cell proliferation. *Cancer Research*, **57(19)**, 4242-4248.

[8] Nilsson, U., Lindqvist, Y., Kluger, R. and Schneider, G. (1993) Crystal structure of Transketolase in complex with thiamine thiazolone diphosphate, an analogue of the reaction intermediate, at 2.3A˚ resolution. *FEBS Letters*, **326(3)**, 145-148.

[9] Wikner, C., Nilsson, U., Meshalkina, L., Udekwu, C., Lindqvist, Y. and Schneider, G. (1997) Identification of catalytically important residues in yeast Transketolase. *Biochemistry*, **36(50)**, 15643-15649.

[10] Lindqvist, Y., Schneider, G., Ermler, U. and Sundstrom, M. (1992) Three-dimensional structure of transketolase, a thiamine diphosphate dependent enzyme, at 2.5 Å resolution. *European Molecular Biology Organization Journal*, **11(7)**, 2373-2379.

[11] Nikkola, M., Lindqvist, Y. and Schneider, G. (1994) Refined structure of transketolase from *Saccharomyces cerevisiae* at 2.0A˚ resolution. *Journal of Molecular Biology*, **238(3)**, 387-404.

[12] Isupov, M.N., Rupprecht, M.P., Wilson, K.S., Dauter, Z. and Littlechild, J.A. Crystal Structure of *Escherichia coli* Transketolase. In press.

[13] Gerhardt, S., Echt, S., Busch, M., Freigang, J., Auerbach, G., Bader, G., Martin, W.F., Bacher, A., Huber, R. and Fischer, M. (2003) Structure and properties of an engineered transketolase from maize. *Plant Physiology*, **132(4)**, 1941-1949.

[14] Obiol-Pardo, C. and Rubio-Martinez, J. (2009) Homology modelling of human Transketolase: Description of critical sites useful for drug design and study of the cofactor binding mode. *Journal of Molecular Graphics and Modelling*, **27(8)**, 723-734.

[15] Joshi, S., Singh, A.R., Kumar, A., Misra, P.C., Siddiqi, M.I. and Saxena, J.K. (2008) Molecular cloning and characterization of *Plasmodium falciparum* transketolase. *Molecular and Biochemical Parasitology*, **160(1)**, 32-41.

[16] Sali, A. and Blundell, T.L. (1993) Comparative protein modeling by satisfaction of spatial restraints. *Journal of Molecular Biology*, **234(3)**, 779-815.

[17] Accelrys Inc. (2001) Insight II 2000.1 program. Accelrys Inc., San Diego.

[18] Fiser, A., Do, R.K. and Sali, A. (2000) Modeling of loops in protein structures. *Protein Science*, **9(9)**, 1753-1773.

[19] Laskowski, R.A., MacArthur, M.W., Moss, D.S. and Thornton, J.M. (1993) PROCHECK: a program to check the stereochemical quality of protein structures. J*ournal of Applied Crystallography*, **26(2)**, 283-291.

[20] Nilsson, U., Meshalkina, L., Lindqvist, Y. and Schneider, G. (1997) Examination of substrate binding in thiamine diphosphate dependent transketolase by protein crystallography and site-directed mutagenesis. *Journal of Biological Chemistry*, **272(3)**, 1864-1869.

[21] Asztalos, P., Parthier, C., Golbik, R., Kleinschmidt, M., Hübner, G., Weiss, M.S., Friedemann, R., Wille, G. and Tittmann, K. (2007) Strain and near attack conformers in enzymic thiamin catalysis: X-ray crystallographic snapshots of bacterial transketolase in covalent complex with donor ketoses xylulose 5-phosphate and fructose 6-phosphate, and in noncovalent complex with acceptor aldose ribose 5-phosphate. *Biochemistry*, **46(43)**, 12037-12052.

[22] Wood, T. and Fletcher, S. (1978) The affinity chromatography of transketolase. *Biochemica Biophysica Acta*, **527(1)**, 249-255.

[23] Kochetov, G.A. (1982) Determination of transketolase activity via ferricyanide reduction. *Methods in Enzymology*, **89**, 43-44.

[24] Edsall, J.T., Flory, P.J., Kendrew, J.C., Liquori, A.M., Nemethy, G., Ramachandran, G.N. and Scheraga, H.A. (1996) A proposal of standard conventions and nomenclature for the description of polypeptide conformations. *Journal of Molecular Biology*, **15(4)**, 399-407.

[25] Lipinski, C.A., Lombardo, F., Dominy, B.W. and Feeney, P.J. (2001) Experimental and computational approaches to estimate solubility and permeability in drug discovery

and development settings. *Advances in Drug Delivery Review*, **46(1-3)**, 3-26.

[26] Kramer, B., Rarey, M. and Lengauer, R. (1999) Evaluation of the FlexX incremental construction algorithm for protein ligand docking. *Proteins*: *Structure*, *Function and Genetics*, **37(2)**, 228-241.

[27] Rarey, M., Kramer, B., Lengauer, T. and Klebe, G. (1996) A fast flexible docking method using an incremental construction algorithm. *Journal of Molecular Biology*, **261(3)**, 470-489.

[28] Abagyan, R. and Totrov, R. (2001) High throughput docking for lead generation. *Current Opinion in Chemical Biology*, **5(4)**, 375-382.

[29] Bissantz, C., Folkers, G. and Rognan, D. (2000) Protein based virtual screening of chemical databases 1. Evaluation of different docking/scoring combinations. *Journal of Medicinal Chemistry*, **43(25)**, 4759-4767.

[30] Rester, U. (2008) From virtuality to reality-virtual screening in lead discovery and lead optimization: A medicinal chemistry perspective. *Current Opinion in Drug Discovery & Development*, **11(4)**, 559-568.

[31] Rollinger, J.M., Stuppner, H. and Langer, T. (2008) Virtual screening for the discovery of bioactive natural products. *Progress in Drug Research*, **65(211)**, 213-249.

Vol.1, No.2, 105-112 (2010)
doi:10.4236/jbpc.2010.12013

Journal of Biophysical Chemistry

Structure-activity correlationship and folding of recombinant *Escherichia coli* dihydro folate reductase (DHFR) enzyme through biochemical and biophysical approaches

Jai Mittal[1*], Gayathri Ravitchandirane[1*], Tapan K. Chaudhuri[1], Pratima Chaudhuri (Chattopadhyay)[2]**

[1]Department of Biochemical Engineering and Biotechnology, Indian Institute of Technology Delhi, Delhi, India; *Both authors contributed equally to the work
[2]Amity Institute of Biotechnology, Amity University, Noida, India; **Corresponding Author: pratimachaudhuri@yahoo.com

Received 5 June 2010; revised 9 July 2010; accepted 15 July 2010.

ABSTRACT

The design of any antagonist or inhibitor for any enzyme requires the knowledge of structure-function relationship of the protein and the optimum conformational states for maximum and minimum activities. Furthermore, designing of the inhibitors or drugs against an enzyme becomes easier if there is information available about various well characterized intermediate conformation of the molecule. In vivo folding pathway of any recombinant protein is an important parameter for understanding its ability to fold by itself inside the cell, which always dictates the downstream processing for the purification. In the present manuscript we have discussed about the in vivo and in vitro folding, and structure-function relationship of Dihydrofolate reductase enzyme. This is an important enzyme involved in the cell growth and hence inhibition or inactivation of the enzyme may reduce the cell growth. It was observed that the equilibrium unfolding transition of DHFR proceeds through the formation of intermediates having higher exposed surface hydrophobicity, unchanged enzymatic activity and minimum changes in the secondary structural elements. Because of enhanced surface hydrophobicity, and unchanged enzymatic activity, these intermediates could be a nice target for designing drugs against DHFR.

Keywords: Cellular Folding of *E. coli* DHFR; Structure-Function Relationship; Conformational Properties; Equilibrium Unfolding Transitions; Pathways for Denaturation and Renaturation

1. INTRODUCTION

Proteins are one of the most common and important cellular macromolecules, which control almost all biological processes. Every protein acquires a unique three-dimensional conformation in order to be functionally effective. As unfolded polypeptides contain many more exposed hydrophobic residues than the polypeptide in their native state, they are exquisitely susceptible to aggregation. Also any small error in the process of folding produces misfolded structure, which becomes a cellular burden and is responsible for several misfolding disorders such as Alzheimer's disease, Type II Diabetes, Parkinson's disease and several others that are threatening human lives [1].

It is quite common that majority of over expressed recombinant proteins fail to reach a correct conformation and undergo proteolytic degradation or associate with each other to form insoluble aggregates of non native proteins known as inclusion bodies. Hence, there is a growing interest in developing strategies to prevent protein aggregation, to enhance protein refolding yields.

Dihydrofolatereductase (DHFR; 5,6,7,8-tetrahydrofolate: NADP+ oxidoreductase) (a 24 kDa protein) catalyzes the NADPH-dependent reduction of dihydrofolate (H_2folate) or folic acid to tetrahydrofolate (H_4folate) and is considered to be a key enzyme in folate metabolism. H_2folate is the product of thymidylate synthetase and must be recycled to H_4folate in order to be incorporated into tetrahydrofolate metabolic pool. After reduction of H_2folate, H_4folate receives one carbon unit and acts as a one-carbon donor in the biosynthesis of purines and pyrimidines and in the interconversion of amino acids [2]. Tetrahydrofolate acts as a methyl group shuttle required for the de novo synthesis of purines, thymidylic acid, and certain amino acids.

As tetrahydrofolate, the product of this reaction is the active form of folate in humans, inhibition of DHFR can cause functional folate deficiency. Folate is needed by rapidly dividing cells to make thymine, this effect may be therapeutic. For example, methotrexate is used in cancer chemotherapy because it can prevent neoplastic cells from dividing.

So, DHFR has become very important nowadays in making anti-cancer drugs due to its inhibition by methotrexate. Its binding to methotrexate depends on its conformation, so it is very necessary that it should be present in its correctly folded form.

In the present manuscript, cellular folding of *E. coli* DihydrofolateReductase (DHFR), unfolding and refolding pathways, and structure activity relationship of the protein have been demonstrated with the help of experimental findings using biochemical and biophysical approaches.

2. MATERIALS AND METHODS

2.1. Reagents and Chemicals

The gene for *E. coli* DihydrofolateReductase (DHFR), cloned in the pET16b vector was obtained from Taguchi and UEDA group, The University of Tokyo, Japan. pET16b vector contains T7 promoter region and genes for ampicillin resistance, so specially engineered *E. coli* strain, BL21(DE3) was used for transformation of plasmid, expressing DHFR. BL21(DE3) cells contain the machinery for production of T7 RNA polymerase. Isopropyl *β*-D-1-thiogalactopyranoside (IPTG) was used as the inducer, as genes for T7 RNA polymerase were under lac promoter in BL21 DE3 strain. The ampicillin concentration used for optimum growth of the cells was 80 µg/ml. Isopropyl *β*-D-1-thiogalactopyranoside (IPTG), ampicillin, Luria broth media from Himedia (India), Dihydro folic acid, NaDH, Imidazole are from Sigma chemical company (USA), Hitrap chelating column from GE Health care (USA). All other reagents were of molecular Biology grade.

2.2. Over-Expression of DHFR

Competent *E. coli* BL21 DE3 cells were prepared according to the $CaCl_2$ method given by Sambrook and Russell [3]. The cells were transformed with pET16b vector containing DHFR and spread on a LB agar plate containing ampicillin. The culture of the selected transformed *E. coli* colonies was grown at 37°C, with agitation at 200 rpm and induced with IPTG (final concentration 1 mM) at OD_{600} of 0.85. The cells were further incubated for 12-14 h for DHFR expression. About 200 µl of culture was centrifuged and the pellet was re-suspended in SDS loading dye [3,4], boiled at 100°C for five minutes and loaded on a 12 % SDS-PAGE for confirming DHFR expression.

BL21 (DE3) cells transformed with pDHFR plasmid were induced by 1 mM IPTG and different samples were collected after incubation of 3 hrs, 6 hrs, 9 hrs and 12hrs. The samples were denatured by boiling with SDS sample buffer and were run into SDS-PAGE and over-expression of the protein was judged from the band intensity in the gel.

2.3. *In Vivo* Folding of DHFR

Amount of folded protein in a cell can be estimated based on the principle that the proteins with correctly folded structure are soluble in the cytoplasm and in aqueous buffer, however, denatured proteins are insoluble and occur as aggregates [5]. Thus, to estimate the extent of correct folding of DHFR *in vivo*, culture broth of transformed strain expressing DHFR were harvested and resuspended in lysis buffer containing 20mM sodium phosphate (pH 7.0), 500mM NaCl. Normalization of the cell culture was done such that the same number of cells was taken for the analysis of each sample along with the control (un-induced cells). These cells were disrupted using ultrasonicator, followed by centrifugation at 10,000 rpm for 30 min. The supernatants and pellets were separated and were resuspended in the SDS loading dye, heated at 100°C for 5 minutes and analyzed by SDS-PAGE.

2.4. Purification of DHFR Using Immobilized Metal Ion Affinity Chromatography (IMAC)

Purification of DHFR was carried out by Immobilized Metal Ion Affinity Chromatography (IMAC) using chelating column charged with nickel ions as recombinant DHFR contained six Histidine residues on the N terminal. Plasmid pET16b containing DHFR gene was used for over-expression of DHFR. Cells were grown at 37°C and induced with 1 mM IPTG at OD_{600} = 0.90. After induction, further incubation was carried out at 37°C for 12 hr and the cells were harvested by centrifugation at 10,000 rpm for 30 min. Expression of DHFR was confirmed by analysis on 12% SDS-PAGE. Harvested cells were re-suspended in lysis buffer containing 20 mM sodium phosphate (pH 7.0), 500mM NaCl and 5µl of DNAse I, PMSF (final concentration, 1 mM) and 5 µl of 0.01 M $MgCl_2$ were added followed by incubation for 30 min on ice. The re-suspended cells were disrupted by 3 passes through French press at 13000 psi. Cell debris was removed by centrifugation in Beckman ultracentrifuge at 13,000 rpm for 40 min at 4°C. The supernatant was collected and filtered through a 0.22 micron filter. Nickel chelating column (Histrap, 5 ml, GE Health Care,

USA) was cleaned and pre-treated according to the manufacturer's instructions. The column was then equilibrated with buffer A1 (20 mM sodium phosphate (pH 7.0), 500 mM NaCl). The clear lysate was applied for chromatographic process by AKTA FPLC system (GE Health care, USA). Buffer A1 was passed through the system for three column volumes. Then the column was washed with 2% buffer B1 for two column volumes. Elution of DHFR was done by passing buffer B1 (500 mM imidazole in buffer A1). The fractions corresponding to the peaks for DHFR were analysed by SDS PAGE. These fractions were pooled and concentrated by Amicon centrifugation kit, 10 kDa cut-off membranes (Millipore). Concentrated DHFR solution was divided in aliquots, frozen in liquid nitrogen and stored at –80°C.

2.5. Protein Estimation Using Bradford's Reagent

Protein was estimated by the Bradford's dye binding method using bovine serum albumin as the standard protein. 500 µl of appropriately diluted protein was taken in a test tube. 4.5 ml of Bradford's reagent was added to it. The mixture was incubated at room temperature for 10 min and the concentration of the protein was determined from the colour development, measured spectro-photometrically at 595 nm.

2.6. Enzymatic Activity Assay of DHFR

DHFR activity was determined by the fact that it catalyses the following reaction:

$$DHF + NADPH + H^+ \rightarrow THF + NADP^+ \quad [6]$$

where, DHF and THF are dihydrofolate and tetrahydrofolate, repectively. The decrease in NADPH was monitored by measuring its absorbance at 340 nm at 37°C. The reaction was initiated by DHFR. The standard assay mixture (1.0 ml) contained 3 M KCI in phosphate/Cit. (25 mM citrate, 25 mM phosphate titrated to pH 6 by KOH), 0.05 mM dihydrofolic acid and 0.08 mM NADPH. An enzyme unit is defined as the amount of enzyme that catalyzes the oxidation of 1 mol NADPH/ min. This value was calculated from the changes with time in the optical absorption at 340 nm, using the value 12300 $M^{-1}cm^{-1}$ [7] as combined molar absorption coefficients for the oxidation of the NADPH and the subsequent reduction of the dihydrofolate.

2.7. Equilibrium Unfolding Studies by Intrinsic Tryptophan Fluorescence Spectroscopy

For equilibrium unfolding studies, intrinsic fluorescence measurements were performed using Perkin-Elmer LS 55 spectrofluorimeter using an optical cuvette of pathlength1cm. Samples were prepared by incubating DHFR (final conc. 1 µM) with different concentrations of GdnHCl (0-4 M) at 25ºC for 30 min in 10mM sodium cacodylate, 50 mM NaCl buffer, pH 7.4. The samples were excited at 295 nm and emission spectra were recorded between 310-500 nm with excitation and emission slit width 5 nm each. The quantity 'relative fluorescence' was calculated accordingly:

$$F_R = (F - F_0)/F_0$$

where, F is the fluorescence intensity of the protein at various GdnHCl conc. F_0 is the fluorescence intensity of the native protein. F_R was plotted against GdnHCl concentration.

2.8. Equilibrium Unfolding Studies by Circular Dichroism

Far-UV CD spectra were recorded on JASCO J-810 CD polarimeter (JASCO, Japan), flashed with nitrogen gas, using an optical cuvette of pathlength 2 mm. Samples were prepared by incubating DHFR (final conc. 10µM) with different concentrations of GdnHCl (0-4M) at 25 ºC for 30 min in 10 mM sodium cacodylate, 50mM NaCl buffer, pH 7.4. Each spectrum was corrected for contributions from buffer solutions, containing increasing concentration of GdnHCl (0-4M). The emission spectra were recorded between 250- 205 nm for far-UV CD. The Molar Residue ellipticity (MRE) was calculated using the formula:

$[\theta]$= (θ_{obs} in mdeg)/ (Molar conc. of the protein × path length in mm × Number of amino acids residue present in the protein) [8].

2.9. Equilibrium Unfolding Studies by Extrinsic Fluorophore ANS

Protein bound ANS spectra were recorded on luminescence spectrometer LS 55 (Perkeinelmer Life sciences, USA), using an optical cuvette of pathlength 1 cm. Samples were prepared by incubating DHFR (final conc. 1 µM) and ANS (final concentration 40 µM) with different concentrations of GdnHCl (0-4 M) at 25ºC for 30 min in 10 mM sodium cacodylate, 50 mM NaCl buffer, pH 7.4. Each spectrum was corrected for contributions from buffer solutions, containing increasing concentration of GdnHCl (0-4 M) and constant concentration of ANS (40 µM). The samples were excited at 370 nm and emission spectra were recorded in the wavelength range of 400-600 nm with excitation and emission slit width of 5 nm each.

2.10. Equilibrium Unfolding Studies by Enzymatic Assay

Activity of DHFR samples (final protein concentration 10 µM) containing different concentrations of GdnHCl

(0-4 M) in 10 mM sodium cacodylate, 50 mM NaCl buffer, pH 7.4 was measured according to the method described in section 2.6. The activity of the enzyme was then analyzed against the concentration of GdnCl.

2.11. Spontaneous Refolding Studies on DHFR by Intrinsic Tryptophan Fluorescence Spectroscopy

DHFR (40 μM) was unfolded with 3 M concentration of GdnHCl at 25°C for 1 hr. Denaturation was confirmed by the loss of enzymatic activity as well as change of conformational parameters. The denatured protein was diluted to different concentrations of GdnHCl (2 M, 1 M, 0.5 M, 0.25 M, 0.1 M and 0.01 M) with refolding buffer, 10 mM sodium Cacodylate, 50 mM NaCl, pH 7.4 and allowed to refold at 25°C for 2 hrs. Intrinsic fluorescence was measured for all the samples according to the method mentioned in Subsection 2.7.

2.12. Spontaneous Refolding Studies on DHFR by Enzymatic Assay

DHFR (40 μM) was unfolded with 3 M concentration of GdnHCl at 25°C for 1 hr. Denaturation was confirmed by the loss of enzymatic activity as well as change of conformational parameters. The denatured protein was diluted to different concentrations of GdnHCl (2 M, 1 M, 0.5 M, 0.25 M, 0.1 M and 0.01 M) with refolding buffer, 10 mM sodium Cacodylate, 50 mMNaCl, pH 7.4 and allowed to refold at 25°C for 2 hrs. Activity was checked for all the samples by performing assay for the enzyme according to the method described in Subsection 2.6.

3. RESULTS

3.1. Optimization of Time for Over-Expression of DHFR

BL21 DE3 *E. coli* cells were transformed with pET16b vector containing DHFR plasmid and induced with IPTG to its final concentration of 1mM and kept for incubation at 37°C. Maximum expression for DHFR was obtained after incubating the culture for 12 hrs (**Figure 1**).

3.2. *In Vivo* Folding of DHFR

When the induced cells were sonicated, centrifuged and pellet & supernatant were separated and analyzed on 12% SDS PAGE against un-induced cells and non-transformed cells, the result showed that DHFR was expressed only after induction and most of the protein was in the supernatant only (**Figure 2**). However pellet also contained some of the protein but the amount was very less as compared to the supernatant part.

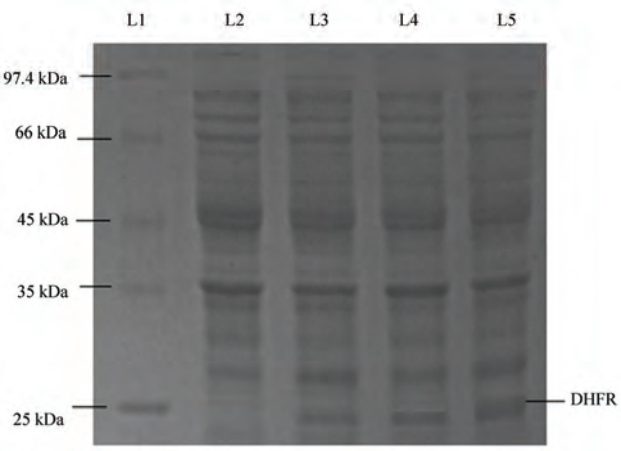

Figure 1. SDS-PAGE shows optimization of time for DHFR expression. Lane L1, marker; lane L2, sample after 3 hr incubation; lane L3 sample after 6 hr incubation; lane L4 sample after 9 hr incubation; lane L5 sample after 12 hr incubation.

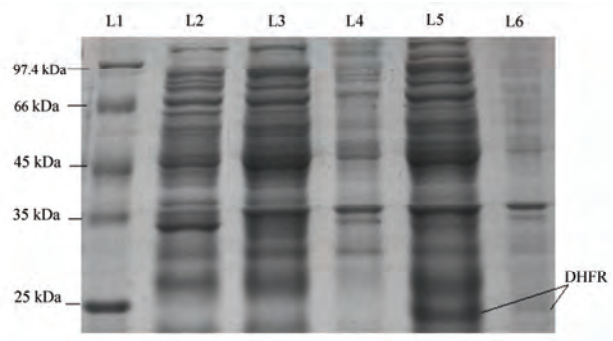

Figure 2. SDS-PAGE shows *in-vivo* folding of DHFR. Lane L1, marker; lane L2, non-transformed cells; lane L3, supernatant of control (un-induced sample); lane L4, pellet of control (un-induced sample); lane L5, supernatant of induced sample; lane L6, pellet of induced sample. The result shows that most of the protein is in folded form.

3.3. Purification of DHFR Using Immobilized Metal Ion Affinity Chromatography (IMAC)

The elution profile of immobilized metal affinity chromatography showed three distinct peaks (data not shown).The third peak appeared during the elution with higher concentration of imidazole, about 225 mM. Fractions corresponding to peak 3 was analysed through 12% SDS PAGE. Dense band at the position of 24 kDa corresponding to DHFR was observed, indicating the presence of DHFR in the solution. No other band in the gel indicated that the solution contained purified DHFR and no other proteins were present in that solution (**Figure 3**). Fractions corresponding to peak 3 were pooled together,

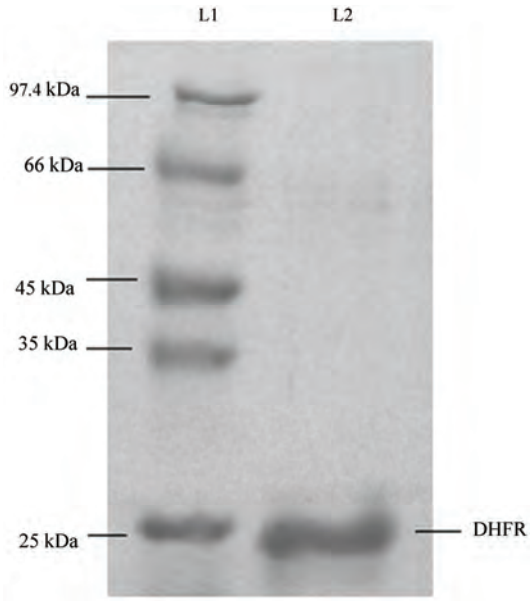

Figure 3. SDS-PAGE shows purified protein in the fraction collected during purification of DHFR corresponding to peak 3 in the chromatogram (not shown). Lane L1, marker; lane L2, fraction corresponding to peak 3 in the chromatogram.

concentrated and stored at 4°C for further in vitro studies.

The concentration of imidazole in the protein solution was reduced to as low as 0.8 mM by buffer exchange method using Amicon centrifugation kit, using 10 kDa molecular weight cut-off (Millipore) membranes. The concentration of the protein in the concentrated solution was determined through Bradford protein estimation method using BSA as a standard. Pure DHFR concentration was found to be 1 mg/ml (40 μM). Substantial activity of the purified protein was observed according to the protocol discussed in Subsection 2.6. This suggested that good amount of protein was present in its active conformation.

3.4. Equilibrium Unfolding and Refolding Studies on DHFR by Intrinsic Tryptophan Fluorescence Spectroscopy

The results obtained for GdnHCl induced conformational transitions of DHFR in 10mM Sodium Cacodylate, 50 mM NaCl, at pH 7.4 and 25°C, studied by intrinsic tryptophan fluorescence are shown in Figure 4 (shown by dots). It is quite evident from the figure 4, that up to 0.75 M of GdnHCl concentration, emission intensity is almost constant. There is not much change in the intrinsic fluorescence. Thereafter, the emission intensity decreased gradually from 1 M to 2.5 M of GdnHCl concentration, from where it became flat. During the refolding studies of denatured DHFR by dilution method, monitored by intrinsic tryptophan fluorescence (shown in **Figure 4** by triangles), it was clear that almost all of the protein had refolded by itself on removal of the denaturant. When the sample was diluted to final GdnHCl concentration of 0.01 M, the relative fluorescence intensity of the protein sample was measured to be 0.96. This showed that protein had refolded almost completely upon removal of GdnHCl.

3.5. Equilibrium Unfolding Studies Monitored By Circular Dichroism

Changes in secondary structure of DHFR, induced by GdnHCl (0-4 M) was monitored by far-UV CD spectroscopy. **Figure 5** shows the unfolding transition curve for the series of GdnHCl concentration, measured by CD ellipticities at 222 nm, expressed by molar residual ellipticities (deg cm^2 $dmol^{-1}$). No appreciable change was observed in ellipticity until a concentration of 1 M GdnHCl. This suggests that there is not much loss of secondary structure up till this concentration of GdnHCl. Beyond 1M concentration of GdnHCl, there was gradual decrease in the ellipticity upto 3 M concentration and then it got flattened. This study showed that the protein got completely unfolded at about 3 M concentration of GdnHCl.

3.6. Equilibrium Unfolding and Refolding Studies Monitored by Enzymatic Assay

Unfolding and refolding of DHFR was studied by per-

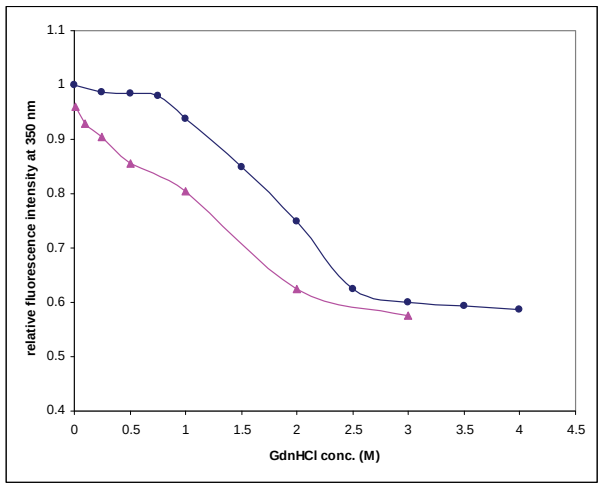

Figure 4. Intrinsic trytophan fluorescence**:** Effect of GdnHCl on equilibrium unfolding of DHFR. Change in tryptophan fluorescence at 350 nm for 1 μM of native protein (pH 7.4, 25°C) denatured by increasing concentration of GdnHCl (0-4 M). It is observed that the Relative fluorescence intensity value (●) becomes nearly constant after 3 M of GdnHCl concentration. (▲) shows spontaneous refolding of DHFR when the completely unfolded protein sample is diluted to different concentrations of GdnHCl (2-0.01 M).

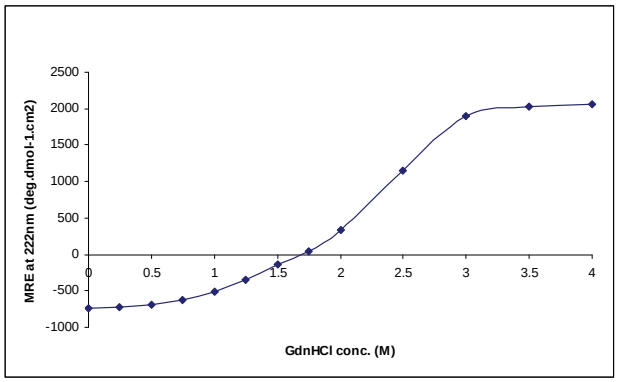

Figure 5. Equilibrium unfolding transition of DHFR monitored by Far-UV CD. Molar residue ellipticity at 222 nm, for 10 µM of native protein, denatured by increasing concentration of GdnHCl, is plotted against GdnHCl conc. (0-4 M). It is observed that MRE value becomes nearly constant after 3 M of GdnHCl concentration.

forming the functional assay for the denatured enzyme and the percentage activity of the denatured enzyme (calculated as compared to activity of native enzyme) was plotted against the GdnHCl concentration as shown in **Figure 6**. During the unfolding process (shown by filled squares in the figure), the activity of the enzyme was lost at 3 M of GdnHCl concentration. On diluting the sample to reduce GdnHCl concentration, the activity of the enzyme was regained. At 0.01 M GdnHCl, almost 95% of the enzymatic activity was regained (filled triangle). This showed that the enzyme had come to its active form after removal of denaturant, confirming its spontaneous refolding.

3.7. Equilibrium Unfolding Studies Monitored by Extrinsic Fluorescence Spectroscopy Using ANS as External Fluorescent Probe

Conformational changes in DHFR, induced by GdnHCl, have also been studied by binding of external fluorescence probe ANS, as shown in **Figure 7**. A steep increase in fluorescence intensity was observed between 0.1-0.3 M of GdnHCl concentration. Maximum fluorescence intensity was observed at 0.3M and it finally decreased to minimum at 3.5 M of GdnHCl, where free ANS molecules are quenched by water and other polar molecules. From our observation, it is quite clear that at 0.3 M of GdnHCl concentration the protein achieved such a conformation, where hydrophobic patches are exposed on the surface much more than native and denatured state. This signifies towards a formation of intermediate at this concentration of GdnHCl.

4. DISCUSSION

In the present study, the pET16b vector containing

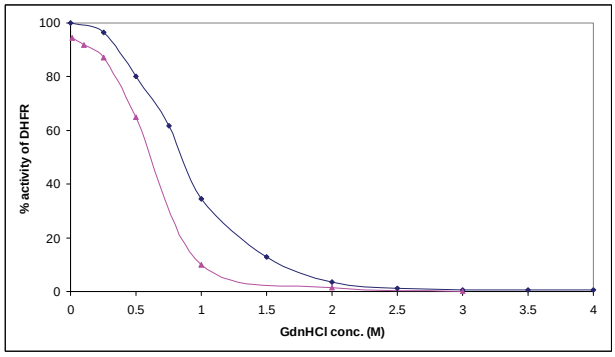

Figure 6. Equilibrium unfolding and refolding of DHFR monitored by change of enzyme activity. (●) shows equilibrium unfolding and refolding of DHFR (protein conc. 1 µM) for increasing GdnHCl (0-4 M). It is clear that the enzyme loses its activity after 2.5 M of GdnHCl. (▲) shows refolding of completely unfolded enzyme by diluting it to different concentrations of GdnHCl (0.01-2 M). It is clear that enzyme regains 95% of its activity on diluting GdnHCl to 0.01 M.

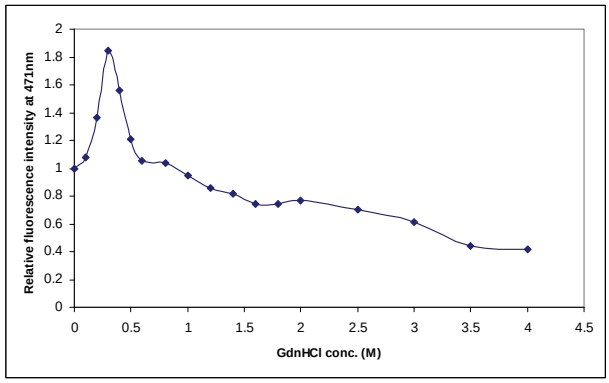

Figure 7. Effect of GdnHCl on extrinsic protein bound ANS fluorescence. Change in ANS fluorescence at 471 nm for 1 µm of native protein and 40µM of ANS, denatured by increasing concentration of GdnHCl (0-4 M). It is observed that the relative fluorescence intensity value becomes maximum at 0.3 M, signifying maximum hydrophobicity at this concentration of GdnHCl.

DHFR gene under control of T7 promoter, was used for over-expression of DHFR in *E. coli* strain that has machinery for T7 RNA polymerase under control of Lac promoter. The chemical induction of the *Lac* promoter was accomplished by the addition of the non-hydrolysable analogue of lactose, IPTG. While larger biomass content before induction is necessary for enhanced expression of the recombinant protein, the cells over-producing recombinant protein should also be sufficiently active at the time of induction. Thus, pre-induction cell concentration (OD_{600}) plays a crucial role for over-expression of recombinant proteins. Expression of DHFR was obtained when induction was carried out in the mid-exponential phase. The protein was purified from

soluble fraction of the over expressed protein, using IMAC Ni^{+2}-chelating chromatography.

The spectroscopy based studies of the unfolding of DHFR with varying concentrations of denaturant gives a close insight into the change in secondary and tertiary structural elements upon denaturation. The equilibrium unfolding studies of *E.coli* DHFR showed that DHFR was completely unfolded above 3M concentration of GdnHCl. The refolding studies monitored by intrinsic tryptophan fluorescence spectroscopy and enzymatic assay of DHFR showed that almost all of the protein folded by itself, without any external assistance.

The tryptophan fluorescence emission intensity gives the clue about the changes in the tertiary structure of the protein. **Figure 4** shows that there was not much change in intrinsic tryptophan fluorescence intensity of the protein up to 0.75 M concentration of GdnHCl. Beyond this concentration there is a sharp fall in intensity until it attains almost constant value and also the λ_{max} shifts to higher wavelengths. This suggests a considerable loss in tertiary structure with increasing concentration of denaturant.

In far-UV CD spectrum also MRE values at 222 nm remain constant up to 0.5 M GdnHCl concentration, and then there is a sharp decrease in the value of ellipticity beyond this concentration of denaturant which continues up to about 3M after which it remains almost constant (**Figure 5**). This trend in the change of ellipticity of DHFR with gradually increasing concentration of denaturant suggests that complete denaturation of the protein took place at about 3 M GdnHCl concentration and the protein lost its secondary structural elements. Similar results were observed when the denaturation was monitored by assaying the enzymatic activity as well as through measuring ANS-bound extrinsic fluorescence intensity of the protein (**Figures 6** & **7**).

However, when the equilibrium unfolding process of DHFR was monitored by extrinsic fluorescence spectroscopy using ANS as the fluorescent probe, distinct intermediate species were observed. It was seen from **Figure 7** that, with increasing denaturant concentration, protein bound ANS fluorescence increased rapidly up to 0.3 M GdnHCl concentration range, which signified the exposure of hydrophobic pockets of DHFR molecule that were otherwise buried inside the core of the native molecule. This phenomenon typically revealed the presence of stable intermediates during the equilibrium unfolding of DHFR. The possibility of salt induced conformational changes of DHFR was nullified by recording ANS-bound DHFR fluorescence emission in presence of gradually higher concentration of NaCl (data not shown). The characteristic features of the equilibrium unfolding intermediate were determined from far-UV CD, intrinsic tryptophan fluorescence spectroscopy, and enzymatic assay. It was observed that the intermediate contains almost identical secondary structural elements, conformation around tryptophan residues were the same and having almost unchanged enzymatic activity. It may resemble a molten-globule like intermediate species in the unfolding pathway of *E. coli* DHFR.

5. CONCLUSIONS

In the present study we have reported that Gdn-HCl denatured *E.coli* DHFR refolded spontaneously after removal of the denaturant through dilution. Hence, the protein does not require any assistance from chaperones for its correct folding. DHFR forms equilibrium unfolding intermediates at around 0.3 M concentration of GdnHCl. The intermediates are having higher exposed surface hydrophobicity, although there were no substantial changes in secondary structural elements and enzymatic activity of the protein. It is worthwhile to study the role of chaperonin GroEL/GroES in accelerating or slowing down the rate of refolding. The reported information also paves the way for designing drugs against the non-native intermediates of DHFR molecules.

6. ACKNOWLEDGEMENTS

The authors acknowledge the financial assistance from Amity Institute of Biotechnology, Amity University, India, and Indian Institute of Technology Delhi, India. One of the authors, TKC, acknowledges the financial assistance from CSIR, Government of India.

REFERENCES

[1] Dobson, C.M. (2001) The structural basis of protein folding and its links with human disease. *Philosophical Transactions of the Royal Society of London, Series B, Biological Sciences*, **356(1406)**, 133-145.

[2] Aiso, K., Nozaki, T., Shimoda, M. and Kokue, E. (1999) Assay of dihydrofolate reductase activity by monitoring tetrahydrofolate using high-performance liquid chromatography with electrochemical detection. *Analytical Biochemistry*, **272(2)**, 143-148.

[3] Sambrook, J. and Russell, D. (2001) Molecular cloning: A laboratory manual. 3rd Edition, Cold Spring Harbor Laboratory Press, New York, **A8**, 1-55.

[4] Laemmli, U.K. (1970) Cleavage of structural proteins during the assembly of the head of bacteriophage T4. *Nature*, **227(5259)**, 680-685.

[5] Chaudhuri, T.K., Farr, G.W., Fenton, W.A., Rospert, S. and Horwich, A.L. (2001) GroEL/GroES-mediated folding of a protein too large to be encapsulated. Cell, **107(2)**, 235-246.

[6] Rao, K.N. and Venkatachalam, S.R. (2000) Inhibition of dihydrofolate reductase and cell growth activity by the

phenanthroindolizidine alkaloids pergularinine and tylophorinidine: The in vitro cytotoxicity of these plant alkaloids and their potential as antimicrobial and anticancer agents. *Toxicology in Vitro*, **14(1)**, 53-59.

[7] Hillcoat, B.L., Nixon, P.F. and Blakley, R.L. (1967) Effect of substrate decomposition on the spectrophotometric assay of dihydrofolate reductase. *Analytical Biochemistry*, **21(2)**, 178-189.

[8] Yang, J.T., Wu, C.-S.C. and Martinez, H.M. (1986) Calculation of protein conformation from circular dichroism. *Methods in Enzymology*, **130**, 208-269.

Vol.1, No.2, 113-118 (2010)
doi:10.4236/jbpc.2010.12014

Journal of Biophysical Chemistry

Biological effects of EV71 infection in neural cells*

Xia Cao[1#], Li-Chun Wang[2#], Long-Ding Liu[2], Yun Liao[2], Cheng-Hong Dong[2], Qi-Han Li[2]**

[1]Department of Immunology and Microbiology, Kunming Medical College, Kunming, China; [#]Both authors contributed equally to this work
[2]Institute of Medical Biology, Chinese Academy of Medical Sciences and Peking Union Medical College, Kunming, China; **Corresponding Author: imbcams.lq@gmail.com

Received 23 May 2010; revised 25 June 2010; accepted 30 June 2010.

ABSTRACT

Enterovirus 71 (EV71) can cause serious nervous system lesions but to date the pathogenesis has been unclear. Our results show that EV71 proliferates in the neural cells and leads to neural cell lesions. The study of the pathology of EV71 infection in neonatal rat brains shows that the invasive ability of EV71 to the nervous system in vivo may depend on many unknown factors.

Keywords: EV71; Neural Cell; Infection; Biological Effects

1. INTRODUCTION

EV71 shares many structural characteristics with Picorna virus and is also a member of the Enterovirus family. Additionally [1], EV71 has been defined as the major pathogen of the hand-foot and mouth disease (HFMD) [2]. The clinical features of HFMD caused by EV71 infection have drawn increased attention [3]. The clinical features of EV71 infection are different from other enteroviruses such as the CoxA16 and CoxB3 that also cause HFMD [4]. A number of severe clinical cases that occurred in an epidemic in the Taiwan and Fuyang regions in China [5,6]suggest that EV71 infection may cause nervous system lesions and lead to a responsive heart and lung failure in some infected patients [7]. The clinical features indicate that the biological significance of EV71 infection in neural cells may affect the epidemiology and clinical consequences of HFMD. Thus, in addition to the study of the pathogenesis of EV71 infection and the epidemiological detection, the study of the biological effects of EV71 infection in neural cells is of great importance. A number of studies have reported the development of a mouse-adapted HEV71 strain and newborn mice infected with mouse-adapted HEV71 [8-10]. These evidence suggests that rodents are not resistant to EV71 infection. Etiological studies of EV71 have so far not provided a good explanation of how EV71 infects neural cells, mainly because there is no established neural cell tissue culture model. In our work, we used a primary rat nerve cell line to examine the basic biological characteristics of the process of EV71 infection in neural cells, as well as the pathological changes caused by EV71 infection in rats. Thus, a basic biological study of EV71 infection in neural cells is provided in this article.

*Foundation item: This work supported by National Natural Science Funds for Young Scholar. (No. 30700205); supported by the Ph.D. Programs Foundation of Ministry of Education of China (No. 200600 23008).

2. MATERIALS AND METHODS

2.1. Viruses and Cells

The EV71-23 isolated strain was provided by the Dept. of Viral Immunology, the Institute of Medical Biology, Chinese Academy of Medical Sciences, which was reproduced and harvested in Vero cells with a titer of 10^7CCID50/ml.

2.2. Rat Cortex Neural Cell Cultures and Phenotype Identification

Four SD neonatal rats were soaked in 75% cold ethanol for 3-5 min before being sacrificed by decapitation under sterile conditions. The rat brains were placed into precooling D-Hanks balanced salt solution. The cerebral cortex was separated by careful removal of the meninges and blood vessels and shredded into a size of about 1 mm^3. The tissues were digested with 0.25% trypsin to a single cell suspension in DF12 complete medium containing 10% FBS, inoculated into culture bottles treated with PLL to a density of 1×10^6, and cultured in relative volume fractions in a 5% CO_2 incubator at 37℃. After 12 h the original culture mediums were replaced with Neurobasal culture media containing 2% B27 for maintenance culture, then one-half of the medium was replaced with Neurobasal/B27 every three days. Culture

bottle coating methods: 0.01 mg/ml of PLL was used for coating for 1 h at 37℃, and bottles were ready for inoculation after washing two times with sterile distilled water. After ten days, the culture medium was discarded, and the neurons were fixed in cold 4% paraformaldehyde for 20 min. Next, 3% H_2O_2 was added to block endogenous peroxidase. The cells were incubated with the primary anti-NSE polyclonal antibody (1:150) at 4℃ overnight, and then the secondary antibody (biotin-labeled goat IgG) was added at room temperature for 30 min. The results were observed under an electron microscope after chromogenic freezing in DAB. In the negative control samples, the primary antibody was replaced with the 0.01 mol/L PBS. All animal care and handling were performed in accordance with the guidelines specified by the Institutes of Health Guide for the Care and Use of Laboratory Animals of Yunnan. During the entire experiment, the animals were monitored online to avoid any unnecessary suffering and to ensure complete anaesthesia.

2.3. Virus Titration

Rat cortex neurons were cultured in 6-well plates for 10 days. The medium was aspirated, and 200 ul of 10^5CCID50/ml virus was added to the cells for 1 h at 37℃ for adsorption. Cell maintenance medium containing 1.0% fetal calf serum was added and cells were incubated in 5% CO_2 at 37℃. For the control group the cell maintenance media was added directly and cultured under the same conditions. The cells were harvested and diluted 10-fold at 24 h and 48 h. The infectious titer was determined to be 5.5 at 10^{-4} diluent degree by the micro-titration test.

2.4. Immunofluorescence Analysis

The coverslip of 10-day cultured cortex neurons (1.0 × 1.0 cm^2) was washed lightly three times in cold 0.01 mol/L PBS (pH 7.4) and fixed with 4% paraformaldehyde for 30 min. The fixed coverslip was washed three times with PBS, 5 min each time, incubated at room temperature for 10 min in 1% H_2O_2, washed two times with PBS for 5 min each wash, and the coverslip was blocked with 1% bovine serum albumin at 37℃ for 30 min. The bovine serum albumin was discarded, and anti-EV71-FY23 polyclonal mouse antibody (1:100) was added and incubated at 4℃ overnight. Next, the coverslip was washed three times with PBS and incubated with FITC labeled goat anti-mouse IgG (1:300) for 2 hours. Finally, the coverslip was washed with PBS three times and photographed under a fluorescence microscope. In the negative control group, the primary antibody was replaced with 0.01 mol/L PBS.

2.5. Electron Microscopy of Infected Cells

The cells were collected after digestion and separation with trypsin 24 hours after virus inoculation and placed into electron microscopy fixing solution mixed with 3% glutaraldehyde plus 1.5% paraformaldehyde, followed by fixation with 1% osmium tetroxide, dehydration with gradient alcohol and embedding with epoxy resin. The neuron ultrastructure was observed through ultrathin sections under electron microscopy.

2.6. Quantitative Detection of the EV71 Viral Load by Real-Time PCR

Cells infected with EV71-23 at different were collected at varying time-points. RNA (TRI REAGENT-BD) was extracted by the Trizol method. Real-time PCR was performed with a one-step PrimescriptTM RT-PCR (TaKaRa) kit. The primer sequences for EV71-23 (gene sequence number is eu812515) are FW primer: 5'-ccacctggagcccctaagccag-3', RV primer: 5'-cattgataagcactcgcagg-3'; and probe primer: 5'-FAM-agcgcaggtttcagtgccattcat-TAMRA3-3'. A volume of 2 ul of total RNA template, 0.5 ul of 10 uM upstream and downstream primers, and 1 ul of Taq man probe solution were used for the reaction for 40 cycles at 42℃ for 5 min, at 95℃ for 10 s, at 95℃ for 5 min. and 60℃ for 40 s.

2.7. Pathological Detection of EV71 Infection in the Nervous System of Rats

0.4 μm thick paraffin sections of the brain of neonatal rats infected by EV71 for five days were used to perform the high-pressure antigen retrieval after deparaffin and dehydration with a gradient ethanol. A volume of 50μl of the primary antibody (VEGF, HO-1 antibody) was added to each slice and incubated in 4℃ overnight. The secondary enzyme-labeled rabbit anti-mouse conjugate antibody was incubated with each slice at room temperature. DAB showed color after 15 minutes. The slices were observed under a microscope for 3-5 minutes, differentiated with 0.1% HCl, washed with tap water to blue, dehydrated and dried with a gradient ethanol, transparencied with xylene, and sealed with neutral gum.

3. RESULTS

3.1. The Primary Passage Culture of Rat Neural Cells and the Phenotype Identification

The neural cortex of neonatal rats were collected, dispersed, screened and cultured in 6-well plates. After 10 days, the cells grew in a monolayer indicating that the networks between neurons are very rich, which is a feature of neurons. Some neural cells assembled into a group (**Figure 1(a)**). To confirm that the cells were neural cells, rather than supporting cells, an immunohisto-

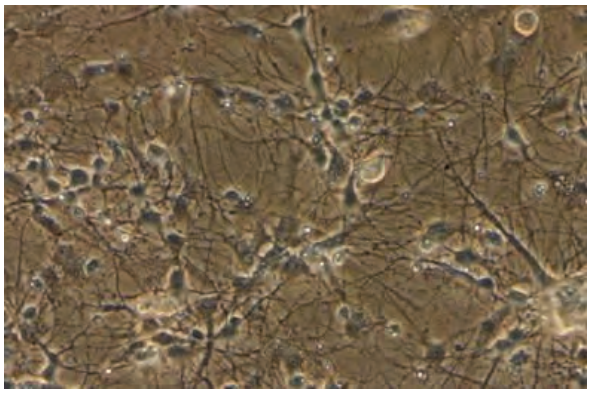

(a)

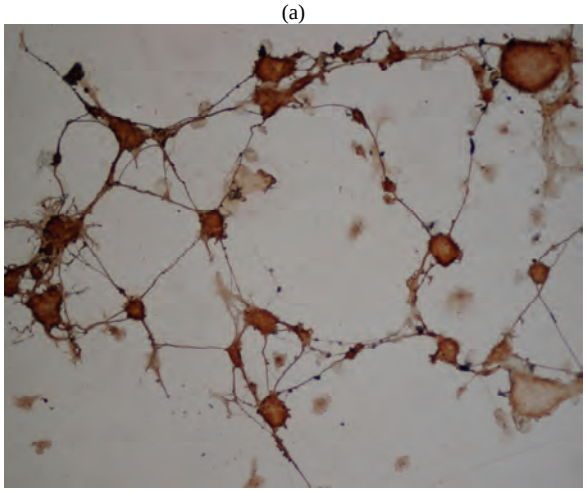

(b)

Figure 1. Primary neuron culture and phenotype identification of neonate rat. (a) Neuron at culture day 10 (×200); (b) NSE labeled neuron (×200).

chemistry staining test was performed using anti-NSE polyclonal antibody. The result showed that the cells had a clear neuronal phenotype (**Figure 1(b)**). Data indicate that neuron-specific enolase (NSE) is a specific marker of neuronal differentiation and maturation. NSE is a cytoplasmic protein and a dimer isozyme involved in the process of glycolysis, which is expressed mainly in neurons and located in neuronal cell bodies, axons and dendrites [11]. The chemical staining method using NSE-specific antibody to immune cells in our test identifies neurons in vitro and allows the analysis of the growth and development of neurons. Our cultured neural cells established a primary neural cell culture while maintaining their phenotypic characteristics.

3.2. Infectious Proliferation of EV71 Cultured in Primary Neural Cells

A monolayer of neural cells were inoculated with virus at an MOI of 0.01. Immunofluorescence analysis of neural cells that had been infected for 8 hours demonstrated EV71 antigen synthesis in the neural cells (**Figure 2(a)**). Examination by light microscopy of neural cells that had been infected for 24 hours showed no pathological features but cells were observed to be round and shrinking (data not shown). However, the electron microscope examination of these cells demonstrated that EV71 infection of neuronal cells led to the typically observed cell lesions, cell degeneration and necrosis, and rupture of cell membrane. In addition, organelles with membrane structures in the cytoplasm were ruptured and dissolved (**Figure 2(b)**). There was no remarkable impact found in red blood cells.

3.3. Analysis of the Growing Dynamics of Infectious Proliferation of EV71 in Infected Neural Cells

Each virus has its own particular growth dynamics in susceptible cells. The proliferation of EV71 in other cells, such as Vero cells and RD cells, shows that its proliferation is similar to other enteroviruses [12]. An analysis of absolute amounts of viral proliferation by an infection at an MOI of 1 in 10^4 neural cells showed that up to 10^6CCID50 of virus were harvested in 24 h (**Figure 3(a)**). The amplification curve from RT-PCR data of EV71 infection in neural cells demonstrates that the proliferation peak occurred 12 h after infection and declined soon after (**Figure 3(b)**).

3.4. Observation of the Infectious Pathology of EV71 in the Neonatal Rat Brain

Although EV71 is able to infect neural cells under tissue culture conditions in vitro, its invasive ability of infection of the nervous system in vivo may depend on more unknown factors. Therefore, we further explored in vivo infection by inoculating EV71 into the nerve tissue of neonatal rats by intracerebral injection to analyze infection using clinical and histopathological indicators. Observation of neonatal rats inoculated with 10^5CCID50 EV71 by intracerebral injection for 10 days indicated that EV71 did not cause the experimental neonatal rat group to develop clinical symptoms (data not shown). However, a histopathological observation of brain nerve tissue of a neonatal rat, which was killed on the fifth day of infection, indicated that the intracerebral injection of EV71 did cause an apparent inflammatory reaction, emergence of nerve glial cell aggregation, and a small amount of nerve cell damage (**Figures 4(a)**, **(b)**, and **(c)**).

4. DISCUSSION

It is difficult to clinically distinguish HFMD caused by EV71 infection from CoxA16 infection but EV71 can cause nervous system lesions with higher mortality rates

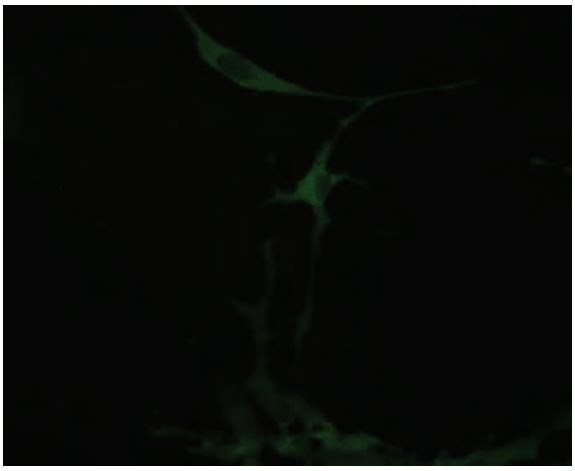

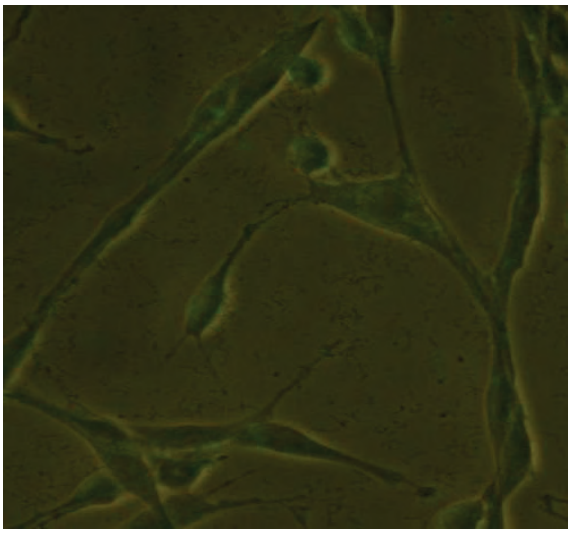

Negtive control

(a)

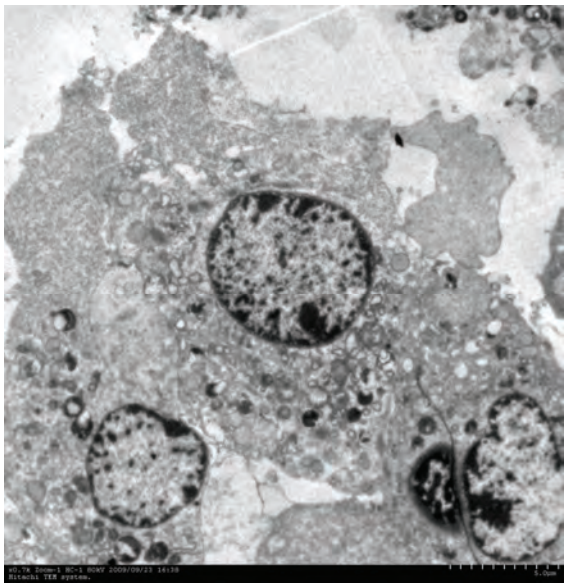

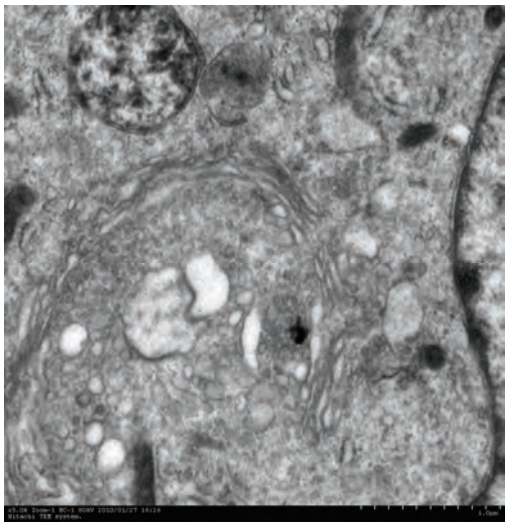

Negtive control

(b)

Figure 2. Cell biology change of EV71 infected neuron. (a) EV71 antigen synthesis in the neural cells; (b) Electron microscope examination of EV71 infected neuron.

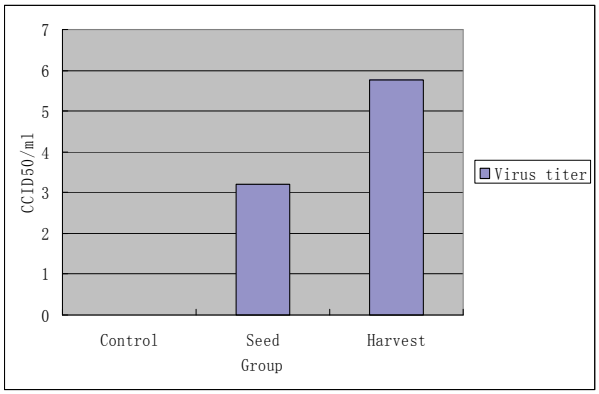

(a)

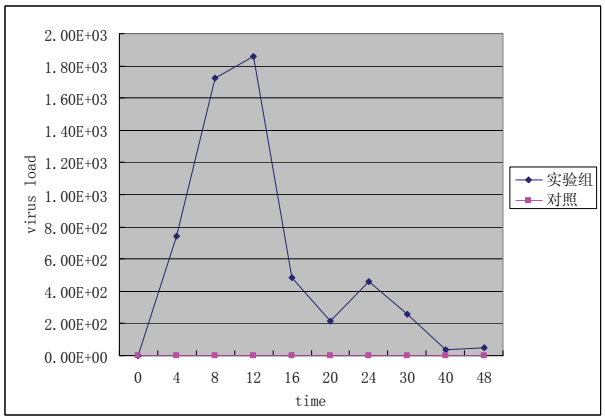

(b)

Figure 3. Growth kinetics analysis of EV71 infected neuron. (a) Proliferation of EV71 in neuron; (b) The amplification curve of EV71 infection in neuron.

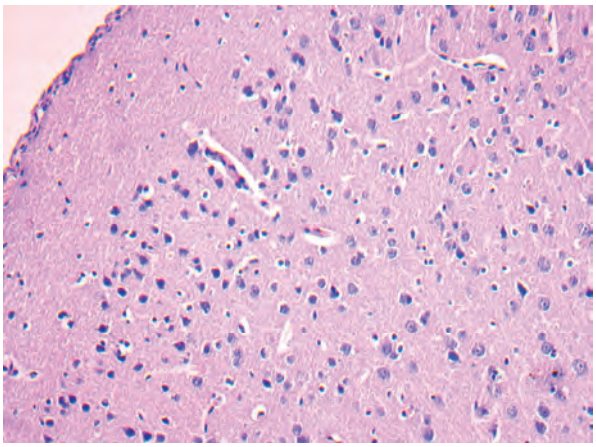

(a)

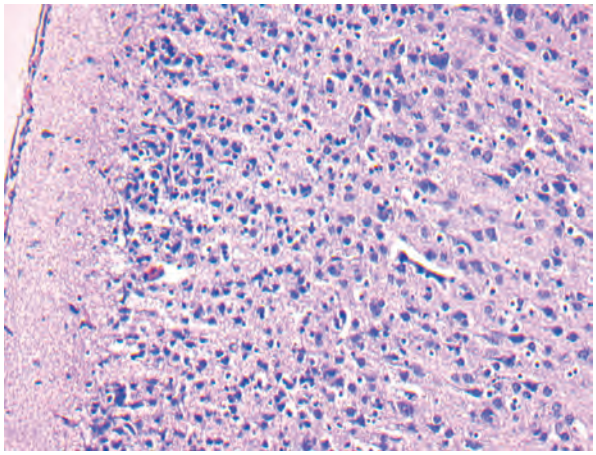

(b)

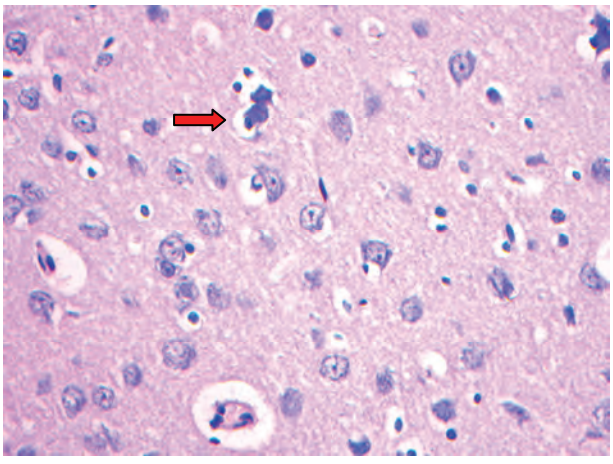

(c)

Figure 4. EV71 virus transcranial inoculates and infects neonate rats' nervous tissue. (a) Normal neonate rat (×200); (b) Infected EV71 for 5 days (×200), it is clear that glial cell diffusely hyperplasy; (c) Infected EV71 for 5 days (×400) arrowhead showed neuronophagia.

and is an extreme hazard in children with severe infections. However, extensive research on EV71 infection of the nervous system is lacking, and particularly there have been no studies in primary neural cells, which could have a great impact on understanding the epidemiology and clinical consequences of HFMD. Thus, analysis of the biological effects of EV71 infection in neural cells will help to understand the pathogenesis of EV71 infection and its clinical impact. As known before, HEV71 has a limited host range, with humans and some monkeys. Therefore, the high cost of monkeys and their maintenance precludes their widespread use for studies of viral pathogenesis. Thus, a small animal model would provide a more cost-effective and practical tool for studies of HEV71 pathogenesis and for vaccine development. A number of studies have suggested that rodents are not resistant to EV71 infection. Since we think mouse-adapted EV71 strains are imperfect, so we want to search other cell lines which facility infected by EV71. On the other hand, it is more convenient to observe the pathological change in rat brain than that of mouse because the former is bigger that the latter. In our study, immunofluorescence analysis of neural cells infected for 8 hours showed EV71 antigen synthesis, which was concentrated in the cytoplasm and neural synapses. Although no lesions were observed under the optical microscope in neural cells infected for 24 hours, subsequent electron microscopy showed that organelles were dissolved and broken. The result showed that EV71 infection affected the cytoplasm and synapses, as observed by Immunofluorescence, as well as the nucleus. Electron microscopy also confirmed the role of EV71 in causing neural cells lesions. An analysis of the growth dynamics of EV71 during infection of neural cells showed specific growth dynamics associated with enterovirus proliferation, which demonstrates that neural cells are as susceptible to infection as other cells. These results show that EV71 could indeed infect and proliferate in neural cells in vivo. To further understand the role of EV71 infection in rats, we examined the pathology of infection in neonatal rat brains. A small amount of nerve cell damage, obvious inflammation and glial cell proliferation were found in the nerve tissue of neonatal rats that were infected for 5 days. This indicated that infection of neonatal rats resulted in a certain degree of central nervous system lesions. There were no obvious clinical symptoms observed among neonatal rats after 10 days infection. We speculate that this is because the nervous system lesions were mild and were able to recover gradually. The result further indicates that there are a variety of complex factors involved in EV71 infection in neural cells in vivo. Therefore, complex pathways should be considered in further studies of the mechanism of EV71 infection of the nervous system.

REFERENCES

[1] Brown, B.A. and Pallansch, M.A. (1995) Complete nucleotide sequence of enterovirus 71 is distinct from poliovirus. *Virus Research*, **39(2-3)**, 195-205.

[2] Chan, K.P., Goh, K.T., Chong, C.Y., *et al*. (2003) Epidemic hand, foot, and mouth disease caused by human enterovirus 71, Singapore. *Emerging Infectious Diseases*, **9(1)**, 78-85.

[3] McMinn, P.C. (2002) An overview of the evolution of enterovirus 71 and its clinical and public health significance. *FEMS Microbiology Reviews*, **26(1)**, 91-107.

[4] Ho, M. (2000) Enterovirus 71: The virus, its infections, and outbreaks. *Journal of Microbiology, Immunology and Infection*, **33(4)**, 205-216.

[5] Lin, T.Y., Twu, S.J., Ho, M.S., *et al*. (2003) Enterovirus 71 outbreaks, Taiwan: Occurrence and recognition. *Emerging Infectious Diseases*, **9(3)**, 291-293.

[6] Wan, J.F., Zhu, L.Y., Liu, H., *et al*. (2008) Analysis of EV71 epidemic situation in Fuyang. *Anhui Medicine*, in Chinese, **29(4)**, 344-345.

[7] Huang, C.C., Liu, C.C., Chang, Y.C., *et al.* (1999) Neurologic complications in children with enterovirus 71 infection. *The New England Journal of Medicine*, **341(13)**, 936-942.

[8] Chen, Y.C., Yu, C.K., Wang, Y.F., *et al*. (2004) A murine oral enterovirus 71 infection model with central nervous system involvement. *Journal of General Virology*, **85(1)**, 69-77.

[9] Chung, Y.C., Ho, M.S., Wu, J.C., *et al*. (2008) Immunization with virus-like particles of enterovirus 71 elicits potent immune responses and protects mice against lethal challenge. *Vaccine*, **26(15)**, 1855-1862.

[10] Tung, W.S., Bakar, S.A., Sekawi, Z., *et al*. (2007) DNA vaccine constructs against enterovirus 71 elicit immune response in mice. *Genetic Vaccines and Therapy*, **5(1)**, 6.

[11] Schmechel, D.E., Brightman, M.W. and Marangos, P.J. (1980) Neurons switch from non-neuronal enolase to neuron-specific enolase during differentiation. *Brain Research*, **190(1)**, 178-181.

[12] Yang, Z.F., Qing, S., Mo, Z.Y., *et al*. (2009) Detection of five different cells' sensitivities to enterovirus 71 using plaque forming assay *World Journal of Gastroenterology*, in Chinese, **17(6)**, 573-577.

Vol.1, No.2, 119-133 (2010)
doi:10.4236/jbpc.2010.12015

Journal of Biophysical Chemistry

Overtone spectra of porphyrins and its substituted forms: an algebraic approach

Srinivasa Rao Karumuri[1]*, Ambati Siva Rama Prasad[2], Nirmal Kumar Sarkar[3], Joydeep Choudhury[4], Ramendu Bhattacharjee[4]

[1]Faculty of Sciences & Humanities, Sri Viveka Institute of Technology (SVIT), Vijayawada, India; *Corresponding Author: drsrkarumuri@rediffmail.com
[2]Faculty, Department of Mathematics, P.B. Siddhartha College of Arts & Sciences, Vijayawada, India
[3]Faculty, Department of Physics, Karimganj College, Karimganj, India
[4]Faculty, Department of Physics, Assam (A Central) University, Silchar, India

Received 8 June 2010; revised 13 July 2010; accepted 18 July 2010.

ABSTRACT

We introduce an algebraic model to vibrations of polyatomic Bio-molecules and present, as an example, the vibrational analysis of C_m-H, C_m-C, C_m-D, C_b-C_b, pyrrol breathing and C_b-C, stretching modes of Metalloporphyrins and its substituted forms. The excited energy levels of C_b-C, pyrrol breathing stretching modes of Ni(OEP) and Ni(OEP)-d_4 are calculated by using U(2) algebraic mode Hamiltonian. The higher excited energy levels of C_m-H, C_m-C, C_m-D and C_b-C_b vibrational modes of Porphyrin and its substituted forms are predicted upto second overtone. It shows that the energy levels are clustering at the higher overtones. The results obtained by this method are accuracy with experimental data.

Keywords: Algebraic Model; Vibrational Spectra; Energy Levels; Metalloporphyrins

1. INTRODUCTION

Recently measurement of highly-excited overtone-combination spectra of molecules have renewed in a theoretical description and understanding of the observed spectral properties. Two approaches have been mostly used so far in an analysis of experimental data: 1) the familiar Dunham like expansion of energy levels in terms of rotations-vibrations quantum numbers and 2) the solution of Schrodinger equation with potentials obtained either by appropriately modifying ab-initio calculations or by more phenomenological methods. In this article, we begin a systematic analysis of overtone-combination spectra of molecules in terms of novel approach: 3) Vibron model [1-4]. This model is a formulation of the molecular spectral problem in terms of elements of Lie algebra and it contains the same physical information of the Dunham and potential approach. However, by making use of the powerful methods of group theory, one is able to obtain the desired results in a much faster and straightforward way.

In recent years, these polyatomic bio-molecules (*i.e* Metalloporphyrins) have numerous importances in the field of Chemical Physics. In case of polyatomic bio-molecules the parameters play major role in the Vibron model. Of course, we have explicitly described with few parameters, the vibrational bands of the triatomic linear molecules HCN, OCS, HCP [5-7] and tetratomic molecules HCCF, HCCD by using an algebraic approach [8]. We have also reported the vibrational bands of tetrahedral molecules CCl_4, $SnBr_4$ and Propadiene [9-11] and polyatomic bio-molecules like Nickel Octaethyl porphyrin, Nickel porphyrin molecules using U (2) Vibron model respectively [12-18]. The advantage of the algebraic approach, as compared to that of Dunham or phonological potential models, is that typically it requires few parameters to obtain the same level of accuracy. It also provides a simultaneous description of bending and stretching modes [19-25].

In Section 2, review the theory of algebraic model to polyatomic molecules is described. In Section 3, the calculation procedure of Vibron number and the fitting algebraic parameters corresponding to various Porphyrins and its substitute form molecule results are discussed. Finally, the conclusions are presented in Section 4.

2. THEORY: AN ALGEBRAIC APPROACH

A complete description of the theoretical foundations

needed to formulate the algebraic model for a vibrating molecule. We apply the one-dimensional algebraic model, consisting of a formal replacement of the interatomic, bond coordinates with unitary algebras. To say it in different words, the second-quantization picture suited to describe anharmonic vibrational modes, is specialized through an extended use of Lie group theory and dynamical symmetries. By means of this formalism, one can attain algebraic expressions for eigenvalues and eigenvectors of even complex Hamiltonian operators, including intermode coupling terms as well expectation values of any operator of interest (such as electric dipole and quadrupole interactions). Algebraic model are not ab-initio methods, as the Hamiltonian operator depends on a certain number of a priori undetermined parameters. As a consequence, algebraic techniques can be more convincingly compared with semi-empirical approaches making use of expansions over power and products of vibrational quantum numbers, such as a Dunham-like series. However, two noticeable advantages of algebraic expansions over conventional ones are that 1) algebraic modes lead to a (local) Hamiltonian formulation of the physical problem at issue(thus permitting a direct calculation of eigenvectors in this same local basis) and 2) algebraic expansions are intrinsically anharmonic at their zero-order approximation. This fact allows one to reduce drastically the number of arbitrary parameters in comparison to harmonic series, especially when facing medium-or large- size molecules. However, it should also be noticed that, as a possible drawback of purely local Hamiltonian formulations (either algebraic or not) compared with traditional perturbative approaches, the actual eigenvectors of the physical system. Yet, for very local situations, the aforementioned disadvantage is not a serious one. A further point of import here is found in the ease of accounting for proper symmetry adaptation of vibrational wave functions. This can be a great help in the systematic study of highly excited overtones of not-so-small molecules, such as the present one. Last but not least, the local mode picture of a molecule is enhanced from the very beginning within the algebraic framework. This is an aspect perfectly lined up with the current tendencies of privileging local over normal mode pictures in the description of most topical situations.

2.1. Hamiltonian Operators

We address here the explicit problem of the construction of the vibrational Hamiltonian operator for the Metalloporphyrin molecules. According to the general algebraic description for one-dimensional degrees of freedom, a dynamically-symmetric Hamiltonian operator for n-interacting (not necessarily equivalent) oscillators can be written as

$$H = E_0 + \sum_{i=1}^{n} A_i C_i + \sum_{i\langle j}^{n} A_{ij} C_{ij} + \sum_{i\langle j}^{n} \lambda_{ij} M_{ij} \qquad (1)$$

In this expresssion, one finds three different classes of effective contributions. The first one, $\sum_{i=1}^{n} A_i C_i$ is devoted to the description of n independent, anharmonic sequences of vibrational levels (associted wih *n* independent, local oscillator) in terms of the operators C_i. The second one, $\sum_{i\langle j}^{n} A_{ij} C_{ij}$ leads to cross-anharmonicities between pairs of distinct local oscillators in terms of the operators C_{ij}. The third one, $\sum_{i\langle j}^{n} \lambda_{ij} M_{ij}$, describes anharmonic, non-diagonal interactions involving pairs of local oscillators in terms of the operators M_{ij}. The C_i, C_{ij} operators are invariant (Casimir) operators of certain Lie algebras, whilst the M_{ij} are invariant (Majorana) operators associated with coupling schemes involving algebras naturally arising from a systematic study of the algebraic formulation of the one-dimensional model for n interacting oscillators. We work in the local (uncoupled oscillaators) vibrational basis written as

$$|\nu\rangle \equiv |\nu_1\nu_2\nu_3.....\nu_n\rangle$$

In which the aforementioned operators have the following matrix elements

$$\langle \nu | C_i | \nu \rangle = -4\nu_i(N_i - \nu_i)$$

$$\langle \nu | C_{ij} | \nu \rangle = -4(\nu_i + \nu_i)(N_i + N_j - \nu_i - \nu_j)$$

$$\langle \nu' | M_{ij} | \nu \rangle = (\nu_i N_i + \nu_j N_j - 2\nu_i\nu_j)\delta_{\nu_i'\nu_i}\delta_{\nu_j'\nu_j}$$

$$\langle \nu' | M_{ij} | \nu \rangle = -[(\nu_i + 1)(N_i - \nu_i)\nu_j(N_j - \nu_j + 1)]^{1/2}\delta_{\nu_i'-1\nu_i}\delta_{\nu_j'+1\nu_j}$$

$$\langle \nu' | M_{ij} | \nu \rangle = -[(\nu_j + 1)(N_j - \nu_j)\nu_i(N_i - \nu_i + 1)]^{1/2}\delta_{\nu_i'+1\nu_i}\delta_{\nu_j'-1\nu_j}$$

We note, in particular, that the expressions above depend on the numbers N_i (Vibron numbers). Such numbers have to be seen as predetermined parameters of well-defined physical meaning, as they relate to the intrinsic anharmonicity of a single, uncoupled oscillator through the simple relation. We report in **Table 4** & **Table 5** the values of the Vibron numbers used in the present study.

The general Hamiltonian operator (1) can be adapted to describe the internal, vibrational degrees of freedom of any polyatomic molecule in two distinct steps. First, we associate three mutually perpendicular one-dimensional anharmonic oscillators to each atom. This procedure eventually leads to a redundant picture of the whole molecule, as it will include spurious (*i.e* translational/rotational) degrees of freedom. However, it is possible to remove easily such spurious modes through

different techniques. One is thus left with a Hamiltonian operator dealing only with true vibrations. Such modes are given in terms of coupled oscillators in the local basis (3). The coupling is induced by the Majorana operators. A sensible use of these operators is such that the correct symmetries of vibrational wave functions are properly taken into account. As a second step, the algebraic parameters A_i, A_{ij}, λ_{ij} of **Eq.1** need to be calibrated to reproduce the observed spectrum. Let us clarify the actual meaning of these two steps by considering explicitly the C_m-H/C_m-D/C_m-N stretches manifold of the Nickel Metalloporphyrin molecule.

We limit ourselves to in-plane C_m-H/C_m-D/C_m-N stretching motions *i.e.*, without including possible coupling terms with ring deformation. So, we can write for these remaining four degrees of freedom the Hamiltonian operator,

$$H_{CH} = \sum_{i=1}^{4} A_i C_i + \sum_{i<j}^{4} A^{1}_{ij} C_{ij} + \sum_{i<j}^{4} \lambda_{ij} M_{ij}$$

The algebraic theory of polyatomic molecules consists in the separate quantization of rotations and vibrations in terms of vector coordinates r_1, r_2, r_3,……. quantized through the algebra

$$G \equiv U_1(2) \otimes U_2(2) \otimes U_3(2) \otimes .....$$

For the stretching vibrations of polyatomic molecules correspond to the quantization of anharmonic Morse oscillators, with classical Hamiltonian

$$H(p_s,\ s) = p_s^2/2\mu + D[1 - \exp(-\beta s)]^2 \qquad (2)$$

For each oscillator i, states are characterized by representations of

$$\left| \begin{array}{ccc} U_i(2) & \supset & O_i(2) \\ \downarrow & & \downarrow \\ N_i & & m_i \end{array} \right\rangle \qquad (3)$$

With $m_i = N_i, N_i - 2,\ldots..,1$ or 0 (N_i - odd or even). The Morse Hamiltonian (2) can be written, in the algebraic approach, simply as

$$H_i = \varepsilon_{0i} + A_i\, C_i, \qquad (4)$$

where C_i is the invariant operator of $O_i(2)$, with eigen values

$$\varepsilon_i = \varepsilon_{0i} + A_i\,(m_i^2 - N_i^2).$$

Introducing the vibrational quantum number $v_i = (N_i - m_i)/2$, [26] one has

$$\varepsilon_i = \varepsilon_{0i} - 4A_i\,(N_i\, v_i - v_i^2\,). \qquad (5)$$

For non-interacting oscillators the total Hamiltonian is

$$H = \sum_i H_i\,,$$

With eigenvalues

$$E = \sum_i \varepsilon_i = E_0 - \sum_i 4A_i\,(N_i\, v_i - v_i^2). \qquad (6)$$

2.2. Hamiltonian for Stretching Vibrations

The interaction potential can be written as

$$V(s_i, s_j) = k_{ij}'[1 - \exp(-\alpha_i\, s_i)][1 - \exp(-\alpha_j\, s_j)], \qquad (7)$$

which reduces to the usual harmonic force field when the displacements are small

$$V(s_i, s_j) \approx k_{ij}\, s_i\, s_j\,.$$

Interaction of the type **Eq.7** can be taken into account in the algebraic approach by introducing two terms [26]. One of these terms is the Casimir operator, C_{ij}, of the combined $O_i(2) \otimes O_j(2)$ algebra. The matrix elements of this operator in the basis **Eq.3** are given by

$$\langle N_i, v_i; N_j, v_j \,|\, C_{ij} \,|\, N_i, v_i; N_j, v_j \rangle = 4[(v_i + v_j)^2 - (v_i + v_j)(N_i + N_j)] \qquad (8)$$

The operator C_{ij} is diagonal and the vibrational quantum numbers v_i have been used instead of m_i. In practical calculations, it is sometime convenient to substract from C_{ij} a contribution that can be absorbed in the Casimir operators of the individual modes i and j, thus considering an operator C_{ij}' whose matrix elements are

$$\langle N_i, v_i; N_j, v_j \,|\, C_{ij}' \,|\, N_i, v_i; N_j, v_j \rangle = 4[(v_i + v_j)^2 - (v_i + v_j)(N_i + N_j)] + [(N_i + N_j)/N_i]4(N_i v_i - v_i^2) + [(N_i + N_j)/N_j]4(N_j v_j - v_j^2). \qquad (9)$$

The second term is the Majorana operator, M_{ij}. This operator has both diagonal and off-diagonal matrix elements

$$\langle N_i, v_i; N_j, v_j \,|\, M_{ij} \,|\, N_i, v_i; N_j, v_j \rangle = (N_i v_j + N_j v_i - 2 v_i v_j)$$

$$\langle N_i, v_i + 1\,;\, N_j, v_j - 1 \,|\, M_{ij} \,|\, N_i, v_i; N_j, v_j \rangle = -[v_j(v_i + 1)(N_i - v_i)(N_j - v_j + 1)]^{1/2}$$

$$\langle N_i, v_i - 1; N_j, v_j + 1 \,|\, M_{ij} \,|\, N_i, v_i; N_j, v_j \rangle = -[v_i(v_j + 1)(N_j - v_j)(N_i - v_i + 1)]^{1/2} \qquad (10)$$

The Majorana operators M_{ij} annihilâtes one quantum of vibration in bond i and create one in bond j, or vice versa.

The total Hamiltonian for n stretching vibrations is

$$H = E_0 + \sum_{i=1}^{n} A_i C_i + \sum_{i<j}^{n} A_{ij}\, C_{ij} + \sum_{i<j}^{n} \lambda_{ij}\, M_{ij} \qquad (11)$$

If λ_{ij} =0 the vibrations have local behavior. As the λ_{ij} s increase, one goes more and more into normal vibrations.

2.3. Symmetry- Adapted Operators

In polyatomic molecules, the geometric point group symmetry of the molecule plays an important role. States must transform according to representations of the point symmetry group. In the absence of the Majorana operators M_{ij}, states are degenerate. The introduction of the Majorana operators has two effects: 1) it splits the degeneracies of figure and 2) in addition it generates states with the appropriate transformation properties under the point group. In order to achieve this result the λ_{ij} must be chosen in an appropriate way that reflects the geometric symmetry of the molecule. The total Majorana operator

$$S = \sum_{i<j}^{n} M_{ij} \qquad (12)$$

is divided into subsets reflecting the symmetry of the molecule

$$S = S' + S'' + \text{----------}. \qquad (13)$$

The operators S', S'', ------ are the symmetry-adapted operators. The construction of the symmetry-adapted operators of any molecule become clear in the following sections where the cases of Porphyrins (D_{4h}) discussed.

2.4. Hamiltonian for Bending Vibrations

We emphasize once more that the quantization scheme of bending vibrations in U(2) is rather different from U(4) and implies a complete separation between rotations and vibrations. If this separation applies, one can quantize each bending oscillator i by means of an algebra $U_i(2)$ as in **Eq.2**. The Poschl-Teller Hamiltonian

$$H(p_s, s) = p_s^2/2\mu - D/\cosh^2(\alpha s) \qquad (14)$$

Where we have absorbed the $\lambda(\lambda - 1)$ part into D, can be written, in the algebraic approach, as

$$H_i = \varepsilon_{0i} + A_i C_i, \qquad (15)$$

This Hamiltonian is identical to that of stretching vibration (**Eq.3**). The only difference is that the coefficients A_i in front of C_i are related to the parameters of the potential, D and α, in a way that is different for Morse and Poschl-Teller potentials. The energy eigenvalues of uncoupled Poschl-Teller oscillators are, however, still given by

$$E = \sum_i \varepsilon_i = E_0 - \sum_i 4A_i (N_i v_i - v_i^2). \qquad (16)$$

One can then proceed to couple the oscillators as done previously and repeat the same treatment of **Eqs.2**, **3**, and **4**.

2.5. The Metalloporphyrin Molecule

The construction of the symmetry-adapted operators and of the Hamiltonian operator of polyatomic molecule illustrated using the example of Metalloporphyrin. In order to do the construction, draw a figure corresponding to the geometric structure of the molecule (**Figure 1**). Number of degree of freedom we wish to describe.

By inspection of the figure, one can see that two types of interactions in Metalloporphyrin:

1) First-neighbor couplings (Adjacent interactions)

2) Second–neighbor couplings (Opposite interactions)

With D_{4h} symmetry here, the operators (on the basis of the considerations mentioned above) are

$$S = \sum_{i<j}^{n} M_{ij}\ ,\ S' = \sum_{i<j}^{n} c'_{ij} M_{ij},\ S'' = \sum_{i<j}^{n} c''_{ij} M_{ij}.$$

$c'_{12} = c'_{23} = c'_{34} = c'_{45} = \text{- - - - -} = 1,\ c'_{13} = c'_{24} = c'_{35} = c'_{46}$

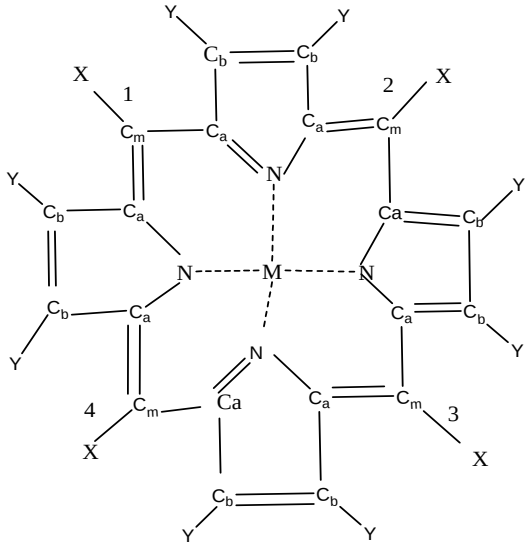

Figure 1. The structure of Metalloporphyrin.

Ni (OEP)	→ X = H,	Y = Ethyl,
Ni (OEP)-d_4	→ X = D,	Y = Ethyl.
Ni (TPP)	→ X = Phenyl,	Y = H,
Cu (TMP)	→ X = Mesityl,	Y = H.
Ni Por	→ X = H,	Y = H.

= - - - - - =0,

$c''_{12} = c''_{23} = c''_{34} = c''_{45} = \text{- - - - -} = 0,\ c''_{13} = c''_{24} = c''_{35} = c''_{46} = \text{- - - - -} = 1, \qquad (17)$

Diagonalization of S' produces states that carry representations transform according to the representations A_{1g}, B_{1g}, A_{2g}, B_{2g}, and E_{1u} of D_{4h}. The S' operator is thus the "symmetry adapter" operator. This result, which, at first sight, appears to be surprising, can be easily verified by computing the characters of the representations carried by the eigenstates of S' in the usual way. Here, in this case the value of n is either 4 ($j = 4$, $i = 3$) or 8 ($j = 8$, $i = 7$).

3. RESULTS AND DISCUSSIONS

We have used U (2) algebraic model to study vibrational spectra of the Porphyrin and its substituted form molecules. The fitting algebraic parameters are A, A', λ, λ' and N (Vibron number). The values of Vibron number (N) can be determined by the relation

$$N_i = \frac{\omega_e}{\omega_e x_e} - 1,\ (i = 1, 2, \ldots\ldots) \qquad (18)$$

where ω_e and $\omega_e x_e$ are the spectroscopic constants of diatomic molecules [27]. This numerical value must be seen as initial guess; depending on the specific molecular structure, one can expect changes in such an estimate, which, however, should not be larger than ± 20% of the original value (**Eq.18**). The Vibron number N between

the diatomic molecule C-C, C-H and C-D are 140, 44 and 59 respectively. From the figure 1, it is noticed that some of the bonds are equivalent. It may be noted that during the calculation of the vibrational frequencies of Porphyrins and substituted forms, the value of N is kept fixed and not used as free parameter.

The second step is to obtain a starting guess for the parameter *A*. As such, the expression for the single-oscillator fundamental mode as

$$E\ (v\ =\ 1)\ =\ -4\ A\ (N\ -\ 1). \qquad (19)$$

In the present case we have three different energies, corresponding to symmetric and antisymmetric combinations of the different local modes. A possible strategy is to use the center of gravity of these modes, so the guess for

$$\bar{A} = \frac{\bar{E}}{4(1-N)} \qquad (20)$$

The third step is to obtain an initial guess for λ. Its role is to split the initially degenerate local modes, placed here at the common value *E* used in **Eq.19**. Such an estimate is obtained by considering the simple matrix structure, we can find

$$\lambda = \frac{\left|E_{Eu} - E_{A1g}\right|}{2N} \qquad (21)$$

$$\&\quad \lambda^{!} = \frac{\left|E_{B2g} - E_{A1g}\right|}{4N} \qquad (22)$$

Finally a numerical fitting procedure is to be carried to adjust (in a least- square sense, for example) the parameters *A* and λ starting from values **Eq.20** and **Eq.21**, and A' (whose initial guess can be zero).

Using the **Eqs.20**, **21** and **22**, *A*, λ and λ' are calculated [4,5-7,27] using the available data points. We have taken $\lambda'' = 0$ (In this case, the next nearest neighbor couplings are omitted). As one can see from **Table 1** & **Table 2**, the agreement with experiment is good and thus we think that the parameter set of **Table 4** & **Table 5** can be used reliably to compute energies of highly excited overtones. We note that in **Table 2** & **Table 3**, there are many predicted overtones that have not been studied experimentally. We have explicit calculations up to the second overtone (energy up to $\approx 10000\ cm^{-1}$).

We have used the algebraic Hamiltonian to study the highly excited vibrational levels of the molecule Ni (TPP), Cu (OEP), Mg (OEP), Cu (TPP), Cu (TMP), Ni Porphyrin, Ni (OEP) and its substitution form Ni (OEP)-d_4. Eight bands are studied, which can be labeled the C_m-H, C_b-C_b and only for Ni (OEP)-d_4 the bands labeled are C_m-D, C_b-C_b respectively. The highly excited vibrational levels, calculated by using the algebraic Hamiltonian **Eq.11**, are shown in **Figures 2, 3, 4**, and **5** (The detail calculated vibrational energy levels are listed in **Tables 3**). **Figures 2** and **3** gives the levels corresponding to the C_m-H, C_b-C_b of Ni (TPP). **Figures 4** and **5** gives the levels corresponding to the C_m-H, C_b-C_b of Cu (TPP). **Figures 6** and **7** gives the levels corresponding to the C_m-H, C_b-C_b of Cu (TMP). **Figures 8** and **9** gives the levels corresponding to the C_m-D, C_b-C_b of Ni (OEP)-d_4. When the quantum number ν increases in a fixed band, the numbers of energy levels increase rapidly. Usually, the degeneracy or quanti-degeneracy of energy levels is called clustering. It may be seen from **Figures 2**, **3**, **4**, **5**, **6**, **7**, **8** and **9** that the vibrational energy levels of Porphyrin and its substituted form make up clusters.

4. CONCLUSIONS

In this paper, we have presented a systematic analysis of vibrational spectra of Porphyrin and its substituted forms in the algebraic framework making use of the one-dimensional Vibron model *i.e.* U (2) Vibron model.

Using the U (2) algebraic model Hamiltonian, the stretching frequencies of C_b-C and Pyrrol breathing up to Second overtone (ν = 2), the combinational bands of Nickel Octaethyl Porphyrin [Ni(OEP)] and its substituted form Ni(OEP)-d_4 molecules are given in **Table 2**. However, due to lack of sufficient data base, we could not compare the calculated vibrational frequencies with that of observed data of Nickel Metalloporphyrin and its substituted forms at higher overtones. This study is useful to the experimentalist to analyze the predicted vibrational frequencies with the observed data. The model pre sented here describes the splitting of local stretching/bending modes due to residual interbond interactions. The splitting pattern determines the nature of interaction (Parameterλ λ'). Once we get the parameter, we predict the splitting pattern of overtones. It is worth to point out that most applications of previous algebraic models available in literature [28-33] are restricted to vibrations of Bio-molecules.

The importance of the method is that it allows one to do a global analysis of all molecular species in terms of few algebraic parameters. In turn provides a way to make assignments of unknown levels or to check assignments of known levels. The study of vibrational excitations of these bio-molecules (proteins) has numerous importance not only in human life but also in scientific research.

5. ACKNOWKEDGEMENTS

The author Dr. Srinivasa Rao Karumuri would like to thank Prof. Thomson G Spiro for providing the necessary literature for this study. The authors Dr.Srinivasa Rao Karumuri and Prof. Ramendu Bhattacharjee are grateful to the DST, New Delhi for supporting this work. The author is very much grateful to the anonymous referee of this paper for his valuable suggestions and comments, which greatly helped to improve the quality of the paper.

Table 1. Comparison between the Observed and Calculated frequencies of the fundamental vibrations of Porphyrin and its substitution forms.

Sym	$\mathbf{E}_{Obs}(cm^{-1})$	$\mathbf{E}_{Calc}(cm^{-1})$	Δ (Obs-Calc) (cm^{-1})	$\mathbf{E}_{Obs}(cm^{-1})$	$\mathbf{E}_{Calc}(cm^{-1})$	Δ (Obs-Calc)(cm^{-1})
Ni (OEP) Molecule				**Ni Porphyrin Molecule**		
C_m-H vibrational mode						
$A_{1g}(\nu_1)$	3041	3041.9321	-0.9321	3042	3042.0322	-0.0322
$B_{2g}(\nu_{27})$	3041	3040.8903	+0.1103	3041	3041.0420	-0.0420
$E_{1u}(\nu_{36})$	3040	3040.0189	-0.0189	3041	3041.4001	-0.4001
C_b-C_b vibrational mode						
$B_{1g}(\nu_2)$	1602	1602.0445	-0.0445	1579	1579.0590	-0.0590
$A_{1g}(\nu_{11})$	1577	1577.9601	-0.9601	1509	1509.0589	-0.0589
$E_{1u}(\nu_{38})$	1604	1604.2822	-0.2822	1547	1548.9754	-1.9754
Cu (OEP) Molecule				**Mg (OEP) Molecule**		
C_m-H vibrational mode						
$A_{1g}(\nu_1)$	3041	3042.3001	-1.3001	3041	3039.3000	+1.7000
$B_{2g}(\nu_{27})$	.....	3052.3226	.....	.....	3052.3207	.....
$E_{1u}(\nu_{36})$	.....	3062.2923	.....	.....	3062.2910	.....
C_b-C_b vibrational mode						
$B_{1g}(\nu_2)$	1592	1594.6856	-2.6856	.....	1596.8243	.....
$A_{1g}(\nu_{11})$	1568	1575.6450	-7.6450	1578	1578.0634	-0.0634
$E_{1u}(\nu_{38})$	.....	1613.7239	.....	.....	1615.58	.....
Ni (TPP) Molecule				**Cu (TPP) Molecule**		
C_m-C vibrational mode						
$A_{1g}(\nu_1)$	1235	1234.4200	+0.5800	1234	1235.6438	-1.6438
$B_{2g}(\nu_{27})$	1269	1270.6832	-1.6832	.....	1245.0709	.....
$E_{1u}(\nu_{36})$	.....	1306.9467	.....	.....	1271.1534	.....
C_b-C_b vibrational mode						
$B_{1g}(\nu_2)$	1572	1571.9300	+0.0700	1530	1532.5800	-2.5200
$A_{1g}(\nu_{11})$	1504	1504.6540	-0.6540	.....	1524.7402	.....
$E_{1u}(\nu_{38})$	.....	1639.2243	.....	.....	1626.8234	.....
Ni (OEP)-d_4				**Cu (TMP)**		
C_m-D vibrational mode				C_m-C vibrational mode		
$A_{1g}(\nu_1)$	3041	3038.6800	+2.3200	1235	1236.8843	-1.8843
$B_{2g}(\nu_{27})$	3041	3040.4000	+0.6000	.....	1246.3940	.....
$E_{1u}(\nu_{36})$	3041	3042.1219	-1.1219	1256	1256.7238	-0.7238
C_b-C_b vibrational mode						
$B_{1g}(\nu_2)$	1602	1602.0484	-0.0484	1567	1567.5587	-0.5587
$A_{1g}(\nu_{11})$	1576	1577.9629	-1.9629	1495	1495.2902	-0.2902
$E_{1u}(\nu_{38})$	1604	1604.2889	-0.2889	-------	1639.7793	.....

Table 2. Comparison between the Observed and Calculated frequencies of C_b-C stretching vibrations of Nickel Octaethyl Porphyrin [Ni(OEP)] and its substituted form *i.e* Ni(OEP)-d_4.

n species	$\mathbf{E}_{Obs}$(cm^{-1})	$\mathbf{E}_{Calc}$(cm^{-1})	(Obs-Calc) (cm^{-1})	$\mathbf{E}_{Obs}$(cm^{-1})	$\mathbf{E}_{Calc}$(cm^{-1})	Δ(Obs-Calc)(cm^{-1})
	Ni(OEP) Molecule			**Ni(OEP)-d4 Molecule**		
			C_b-C vibrational mode			
A_{1g} (ν_5)	1025	1043.3471	-18.3471	1026	1024.1729	1.8271
B_{1g} (ν_{14})	1151	1134.4480	16.5520	1187	1168.2545	18.7455
A_{2g} (ν_{23})	1022	1045.5548	-23.5548	1029	1026.7901	2.2099
B_{2g} (ν_{31})	1019	1010.5280	8.4720	999	1006.2923	-7.2923
E_u (ν_{43})	……	1159.4680	…….		1165.7804	
E_u (ν_{45})	…….	994.4080	…….		978.6798	
			First Overtone			
A_{1g}(ν_5+ν_6)	1831	1837.3438	-6.3438	1828	1823.6649	4.3351
E_u		1981.8380			1924.4935	
B_{1g}		2039.4881			1948.6704	
A_{2g}		2040.7594			2019.2772	
E_u		2089.0281			2088.5504	
E_u		2126.0643			2189.3792	
A_{1g}(ν_{22}+ν_{23})	2135	2145.5906	-10.5906	2216	2246.3847	-30.3847
E_u		2190.3683			2289.3098	
E_u		2261.3456			2293.3070	
B_{1g}		2289.6720			2309.3572	
E_u		2324.6758			2365.8686	
E_u		2356.7683			2371.8268	
E_u		2454.6856			2398.7437	
E_u		2488.9103			2404.7578	
A_{1g}(ν_{28}+ν_{31})	2494	2490.1380	3.8610	2460	2452.6969	7.3031
B_{1g}		2497.4836			2479.8699	
			Second Overtone			
A_{1g}		2502.3920			2529.2334	
E_u		2519.2033			2530.8538	
A_{2g}(ν_3+ν_{23})	2541	2537.2890	3.7110	2539	2541.9693	-2.9693
A_{2g}(ν_{14}+ν_{29})	2568	2569.3040	-1.3040	2607	2609.5773	-2.5773
E_u		2582.2093			2601.3572	
A_{1g}(ν_{19}+ν_{23})	2614	2606.4803	7.5197	2604	2599.9575	4.0425
B_{1g}(ν_3+ν_{14})	2670	2689.3094	-19.3094	2710	2703.3547	6.6453
E_u		2730.3802			2734.8643	
A_{1g}		2772.9689			2767.8346	
E_u		2826.3283			2798.3468	
			Pyr breathing vibrational mode			
A_{1g} (ν_6)	806	804.1759	1.8241	802	801.6378	0.3622
B_{1g} (ν_{15})	761	751.2534	9.7466	758	759.7356	-1.7356
E_u (ν_{47})	……	765.7932			783.3495	
			First Overtone			
A_{1g}		1496.0304			1398.7654	
E_u		1524.7395			1404.8475	
E_u		1548.6704			1439.8364	
B_{1g}(ν_6+ν_{16})	1557	1559.2772	-2.2772	1481	1476.8364	4.1636
E_u		1668.5904			1558.8239	

E_u		1782.3804			1702.7529	
$A_{1g}(\nu_5+\nu_6)$	1831	1864.0326	-33.0326	1828	1825.4704	2.5296
E_u		1893.4056			1870.7354	
E_u		1899.0328			1892.7253	
			Second Overtone			
$A_{2g}(\nu_6+\nu_{21})$	2109	2131.9844	-22.9844	2114	2103.7364	10.2636
$B_{1g}(\nu_6+\nu_{20})$	2144	2148.4379	-4.4379	2148	2152.7856	-4.7856
$A_{1g}(\nu_4+\nu_6)$	2184	2231.9844	-47.9844	2189	2190.4356	-1.4356
E_u		2260.5412			2237.2455	
E_u		2339.6766			2290.5472	
A_{1g}		2310.9441			2367.3864	
E_u		2363.5840			2443.9763	
E_u		2417.2044			2489.8322	
E_u		2481.1734			2547.3453	
B_{1g}		2542.5424			2601.3643	
$A_{2g}(\nu_5+\nu_{19})$	2626	2616.8038	9.1962	2628	2629.7439	-1.7439
E_u		2683.3023			2668.5233	

Observed values taken from the reference [34-36]

Table 3. Calculated excited vibrational frequencies of C_m-H stretching vibrations of Porphyrins & its substituted forms (Cm^{-1}).

	Sym	E_{Obs}	E_{Calc}	E_{Obs}	E_{Calc}	E_{Obs}	E_{CalC}	E_{Obs}	E_{Calc}
		Ni (OEP)		**Ni Porphyrin**		**Cu (OEP)**		**Mg (OEP)**	
	$A_{1g}(\nu_1)$	3041	3041.93	3042	3042.03	3041	3042.30	3041	3042.30
n = 1	$B_{2g}(\nu_{27})$	3041	3040.89	3041	3041.04	.....	3052.32	.....	3052.32
	$E_{1u}(\nu_{36})$	3040	3040.01	3041	3041.40	.....	3062.29	.....	3062.29
	E_{1u}		5941.47		5951.92		5945.15		5922.78
	B_{1g}		5942.44		5951.37		5946.23		5923.63
	A_{2g}		5944.38		5951.73		5947.14		5924.36
n = 2	E_{1u}		5945.16		5952.00		5948.14		5924.89
	E_{1u}		5946.84		5953.35		5986.70		5924.65
	E_{1u}		5947.29		5953.72		5994.28		5925.15
	E_{1u}		5948.07		5954.35		6007.48		5925.94
	A_{1g}		8707.29		8730.98		8708.54		8676.16
	E_{1u}		8708.52		8731.73		8709.53		8676.95
	E_{1u}		8708.97		8731.97		8709.90		8677.24
	E_{1u}		8709.75		8732.33		8712.60		8679.38
	B_{1g}		8712.30		8731.90		8713.53		8680.12
n = 3	E_{1u}		8713.45		8732.96		8812.42		8681.44
	E_{1u}		8715.91		8735.95		8853.97		8683.71
	A_{1g}		8716.09		8735.02		8858.35		8683.79
	E_{1u}		8703.35		8737.94		8874.75		8684.60
	E_{1u}		8717.14		8737.94		8899.68		8685.87
	B_{1g}		8712.13		8738.08		8904.67		8691.29
	E_{1u}		8719.56		8738.93		8921.42		8695.86

Calculated excited vibrational frequencies of C_b- C_b stretching vibrations of Porphyrins & its substituted forms

Sym	E_{Obs}	E_{Calc}	E_{Obs}	E_{Calc}	E_{Obs}	E_{CalC}	E_{Obs}	E_{Calc}

		Ni (OEP)		Ni Por		Cu (OEP)		Mg (OEP)	
	$B_{1g}(\nu_2)$	1602	1602.04	1579	1579.05	1592	1594.68		1596.82
n = 1	$A_{1g}(\nu_{11})$	1577	1577.96	1509	1509.05	1568	1575.64	1578	1578.06
	$E_{1u}(\nu_{38})$	1604	1604.28	1547	1548.97		1613.72		1615.58
	A_{2g}		3143.88		3021.25		3138.57		3137.07
	E_{1u}		3159.17		3033.88		3157.61		3142.67
	B_{2g}		3170.90		3061.13		3164.55		3144.71
n = 2	E_{1u}		3183.36		3161.24		3176.65		3148.27
	E_{1u}		3192.04		3081.13		3190.09		3174.59
	E_{1u}		3200.82		3231.24		3195.69		3181.43
	E_{1u}		3216.12		3068.45		3215.85		3193.35
	A_{1g}		4696.54		4539.77		4688.79		4689.66
	E_{1u}		4720.62		4559.73		4707.83		4695.26
	E_{1u}		4729.40		4567.02		4714.77		4697.30
	E_{1u}		4744.70		4579.69		4766.28		4712.45
	B_{1g}		4794.54		4621.02		4783.99		4717.66
n = 3	E_{1u}		4816.94		4639.59		4869.11		4820.98
	E_{1u}		4865.10		4679.51		4878.12		4827.54
	A_{1g}		4868.71		4682.52		4894.87		4839.74
	E_{1u}		4817.61		5183.77		4925.89		4862.25
	E_{1u}		4889.18		4699.48		4927.63		4867.88
	B_{1g}		4762.34		4889.77		4933.51		4872.57
	E_{1u}		4895.60				4939.95		4874.32

Calculated excited vibrational frequencies of C_m-C & C_m-D stretching vibrations of Porphyrins & its substituted forms

	Sym	E_{Obs}	E_{Calc}	E_{Obs}	E_{Calc}	E_{Obs}	E_{CalC}	E_{Obs}	E_{Calc}
		Ni (TPP)		Cu (TPP)		Cu (TMP		Ni (OEP)-d_4	(C_m - D)
	$A_{1g}(\nu_1)$	1235	1234.42	1234	1235.64	1235	1236.88	3041	3038.68
n = 1	$B_{2g}(\nu_{27})$	1269	1270.68		1245.07		1246.39	3041	3040.40
	$E_{1u}(\nu_{36})$		1306.94		1271.15	1256	1256.72	3041	3042.12
	E_{1u}		2459.13		2417.34		2464.18		5952.05
	B_{1g}		2495.39		2427.57		2474.51		5953.77
	A_{2g}		2508.62		2436.20		2475.39		5953.91
n = 2	E_{1u}		2531.65		2452.85		2484.84		5955.49
	E_{1u}		2777.49		2459.33		2524.26		6007.76
	E_{1u}		2835.59		2470.61		2535.23		6017.93
	E_{1u}		2936.67		2445.64		2554.31		6035.62
	A_{1g}		3674.12		3545.08		3681.89		8774.90
	E_{1u}		3713.46		3554.51		3692.22		8776.62
	E_{1u}		3710.38		3557.95		3695.99		8777.25
	E_{1u}		3821.69		3583.47		3702.55		8778.34
	B_{1g}		4321.98		3633.87		3723.94		8781.91
n = 3	E_{1u}		3855.42		3669.38		3804.16		8888.28
	E_{1u}		4470.02		3675.60		3832.11		8914.19
	A_{1g}		4788.38		3687.14		3892.19		8969.91

	E_{1u}		4812.25		3704.90		3902.71		8979.66
	E_{1u}		4947.56		3708.45		3922.24		8997.77
	B_{1g}		5138.57		3617.35		3952.28		9025.63
	E_{1u}		5187.30		3718.93		3958.29		9031.21
Calculated excited vibrational frequencies of C_b-C_b stretching vibrations of Porphyrins & its substituted forms									
Sym		E_{Obs}	E_{Calc}	E_{Obs}	E_{Calc}	E_{Obs}	E_{CalC}	E_{Obs}	E_{Calc}
		Ni (TPP)		Cu (TPP)		Cu (TMP)		Ni (OEP)-d_4	
	$A_{1g}(\nu_1)$	1572	1571.93	1530	1532.58	1567	1567.55	1602	1602.04
n = 1	$B_{2g}(\nu_{27})$	1504	1504.65		1524.74	1495	1495.29	1576	1577.96
	$E_{1u}(\nu_{36})$		1639.22		1626.82		1639.77	1604	1604.28
	E_{1u}		3035.20		3018.75		3201.84		3143.88
	B_{1g}		3062.66		3027.25		3229.30		3159.17
	A_{2g}		3065.00		3034.43		3231.64		3170.90
	E_{1u}		3090.13		3042.27		3256.77		3183.36
	E_{1u}		3169.76		3120.83		3346.37		3192.04
	E_{1u}		3194.32		3139.46		3372.75		3200.82
	E_{1u}		3237.05		3171.88		3418.64		3216.12
	A_{1g}		4543.99		4471.00		4782.85		4696.54
	E_{1u}		4571.45		4478.84		4810.31		4720.62
	E_{1u}		4581.48		4481.70		4820.34		4729.40
	E_{1u}		4598.92		4502.90		4837.78		4744.70
	B_{1g}		4655.78		4678.74		4894.64		4794.54
	E_{1u}		4817.83		4726.22		5076.98		4816.94
n = 3	E_{1u}		4880.41		4828.30		5144.19		4865.10
	A_{1g}		5014.97		4846.17		5288.72		4868.71
	E_{1u}		5038.52		4879.35		5314.01		4817.61
	E_{1u}		5082.26		4930.39		5360.99		4889.18
	B_{1g}		5149.54		4940.60		5433.26		4762.34
	E_{1u}		5163.00		4945.56		5447.71		4895.60

Table 4. Values [(a)] of Algebraic Parameters Used in the calculation of C_m-H, C_m-D Stretching Modes of Porphyrins and its substituted forms.

	Ni(OEP)	Cu(OEP)	Mg(OEP)	Ni(TPP)	Cu(TPP)	Cu(TMP)	Ni Por	Ni(OEP)-d_4 (C_m -D)
N	44	44	44	44	44	44	44	59
A	-17.6802	-17.6820	-17.614	-2.213	-7.1740	-2.2173	-17.65	-13.043
A´	-0.24	-0.25	-0.28	-0.9985	-0.4302	-1.0182	-1.3108	-0.2782
λ	0.014	0.01136	0.009	0.1295	0.1072	0.0369	0.0113	0.0146
λ'	0.011	0.012	0.012	0.5685	0.2018	0.1073	0.0021	0.2361

[(a)] All values in cm^{-1} except N, which is dimensionless.

Table 5. Values [(a)] of Algebraic Parameters Used in the calculation of C_b-C_b Stretching Modes of Porphyrins and its substituted forms.

Ni(OEP)	Cu(OEP)	Mg(OEP)	Ni(TPP)	Cu(TPP)	Cu(TMP)	Ni Por	Ni(OEP)-d_4
N	140	140	140	140	140	140	140	140
A	-2.83	-2.825	-2.835	-2.7205	-2.7502	-2.8825	-2.691	-2.83
A´	-1.223	-1.286	-0.452	-1.986	1.0921	-1.223	-3.216	-1.223
λ	0.086	0.068	0.067	0.2403	0.028	0.2581	0.0713	0.086
λ'	0.047	0.092	0.020	0.0981	0.1823	0.0981	0.25	0.047

[(a)] All values in cm^{-1} except N, which is dimensionless.

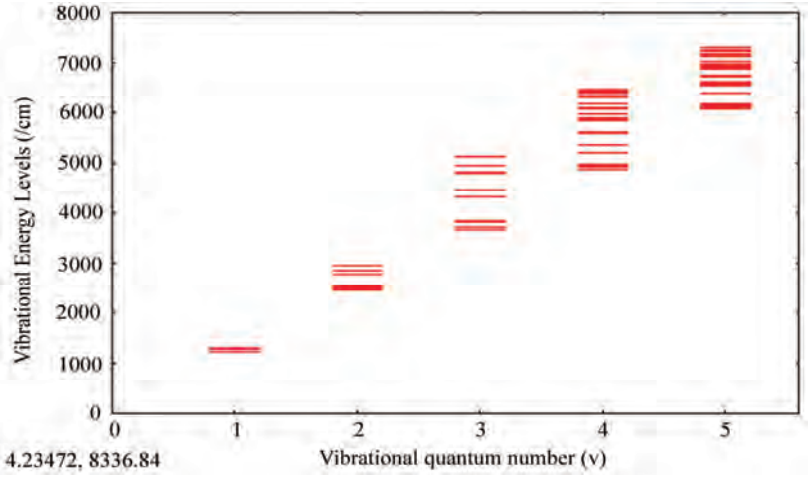

Figure 2. C_m-H band vibrational energy level of Ni(TPP).

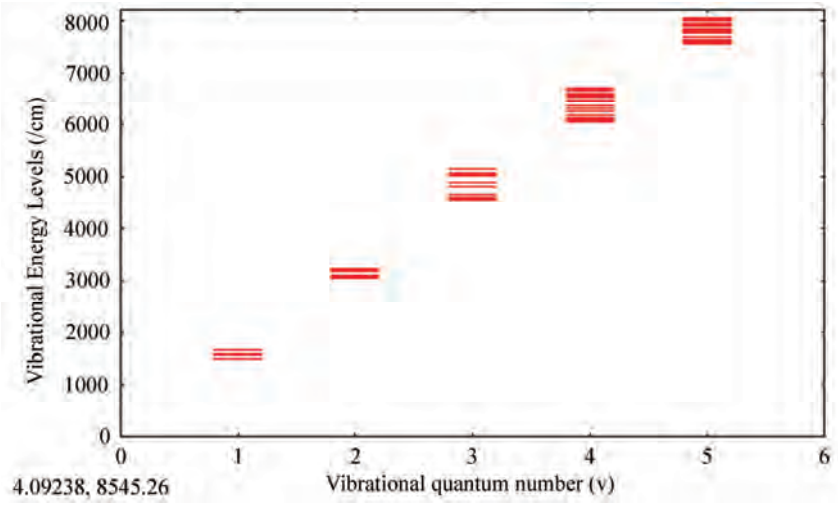

Figure 3. C_b-C_b band vibrational energy level of Ni(TPP).

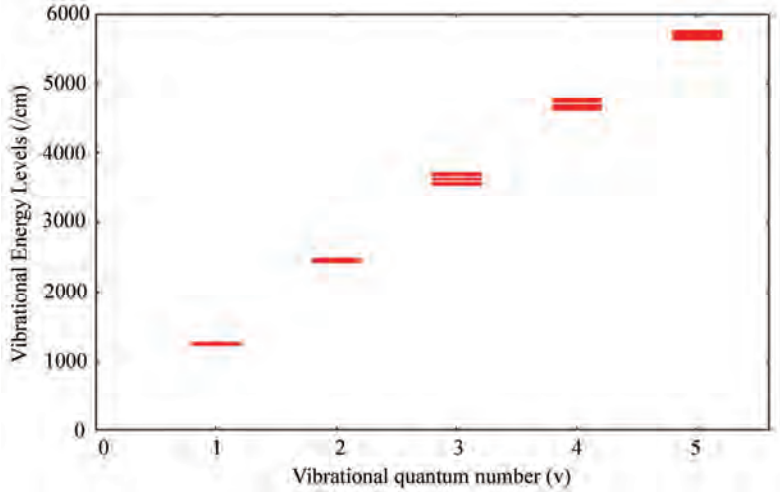

Figure 4. C_m-H band vibrational energy level of Cu(TPP).

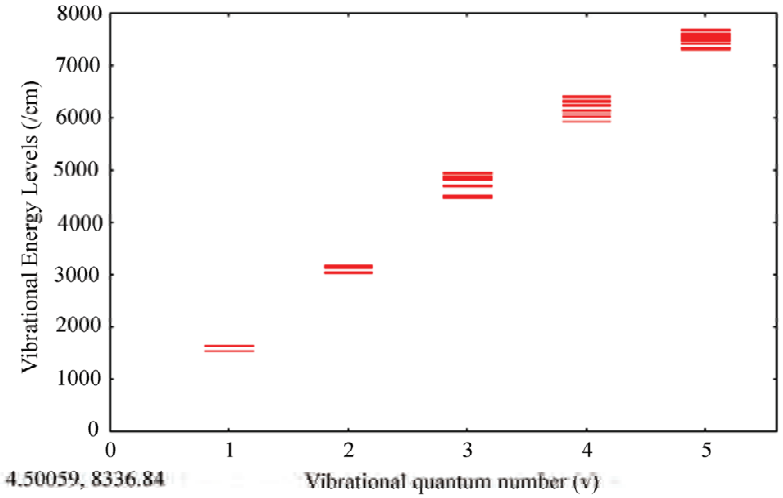

Figure 5. C_b-C_b band vibrational energy level of Cu(TPP).

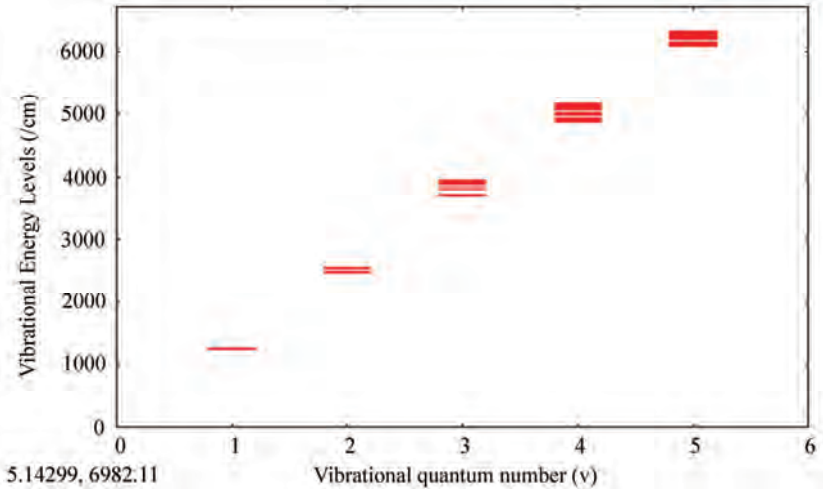

Figure 6. C_m-H band vibrational energy level of Cu(TMP).

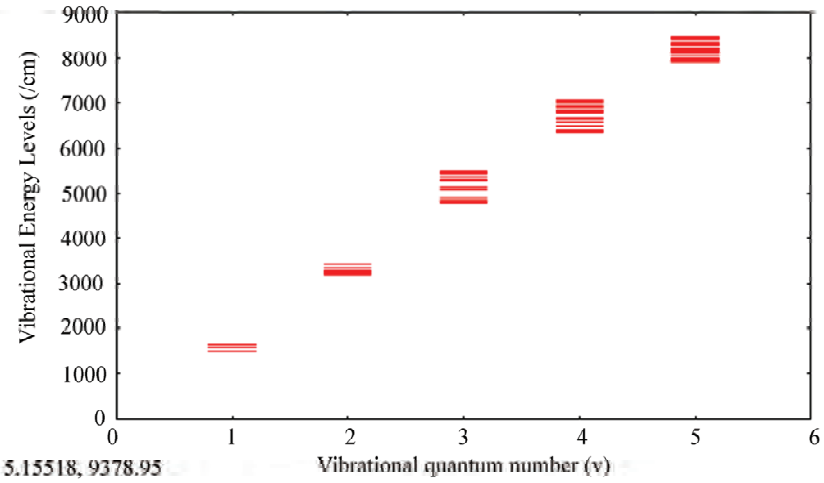

Figure 7. C_b-C_b band vibrational energy level of Cu(TMP).

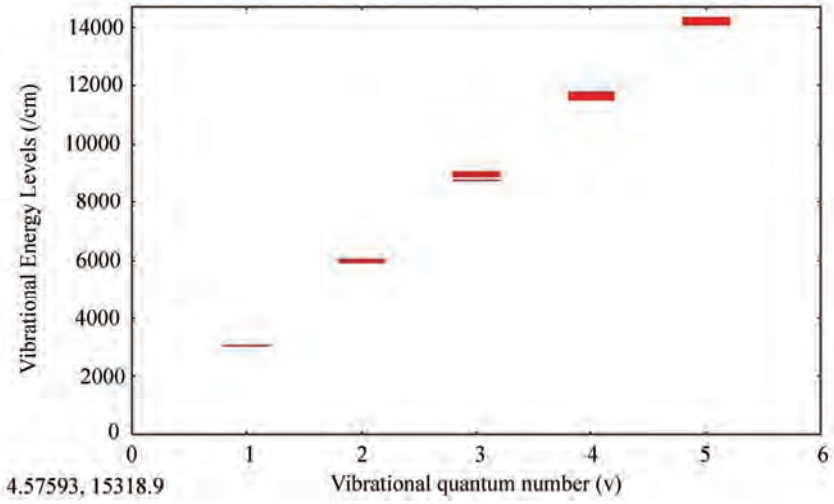

Figure 8. C_m-H band vibrational energy level of Ni(OEP)-d_4.

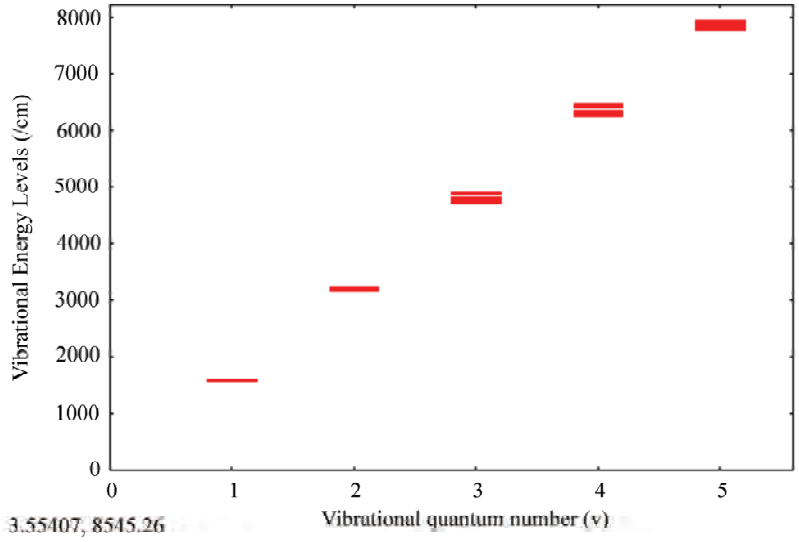

Figure 9. C_b-C_b band vibrational energy level of Ni(OEP)-d_4.

REFERENCES

[1] Iachello, F. (1981) Algebraic methods for molecular rotation-vibration spectra. *Chemical Physics Letters*, **78(3)**, 581-585.

[2] Iachello, F. and Levine, R.D. (1982) Algebraic approach to molecular rotation-vibration spectra. I. Diatomic molecules. *Journal of Chemical Physics*, **77(6)**, 3046-3055.

[3] Van Roosmalen, O.S., Dieperink, A.E.L. and Iachello, F. (1982) A dynamic algebra for rotation-vibration spectra of complex molecules. *Chemical Physics Letters*, **85(1)**, 32-36.

[4] Van Roosmalen, O.S., Iachello, F., Levine R.D. and Dieperink, A.E.L. (1983) Algebraic approach to molecular rotation–vibration spectra. II. Triatomic molecules. *Journal of Chemical Physics*, **79(6)**, 2515-2536.

[5] Sarkar, N.K., Choudhury, J. and Bhattacharjee, R. (2006) An algebraic approach to the study of the vibrational spectra of HCN. *Molecular Physics*, **104(19)**, 3051-3055.

[6] Sarkar, N.K., Choudhury, J. and Bhattacharjee, R. (2008) Algebraic approach: Study of vibrational spectra of some linear triatomic molecules. *Indian Journal of Physics*, **82(6)**, 767-772.

[7] Sarkar, N.K., Choudhury, J., Karumuri, S.R. and Bhattacharjee, R. (2009) A comparative study of the vibrational spectra of OCS and HCP using the Lie algebraic method. *European Physical Journal D*, **53(2)**, 163-171.

[8] Sarkar, N.K., Choudhury, J., Karumuri, S.R. and Bhattacharjee, R. (2008) An algebraic approach to the comparative study of the vibrational spectra of monofluoroacetylene (HCCF) and deuterated acetylene (HCCD). *Molecular Physics*, **106(5)**, 693-702.

[9] Choudhury, J., Karumuri, S.R., Sarkar, N.K. and Bhattacharjee, R. (2008) Vibrational spectroscopy of $SnBr_4$ and CCl_4 using Lie algebraic approach. *Pramana - Journal of Physics*, **71(3)**, 439-445.

[10] Choudhury, J., Sarkar, N.K. and Bhattacharjee, R. (2008) Algebraic approach to analyze the vibrational spectra of tetrahedral molecules. *Indian Journal of Physics*, **82(5)**, 561-565.

[11] Choudhury, J., Karumuri, S.R., Sarkar, N.K. and Bhattacharjee, R. (2009) Vibrational spectroscopy of CH/CD stretches in propadiene: An algebraic approach. *Chinese Physics Letters*, **26(2)**, 020308.

[12] Karumuri, S.R., Sarkar, N.K., Choudhury, J. and Bhattacharjee, R. (2008) Vibrational spectroscopy of C_m-H, C_b-C_b stretching vibrations of Nickel Metalloporphyrins: An algebraic approach. *Molecular Physics*, **106(14)**, 1733-1738.

[13] [Karumuri, S.R., Choudhury, J., Sarkar, N.K. and Bhattacharjee, R. (2008) Analysis of resonance raman spectra of Nickel Octaethyl Porphyrin using Lie algebra. *Journal of Environmental Research and Development*, **3(1)**, 250-256.

[14] Karumuri, S.R., Sarkar, N.K., Choudhury, J. and Bhattacharjee, R. (2009) Study of vibrational spectra of Nickel Metalloporphyrins: An algebraic approach. *Pramana - Journal of Physics*, **72(3)**, 517-525.

[15] Karumuri, S.R., Sarkar, N.K., Choudhury, J. and Bhattacharjee, R. (2009) Vibrational spectroscopy of stretching and bending modes of Nickel Tetra Phenyl Porphyrin: An algebraic approach. *Chinese Physics Letters*, **26(9)**, 093301.

[16] Karumuri, S.R., Sarkar, N.K., Choudhury, J. and Bhattacharjee, R. (2009) U(2) algebraic model applied to stretching vibrational spectra of Metalloporphyrins. *Journal of Molecular Spectroscopy*, **255(2)**, 183-188.

[17] Karumuri, S.R. and Prasad, A.S.R. (2009) Analysis of vibrational spectra of Copper Octaethyl Porphyrin [Cu (OEP)] using U(2) algebraic technique. *International Journal of Computational Mathematical Ideas*, **1(3)**, 68.

[18] Karumuri, S.R., Choudhury, J., Sarkar, N.K. and Bhattacharjee, R. (2010) Vibrational spectroscopy of C_m-C/ C_b-C_b stretching vibrations of Copper Tetramesityl Porphyrin Cu (TMP): An algebraic approach. *Pramana - Journal of Physics*, **74(1)**, 57-66.

[19] Iachello, F. and Oss, S. (1990) Overtone frequencies and intensities of bent XY_2 molecules in the vibron model. *Journal of Molecular Spectroscopy*, **142(1)**, 85-107.

[20] Iachello, F., Oss, S. and Lemus, R. (1991) Vibrational spectra of linear triatomic molecules in the vibron model. *Journal of Molecular Spectroscopy*, **146(1)**, 56-78.

[21] Iachello, F., Oss, S. and Lemus, R. (1991) Linear four-atomic molecules in the vibron model. *Journal of Molecular Spectroscopy*, **149(1)**, 132-151.

[22] Wang, M.S., Ding, S.L., Feng, D.T. and Liu, H.Y. (2002) Lie-algebraic approach to vibrational spectra of a linear symmetrical tetratomic molecule: C_2H_2. *Physical Review A*, **66**, (022506)1-10.

[23] Van Roosmalen, O.S., Levine, R.D. and Dieperink, A.E.L. (1983) The geometrical-classical limit of algebraic Hamiltonians for molecular vibrotational spectra. *Chemical Physics Letters*, **101(6)**, 512-517.

[24] Benjamin, I., Van Roosmalen, O.S. and Levine, R.D. (1984) A model algebraic Hamiltonian for interacting nonequivalent local modes with application to HCCD and $H^{12}C^{13}CD$. *Journal of Chemical Physics*, **81(7)**, 3352-3353.

[25] Van Roosmalen, O.S., Benjamin, I. and Levine, R.D. (1984) A unified algebraic model description for interacting vibrational modes in ABA molecules. *Journal of Chemical Physics*, **81(12)**, 5986-5997.

[26] Halonen, L. and Child, M.S. (1983) Model stretching overtone eigenvalues for SF_6, WF_6, and UF_6. *Journal of Chemical Physics*, **79(2)**, 559-570.

[27] Bowman, J.M., Wierzbicki, A. and Zuniga, J. (1988) Exact vibrational energies of non-rotating H_2O and D_2O using an accurate ab initio potential. *Chemical Physics Letters*, **150(3-4)**, 269-274.

[28] Iachello. F and Oss, S. (1991) Model of *n* coupled anharmonic oscillators and applications to octahedral molecules. *Physical Review Letters*, **66(23)**, 2976-2979.

[29] Iachello. F and Oss, S. (1991) Stretching vibrations of benzene in the algebraic model. *Chemical Physics Letters*, **187(5)**, 500-505.

[30] Alhassid, Y., Gursey, F. and Iachello, F. (1983) Group theory approach to scattering. *Annual Physics* (New York), **148(2)**, 346-380.

[31] Alhassid, Y., Gursey, F. and Iachello, F. (1983) Group theory of the Morse oscillator. *Chemical Physics Letters*, **99(1)**, 27-30.

[32] Levine, R.D. (1983) Representation of one-dimensional

motion in a morse potential by a quadratic Hamiltonian. *Chemical Physics Letters*, **95(2)**, 87-90.

[33] Child, M.S. and Halonen, L.O. (1984) Overtone frequencies and intensities in the local mode picture. *Advances in Chemical Physics*, **57**, 1-58.

[34] Li, X.-Y., Czernuszewicz, R.S., Kincaid, J.R., Stein, P. and Spiro, T.G., (1990) Consistent porphyrin force field. 2. Nickel octaethylporphyrin skeletal and substituent mode assignments from nitrogen-15, meso-d4, and methylene-d16 Raman and infrared isotope shift. *Journal of Physical Chemistry*, **94(1)**, 47-61.

[35] Kitagawa, T., Abe, M. and Ogoshi, H. (1978) Resonance Raman spectra of octaethylporphyrinato-Ni(II) and meso-deuterated and 15N substituted derivatives. I. Observation and assignments of nonfundamental Raman lines. *Journal of Chemical Physics*, **69(10)**, 4516-4525.

[36] Czernuszewicz, R.S., Macor, K.A., Li, X.-Y., Kincaid, J.R. and Spiro, T.G. (1989) Resonance Raman spectroscopy reveals a1u vs. a2u character and pseudo-Jahn-Teller distortion in radical cations of nickel(II), copper(II), and chloroiron(III) octaethyl- and tetraphenylporphyrins. *Journal of the American Chemical Society*, **111(11)**, 3860-3869.

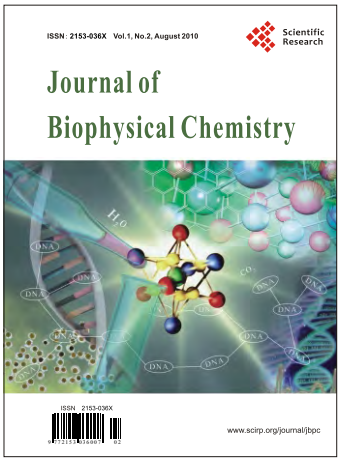

Call for Papers

Journal of Biophysical Chemistry

ISSN 2153-036X (Print) ISSN 2153- 0378 (Online)
http://www.scirp.org/journal/jbpc

Journal of Biophysical Chemistry (JBPC) is an international journal dedicated to the latest advancement in related research fileds. The goal of this journal is to provide a platform for scientists and academicians all over the world to promote, share, and discuss various new issues and developments in different aspects of biophysical chemistry.

Editor-in-Chief

Prof. Cornelis J. Van der Schyf Northeastern Ohio Universities Colleges of Medicine and Pharmacy, USA

Editorial Board (According to Alphabet)

Subject Coverage

This journal invites original research and review papers that address the following issues. Topics of interest include, but are not limited to:

Agronomy Agriculture
Bioenergetics
Biomechanics
Biomolecular and Drug Databases
Biomolecular Free Energy
Biomolecular Structure
Covering Dynamics
Dynamical Systems
Gene Regulation
Graph/Network Theory
Medicine and Neuroscience
Molecular Docking
Molecular Dynamics Simulation
Neural Networks
Nucleic Acid Structure
Patch Clamping
Pharmacology and Physiology
Phylogenetics
Population Modeling
Protein Structure Prediction
Quantum Biophysics
Quantum Chemistry
Sequence Alignment
Single Protein Dynamics
Stochastic Processes
Structural Alignment
Structural Biology
Structure-Activity Relationships

We are also interested in short papers (letters) that clearly address a specific problem, and short survey or position papers that sketch the results or problems on a specific topic. Authors of selected short papers would be invited to write a regular paper on the same topic for future issues of the ***JBPC.***

Notes for Intending Authors

Submitted papers should not have been previously published nor be currently under consideration for publication elsewhere. Paper submission will be handled electronically through the website. All papers are refereed through a peer review process. For more details about the submissions, please access the website.

Website and E-Mail

http://www.scirp.org/journal/jbpc E-mail: jbpc@scirp.org

Journal of Biophysical Chemistry, 2010, 1, 77-132
Published Online August 2010 in SciRes (http://www.SciRP.org/journal/jbpc/).

TABLE OF CONTENTS

Volume 1 Number 2 **August 2010**

